Computational Gas Dynamics with the Lattice Boltzmann Method

Preconditioning and Boundary Conditions

Salvador Izquierdo Estallo

June 2008

Agradecimientos

El trabajo contenido en esta Tesis se ha desarrollado durante los cuatro años de duración (2004-2007) de la beca-contrato predoctoral I3P-CSIC, financiada por el Fondo Social Europeo, y bajo la supervisión del Prof. Norberto Fueyo. El centro de desarrollo ha sido el Laboratorio de Investigación en Tecnologías de la Combustión (LITEC), centro mixto del Consejo Superior de Investigaciones Científicas (CSIC), de la Universidad de Zaragoza (UZ) y de la Diputación General de Aragón (DGA). La continuación del trabajo realizado es financiado en la actualidad (2008-2010) por el Gobierno de España a través del proyecto ENE2007-67217/ALT *Simulación del campo local de vientos mediante métodos de lattice Boltzmann para la predicción de la potencia entregada por parques de aerogeneradores*. Durante el desarrollo de la Tesis se realizó una breve estancia (Septiembre - Diciembre 2005) en el Instituto para la Modelización Computacional en Ingeniería Civil (IRMB, Prof. Manfred Krafczyk) en la Universidad Técnica de Braunschweig, financiada por el Servicio Alemán de Intercambios Académicos (DAAD).

Cumplidas las formalidades, quisiera remarcar que el carácter eminentemente unipersonal de la elaboración de una Tesis (que no del trabajo científico-técnico) no debe relegar la imprescindible labor realizada por todos aquellos que de una forma u otra han colaborado a lo largo del proceso. Muchos y de diversa índole son los agradecimientos que quisiera expresar, ya que es la relación con todas estas personas (y no este documento por sí mismo) lo que conforma el resultado más interesante obtenido.

En primer lugar agradecer a Norberto Fueyo la confianza depositada para desarrollar el trabajo con total libertad, así como el interés mostrado por mis ideas y aportaciones. Es de agradecer también el cuidado por los temas logísticos (i.e. financiación, equipos, formación continua, ambiente de trabajo), y, quizá por encima del resto, la oportunidad de conocer aspectos de la vida investigadora que seguro son útiles en un futuro.

On the other hand, I would like to acknowledge Prof. Krafczyk and Dr. Tölke for their dedication during my brief stay in their institute, which motivated me for the learning about lattice Boltzmann methods. Really fruitful was also the contact with the people of the ICMMES conference.

A los ¡compañeros! del Área de Mecánica de Fluidos especialmente a todo áquel con el que haya perdido-invertido tiempo discutiendo sobre cualquier tema relacionado con esta Tesis, o con cualquier otro tema.

A los amigos amantes de una vida aventurera, porque el soñar en otros mundos, y a veces vivirlos, ayuda, y mucho, a seguir adelante en el trabajo diario; y a relativizar la insignificante importancia de los éxitos y fracasos que acontecen.

A los amigos, los que siempre están ahí.

A mi familia.

A Alba, compañera y amiga, quizá más lo primero que lo segundo y también viceversa; gracias por ser y por estar.

Zaragoza, Mayo de 2008

Resumen

La ecuación de lattice Boltzmann (LB) es un método de Fluidodinámica Computacional (CFD) que aproxima la solución de las ecuaciones de Navier-Stokes incompresibles en el límite de números de Mach y de Knudsen bajos. El trabajo de esta Tesis se centra en el desarrollo de nuevas aproximaciones a dos aspectos numéricos: (i) *condiciones de contorno*, incluyendo la modificación de condiciones de contorno existentes para el tratamiento de la interacción entre contornos y ondas de presión, y la extensión necesaria para incluir condiciones de contorno relacionadas con gradientes de variables macroscópicas; y (ii) *precondicionamiento*, derivando métodos de lattice Boltzmann equivalentes a precondicionadores temporales de las ecuaciones de Navier-Stokes, y analizando las mejoras obtenidas.

El efecto de la interacción entre los contornos abiertos (entradas y salidas de flujo) y el dominio fluido se estudian en simulaciones transitorias con el método de lattice Boltzmann. Se concluye que los métodos de lattice Boltzmann sufren los mismos problemas que otros métodos compresibles o pseudo-compresibles para la resolución del flujo de fluidos; esto es, los contornos reflejan las ondas de presión, y esto tiene una influencia relevante en la solución y en la velocidad de convergencia, tanto de simulaciones de flujos estacionarios como transitorios, incluso a números de Reynolds muy bajos. Sin embargo, existen soluciones prácticas, como el uso de algún tipo de condición de contorno que considere ciertas derivadas igual a cero o condiciones de contorno no reflectivas. Se presentan y validan dos nuevas condiciones de contorno no reflectivas: la primera se basa en el filtrado temporal de la presión en contornos con condición tipo Dirichlet para la velocidad, la segunda se basa en el análisis del movimiento de información a través de las características de Euler. Esta última condición puede aplicarse para la velocidad y para la presión, en estacionario y en transitorio, y tanto con condiciones de contorno tipo Dirichlet como Neumann. En relación a otras condiciones de contorno características semejantes, empleadas en métodos de volúmenes finitos o diferencias finitas para la resolución de las ecuaciones de Navier-Stokes, se necesita introducir algunas correcciones para compensar la naturaleza isoterma e incompresible del método de lattice Boltzmann empleado en la resolución de flujo fluido. Los resultados muestran que la condición de contorno característica propuesta es altamente no-reflectiva, conserva la masa, y no necesita ninguna capa absorbente adicional.

Las condiciones de contorno relacionadas con gradientes de variables macroscópicas necesitan, en los métodos de lattice Boltzmann, un equilibrio en su implementación entre la complejidad del esquema y la precisión obtenida. Se presenta una generalización de la condición de contorno basada en la transferencia de cantidad de movimiento, donde la localización del contorno se realiza mediante interpolaciones en las direcciones de las uniones entre los nodos (típicamente empleado para imponer condiciones de contorno tipo Dirichlet) y el gradiente macroscópico se incorpora mediante un cierto esquema de diferencias finitas. De esta forma se obtiene una aproximación estable para geometrías arbitrarias que se puede aplicar para imponer condiciones de contorno tipo Neumann y Robin. La propuesta se valida para condiciones de contorno relacionadas con esfuerzos en la pared y para condiciones de contorno de presión. Diferentes configuraciones bidimensionales, tanto en estado transitorio como estacionario, son usadas como casos test.

El precondicionamiento de las ecuaciones de Navier-Stokes es una técnica ampliamente utilizada en las simulaciones de Fluidodinámica Computacional de flujos estacionarios. En esta tesis se realiza un estudio sistemático de los precondicionadores temporales para las ecuaciones de Navier-Stokes que se pueden obtener a partir de la ecuación generalizada de lattice Boltzmann. Dicha ecuación generalizada presenta cierto número de parámetros ajustables que permiten el acceso a una hidrodinámica más general. Empezando desde este método de lattice Boltzmann totalmente parametrizado y aplicando restricciones relacionadas con la isotropía, la invarianza Galileana y con la correcta recuperación de las ecuaciones de Navier-Stokes, se obtiene un esquema precondicionado con dos parámetros libres (β y γ). Estos dos precondicionadores son estudiados en función de su número de condicionamiento y comparados con los precondicionadores de Navier-Stokes.

El precondicionador γ se estudia con más detalle. La idea fundamental de este precondicionador es la modificación de los términos cuadráticos de la velocidad de la función de distribución en equilibrio, de tal forma que la ecuación que se obtiene tras la expansión de Chapman-Enskog corresponda con las ecuaciones de Navier-Stokes con un precondicionador temporal. Se han buscado los valóres óptimos de γ tanto de forma numérica como teórica, esto último mediante el análisis de estabilidad lineal y mediante el número de condición. También se estudia la influencia del operador de colisión aplicado, realizando esencialmente una comparación entre el método de un solo tiempo de relajación (SRT) y el método de múltiples tiempos de relajación (MRT). Finalmente se sugieren ciertos criterios para seleccionar *a priori* el valor óptimo de γ. El método de lattice Boltzmann con el operador de colisión MRT y el valor óptimo de γ mejora simultáneamente la velocidad de convergencia, la estabilidad y la precisión de las simulaciones de lattice Boltzmann, si se compara con los métodos no precondicionados y con los métodos SRT óptimamente precondicionados. Se estudian dos aspectos adicionales: el precondicionamiento temporal directo de la ecuación de lattice Boltzmann y el mal condicionamiento de dicha ecuación, ambos

como casos especiales de esquemas relajados.

En conclusión, se presentan y validan diferentes elementos para la realización de simulaciones eficientes y con ciertas condiciones de contorno complejas emplendo el método de lattice Boltzmann. Se espera que estas propuestan ayuden a la generalización del uso de los métodos de lattice Boltzmann como una técnica estándar de CFD.

Abstract

The standard Lattice Boltzmann (LB) equation is a Computational Fluid Dynamics (CFD) method that approximates the incompressible solution of the Navier-Stokes (NS) equations in the low Mach and Knudsen number limit. This Thesis focuses on the development of new approaches for two numerical aspects of lattice Boltzmann methods: (i) *Boundary Conditions*, modifying existing open boundary conditions for the treatment of the interaction between boundaries and pressure waves, and extending macroscopic-gradient-related conditions in arbitrary geometries; and (ii) *Preconditioning*, developing equivalent lattice Boltzmann methods of time-derivative preconditioned Navier-Stokes schemes, and analyzing its improved behavior.

The effects of the interaction between the open boundaries (inflow and outflow) and the fluid domain are studied in unsteady lattice Boltzmann simulations of fluid flow. We conclude that lattice Boltzmann methods suffer from the same problems with open boundaries as other compressible or pseudo-compressible approximations for the numerical solution of fluid flows: these boundaries reflect pressure waves, and this has a relevant influence on the solution and convergence rate of both steady and unsteady flows, even at very low Reynolds numbers. However, practical solutions considering zero derivatives at the outflow or non-reflecting boundaries are possible. Two novel non-reflecting boundary conditions are introduced and tested: the first one is based on the temporal filtering of the pressure at Dirichlet-velocity boundaries; the second one is based on the movement of information through Euler characteristics. The latter can be applied for pressure and velocity, with both Dirichlet and Neumann conditions. With respect to similar characteristic conditions used in finite-difference or finite-volume implementations, some corrections are needed to compensate the isothermal compressible nature of standard lattice Boltzmann methods for fluid flow. The results show that the proposed Euler-characteristic boundary condition for lattice Boltzmann methods is highly non-reflecting, mass-conserving, and does not need additional buffer layers.

Boundary conditions for macroscopic-gradient related behaviors in arbitrary geometries with lattice Boltzmann methods require a trade-off between the complexity of the scheme and the accuracy obtained. A generalization of the momentum transfer boundary condition is presented, where the arbitrary location of the boundary is

addressed with link-wise interpolations (used for Dirichlet conditions) and the macroscopic gradient is taken into account with a finite-difference scheme. This leads to a stable approach for arbitrary geometries which can be used to impose Neumann and Robin boundary conditions. The proposal is validated for stress boundary conditions at walls and for pressure gradient conditions. Several two-dimensional steady and unsteady configurations are used as test cases.

The preconditioning of Navier-Stokes equations is a widely used technique to speed up CFD simulations of steady flows. In this Thesis, a systematic study is performed of time-derivative preconditioners of Navier-Stokes equations that can be derived from the generalized lattice Boltzmann equation. In this way, lattice Boltzmann models equivalent to preconditioned Navier-Stokes systems are built, and it becomes possible to take advantage of the pre-existing knowledge in this field to improve the convergence to steady state of lattice-Boltzmann flow-calculations. The generalized lattice Boltzmann equation presents a number of tuneable parameters, which provide access to a generalized hydrodynamics. Starting from this fully parametrized lattice Boltzmann scheme, and applying restrictions to account for isotropy and Galilean invariance, and for a correct recovery of the Navier-Stokes equations (through a Chapman-Enskog expansion), a preconditioned scheme with two free parameters (β and γ) is obtained. The β- and γ-preconditioners are studied according to their condition number and compared with typical Navier-Stokes preconditioners.

The γ-preconditioner is studied in more detail. The key idea in this preconditioner is to modify the u^2 terms of the equilibrium distribution function in such a way that, by the means of a Chapman-Enskog expansion, a time-derivative preconditioner of the Navier-Stokes equations is obtained. In this contribution, the optimal values for the free parameter γ are searched for numerically and theoretically; the latter with the aid of linear stability analysis and with the condition number of the Navier-Stokes system of equations. The influence of the collision operator, single- (SRT) versus multiple-relaxation-times (MRT), is also studied for all the cases. Finally, guidelines are suggested for an *a priori* definition of optimal preconditioning parameters as a function of the Reynolds and Mach numbers. The new optimally preconditioned MRT method derived is shown to improve, simultaneously, the rate of convergence, the stability and the accuracy of the lattice Boltzmann simulations, when compared to the non-preconditioned methods and to the optimally preconditioned SRT one. Two additional aspects are studied, namely: the time-derivative preconditioning of the LB equation and the ill-conditioning LB method; both as special types of relaxed schemes.

In summary, several tools for efficient lattice Boltzmann simulations of fluid flow with complex boundary behaviors have been developed and validated. These are expected to further increase the applicability of the lattice Boltzmann method as a standard CFD technique.

Contents

Background and Outline

Computational Fluid Dynamics (CFD) has become a paramount tool for the optimal design of new products in industry (e.g. aeroplanes, wind turbines, combustion chambers or heat exchangers), and for the study from a new viewpoint of some of the present-day scientific and technological challenges (e.g. rocket engines, micro-electromechanical systems or biological processes). CFD techniques are progressively being made available to industrial sectors for which only a few years ago they were not due to its unaffordable computational and/or economic cost. The rapid extension of the CFD capabilities, and the spread and generalization of its use in industrial and academic environments, motivate the development of more efficient, robust and general techniques. The final goal of a single multi-scale multi-physics solver is far from being attained; however, there exist commercial CFD software packages that integrate (with various degrees of success) several solvers for multipurpose applications, which reflects the demand for integrated and generalized approaches. A master solver for transport phenomena should be based on first principles (i.e. molecular dynamics). From a practical point of view this means simpler equations to solve but an impracticable number of degrees of freedom for real configurations. A promising approach for this problem is the use of different kinds of coarse graining techniques (e.g. dissipative particle dynamics - DPD, smoothed-particle hydrodynamics - SPH, stochastic rotation dynamics - SRD or lattice Boltzmann methods - LBM), which allow to work from first principles, but only with the subset of information which is essential for the process of interest. This research field has led to the development in Fluid Mechanics of the so-called mesoscopic methods. These methods are mainly based on the kinetic theory of gases and are, probably after combination with existing efficient methods, the kernel of the future multi-purpose transport-phenomena solvers.

Among mesoscopic methods, one of the most popular, due to its simplicity and performance properties, is the lattice Boltzmann equation. Although its potential to include complex effects from the nanoscale, this method is nowadays basically used for fluid flow simulations in the continuum limit and also for moderate Knudsen number flows (slip regime).

The development and the continuous improvement of lattice Boltzmann methods for fluid flow simulation is brought about by three different approaches to the method: (i)

a physical approach, focusing on the development of new lattice Boltzmann methods that improve the stability and accuracy properties for fluid flow simulations, and that allow to model other phenomena than mass and momentum transport in the continuum limit; (ii) a mathematical approach, which is devoted to the development of new efficient numerical schemes for kinetic methods; and (iii) an engineering approach, motivated by the high performance of the model and the new perspectives in different technologies opened up by these methods.

Objectives

In the context of lattice Boltzmann as a CFD tool for the continuum limit, this Thesis focuses on the following aspects:

1. The extension of existing boundary conditions for real CFD applications, by
    - developing non-reflecting conditions to avoid the spurious interaction of boundaries with the fluid domain due to the compressible nature of the method; and
    - expanding the applicability of well-established treatments for Dirichlet boundary conditions to include macroscopic-gradient-related effects.
2. The improvement of the performance of the lattice Boltzmann method, through the stabilization and acceleration to the steady state;
    - developing new preconditioned LB schemes; and
    - optimizing the use of the preconditioners.

Boundary conditions developed for lattice Boltzmann methods are principally Dirichlet-velocity boundary conditions for straight and curved walls. However, CFD simulations of real configurations are characterized by complex geometries, and complex boundary conditions for modeling a variety of situations. This motivates the objectives of this Thesis related to boundary conditions.

The performance of lattice Boltzmann methods is hindered by its kinetic origin and its pseudo-compressible behavior. Important improvements are needed to be competitive with classical CFD solvers. These improvements are mainly related to the stability of the method, but also to the time to reach the steady state and even with the accuracy of the method. To overcome these limitations, the search of novel effective, robust and simple lattice Boltzmann schemes is required.

Contents

The outline of the Thesis is as follows:

- In *Chapter 1 – Lattice Boltzmann methods for CFD*, the fundamentals of lattice Boltzmann methods are briefly introduced.

- In *Chapter 2 – Non-reflecting open boundary conditions*, the problem of working with artificially-truncated boundaries and the associated pressure wave reflection is described, and its effects are analyzed in lattice Boltzmann simulations of viscous fluid flows. As a solution for this problem, two new non-reflecting boundary conditions are presented: the first one is only valid for Dirichlet steady open boundaries and it is based on the temporal filtering of the density; the second one is valid for Dirichlet and Neumann, steady and unsteady boundaries, and it is based on the analysis of the information traveling through Euler characteristics.

- In *Chapter 3 – Gradient-based boundary conditions*, a novel, simple and stable scheme is introduced to specify macroscopic-gradient boundary conditions. It is based on the extension of link-wise interpolations used to implement Dirichlet conditions in complex geometries, in which the macroscopic gradient is explicitly built within the boundary scheme by the means of a predefined finite difference stencil.

- In *Chapter 4 – Preconditioning: derivation*, the derivation of modified lattice Boltzmann methods is presented, which are obtained to be equivalent to time-derivative preconditioned Navier-Stokes schemes. Two different lattice Boltzmann preconditioners are obtained: the β- and the γ-preconditioner, which are based, respectively, on the modification of the linear and the quadratic velocity terms of the equilibrium distribution function.

- In *Chapter 5 – The γ-preconditioner*, which is derived in the previous Chapter is systematically analyzed. Its stability properties and limits are theoretically studied, as well as its acceleration potential in explicit computations of steady state problems. Furthermore, the same properties are studied numerically to find that preconditioned lattice Boltzmann methods improve simultaneously the stability, the accuracy and the acceleration to the steady state.

- In *Chapter 6 – Conclusions*, where general conclusions about the results obtained are drawn, and possible future work is discussed in the field of boundary conditions and preconditioning for lattice Boltzmann methods.

Scientific production

A two-dimensional and a parallel three-dimensional code for solving the lattice Boltzmann equation has been developed as part of the work of this Thesis, but the dissertation reports mainly those results that are novel in the field. Most of these results have been published (or are in the process of being published) by the author in the following papers:

1. Martínez-Lera P, **Izquierdo S**, Fueyo N. Lattice-Boltzmann LES of Vortex Shedding in the wake of a Square Cylinder. In Complex Effects in Large Eddy Simulations, *Lectures Notes in Computational Science*, Springer, 56, 203-217, 2007.

2. **Izquierdo S**, Fueyo N. Preconditioned Navier-Stokes schemes from the generalized lattice Boltzmann equation. *Progress in Computational Fluid Dynamics*, 8(1-4),189-196, 2008.

3. **Izquierdo S**, Martínez-Lera P, Fueyo N. Analysis of open boundary effects in unsteady lattice Boltzmann simulations. *International Journal of Computational Fluid Dynamics* (Accepted)

4. **Izquierdo S**, Fueyo N. Characteristic non-reflecting boundary conditions for open boundaries in lattice Boltzmann methods. *Physical Review E* (Submitted)

5. **Izquierdo S**, Fueyo N. Optimal lattice Boltzmann preconditioning: convergence acceleration, stability and accuracy improvements. (In preparation)

6. **Izquierdo S**, Fueyo N. Momentum transfer correction for macroscopic-gradient boundary conditions in lattice Boltzmann methods. (In preparation)

1

Lattice Boltzmann methods for CFD

The relationship between the use of the Navier-Stokes equations and the Boltzmann equation for the study of the gas dynamics has been an active reseach field in the last decades [1, 2]. One of the most relevant characteristic of the Boltzmann equation is its capability to represent gas flows for a wider range of Mach and Knudsen numbers than the Navier-Stokes equations can. On the other hand, numerical methods for solving the Navier-Stokes equations are generally much more efficient than those used for solving the Boltzmann equations, and therefore the former ones are preferred when fluid flows are simulated within the continuum limit. The development of the lattice-gas automata [3, 4] and subsequent early works [5, 6] were the first steps towards the use of a simplified versions of the Boltzmann equation, viz. the lattice Boltzmann method, for simulating fluid flow within the continuum limit in an efficient way. Since these first approaches, the method has evolved and has now become a real alternative [7] to classical fluid-flow solvers based on the solution of discretized versions of the Navier-Stokes equations.

1.1 The lattice Boltzmann method

Lattice Boltzmann (LB) methods [8, 9, 10, 11, 12] encompass those schemes developed to solve the Boltzmann equation restricted to a finite (and minimal) number of microscopic velocities which fulfill some lattice-symmetry properties, preserving spatial invariance up to a specified order and allowing the conservation of some defined macroscopic moments (e.g. mass and momentum) [13, 14]. The standard lattice Boltzmann method [15] is an explicit-time-step solver for isothermal compressible

flows within the continuum and incompressible limit. It splits each temporal step in a propagation step, which accounts for advection, and in a collision step, to represent inter-particle interactions. This construction results in a second order method in space and first order in time [16] with very low numerical diffusion (it is present in fourth-order terms) [17].

The lattice Boltzmann equation can be derived from the Boltzmann equation [13, 14], which is an equation for the evolution of the particle-velocity distribution, by discretizing the velocity space using a finite set of velocity vectors (for a complete description of the Boltzmann equation see [1, 18, 19]):

$$\frac{\partial f_\alpha}{\partial t} + e_{i\alpha}\frac{\partial}{\partial x_i} f_\alpha = \Omega_\alpha \, ; \tag{1.1}$$

where f_α is the particle distribution function, $e_{i\alpha}$ is the discrete set of velocities and Ω_α is the collision operator.

A particular scheme is obtained by using an Euler time discretization and an upwind spatial one, which allows for simplified and highly efficient implementation (see for example [20, 21, 22]).

1.1.1 Multi-relaxation-time lattice Boltzmann method

A Multi-Relaxation-Time (MRT) collision operator [23, 24] is used in this work. For a $DdQq$ model (with d dimensions and q velocities $e_\alpha \in V = \mathbb{R}^q | \alpha = 0, 1, ..., N$, and $N = q - 1$), a set of velocity distribution functions $\{f_\alpha \in V = \mathbb{R}^q | \alpha = 0, 1, ..., N\}$ is defined at each node $\{x_i \in \delta x \mathbb{Z}_d | i = 1, ..., d\}$. The MRT-LB evolution equation for f_α, at discrete time $t \in \delta t \mathbb{N}$, is the following:

$$\begin{aligned} f_\alpha(x_i + e_{i\alpha}\delta t, t + \delta t) - f_\alpha(x_i, t) = \; & - \; M^{-1}_{\alpha\beta} S_{\alpha\beta} [m_\alpha(x_i, t) - m^{eq}_\alpha(x_i, t)] \\ & + \; F_\alpha(x_i, t) \, ; \end{aligned} \tag{1.2}$$

where $S_{\alpha\beta}$ is a $q \times q$ diagonal relaxation matrix; and $M_{\alpha\beta}$ is a $q \times q$ matrix which linearly transforms the velocity distribution functions f_α to the macroscopic moments: $m_\alpha = M_{\alpha\beta} f_\alpha$. The external body force F_α is approximated as:

$$F_\alpha = w_\alpha \rho_0 c_s^{-2} (e_{i\alpha} a_i) \, , \tag{1.3}$$

where a_i is the acceleration induced by this force, and w_α are the lattice weighting factors detailed bellow. This body force approach is valid for temporally- and spatially-constant accelerations, such as gravity; an improved description for time- and space-dependant body forces can be found in [25].

To solve the evolution equation for the particle distribution function, Eq. (1.2), two steps are performed:

$$\text{collision: } \tilde{f}_\alpha(x_i, t) = f_\alpha(x_i, t) - M^{-1}_{\alpha\beta} S_{\alpha\beta} [m_\alpha(x_i, t) - m^{eq}_\alpha(x_i, t)] \, ; \tag{1.4a}$$

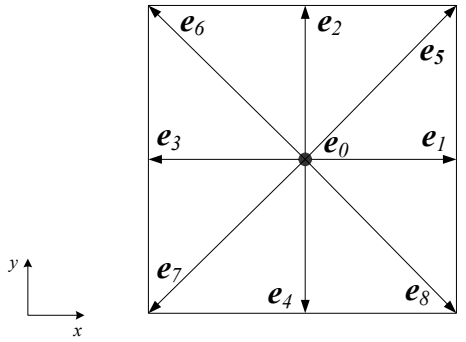

Figure 1.1: D2Q9 lattice used for two dimensional simulations.

$$\text{propagation: } f_\alpha(x_i + e_{i\alpha}\delta t, t + \delta t) = \tilde{f}_\alpha(x_i, t)\ . \tag{1.4b}$$

where $\tilde{f}_\alpha$ represents the post-collision state.

Two lattice models are used in this Thesis: the $D2Q9$ and $D3Q19$ models. For simplicity, the following description applies to the two-dimensional case ($D2Q9$). The details of the $D3Q19$ model can be found in Appendix B.

The set of velocities for $D2Q9$ is (see Fig. 1.1):

$$e_{i\alpha}^{D2Q9} = \begin{pmatrix} 0 & 1 & 0 & -1 & 0 & 1 & -1 & -1 & 1 \\ 0 & 0 & 1 & 0 & -1 & 1 & 1 & -1 & -1 \end{pmatrix}\ . \tag{1.5}$$

Moments for this model are: $m_\alpha = (\rho, e, \epsilon, j_x, q_x, j_y, q_y, p_{xx}, p_{xy})^\mathsf{T}$. The only macroscopic conserved variables of the flow field are: density, $\rho = \rho_0 + \delta\rho$, where ρ_0 is a constant density, and $\delta\rho$ the density variation; and momentum, $(j_x, j_y) = (\rho_0 u, \rho_0 v)$, which are obtained by integrating the distribution function f_α over the velocity space:

$$\rho = \sum_\alpha f_\alpha\ ; \tag{1.6a}$$

$$\rho_0 u_i = \sum_\alpha e_{i\alpha} f_\alpha\ ; \tag{1.6b}$$

The relaxation matrix for the D2Q9 is: $S_{\alpha\beta} = diag(0, s_e, s_\epsilon, 0, s_q, 0, s_q, s_\nu, s_\nu)$; and

the transformation matrix is:

$$M_{\alpha\beta} = \begin{pmatrix} 1 & 1 & 1 & 1 & 1 & 1 & 1 & 1 & 1 \\ -4 & -1 & -1 & -1 & -1 & 2 & 2 & 2 & 2 \\ 4 & -2 & -2 & -2 & -2 & 1 & 1 & 1 & 1 \\ 0 & 1 & 0 & -1 & 0 & 1 & -1 & -1 & 1 \\ 0 & -2 & 0 & 2 & 0 & 1 & -1 & -1 & 1 \\ 0 & 0 & 1 & 0 & -1 & 1 & 1 & -1 & -1 \\ 0 & 0 & -2 & 0 & 2 & 1 & 1 & -1 & -1 \\ 0 & 1 & -1 & 1 & -1 & 0 & 0 & 0 & 0 \\ 0 & 0 & 0 & 0 & 0 & 1 & -1 & 1 & -1 \end{pmatrix} . \tag{1.7}$$

The equilibrium moments for non-conserved quantities are the following [24]:

$$e^{eq} = -2\rho + 3\rho_0(u^2 + v^2) \,, \tag{1.8a}$$

$$\epsilon^{eq} = \rho - 3\rho_0(u^2 + v^2) \,, \tag{1.8b}$$

$$q_x^{eq} = -\rho_0 u \,, \tag{1.8c}$$

$$q_y^{eq} = -\rho_0 v \,, \tag{1.8d}$$

$$p_{xx}^{eq} = \rho_0(u^2 - v^2) \,, \text{ and} \tag{1.8e}$$

$$p_{xy}^{eq} = \rho_0 uv \,. \tag{1.8f}$$

The equilibrium distribution functions f_α^{eq} equivalent to the previous equilibrium moments have the form:

$$f_\alpha^{eq} = w_\alpha \left\{ \rho + \rho_0 \left[\frac{1}{c_s^2}(e_{i\alpha}u_i) + \frac{1}{2c_s^4}\left((e_{i\alpha}u_i)^2 - c_s^2 u_i u_i\right) \right] \right\} \,, \tag{1.9}$$

where c_s is the sound speed, and the weighting factors w_α are: $w_0 = 4/9$, $w_{1-4} = 1/9$, and $w_{5-8} = 1/36$. Both Eq. (1.8) and (1.9) are the so called *incompressible* form [26, 27], where the density is split as $\rho = \rho_0 + \delta\rho$ and the $\delta\rho u_i$ and $\delta\rho u_i^2$ terms are discarded.

1.1.2 From lattice Boltzmann to Navier-Stokes

The macroscopic equations recovered from a particular lattice Boltzmann method can be obtained by means of asymptotic analysis. There exist several types of asymptotic analysis that can be applied to the lattice Boltzmann method. For most cases they are essentially equivalent; however, depending on the specific application or on the complexity of the LB method, one of them can be preferred over the others. The following expansions can be used to recover the macroscopic equations:

- The *Hilbert*, or regular asymptotic, expansion has been proposed by Junk et al. [16] for LB methods, and previously used in the context of kinetic theory [2]. It is based on a diffusive scaling that leads to the recovering of the system of incompressible Navier-Stokes equations. It provides order-by-order information about the numerical solution of the LB methods, which allows to analyze the structure of the leading order errors and the accuracy of numerically derived quantities.

- The *Chapman-Enskog* expansion [1] is the most commonly used one. It is based on an expansion of the velocity distribution functions and time in powers of a small parameter related to the Knudsen number. The leading set of equations derived are: first, the Euler system (related to the convective temporal scaling); second, the Navier-Stokes system (related to the diffusive temporal scaling); and so on (e.g. the third set of equations is the Burnett system).

- The use of *Grad* moments in conjunction with some proper scaling and recursive substitutions has also been proposed to be used for the analysis of the lattice Boltzmann method [28], based on a recent asymptotic method for kinetic theory [29]. This method allows to directly work at the level of the moment equations.

Further details and discussions about asymptotic analyses in kinetic theory can be found in Refs. [2, 18, 19].

To recover the equivalent macroscopic equations, the Chapman-Enskog expansion is used here. This is so for two reasons: (i) we are mainly interested in the application of lattice Boltzmann methods within the continuum limit, and the Chapman-Enskog expansion is the preferred route to recover the Navier-Stokes equations; and (ii) the compressible nature of the method is relevant for the new approaches proposed in this Thesis. By employing the Chapman-Enskog procedure on the lattice Boltzmann equation, the Navier-Stokes continuity and momentum equations are derived (see

Appendix C):

$$\frac{\partial \rho}{\partial t} + \rho_0 \frac{\partial u_i}{\partial x_i} = 0 \,, \tag{1.10a}$$

$$\rho_0 \frac{\partial u_i}{\partial t} + \rho_0 u_j \frac{\partial u_i}{\partial x_j} = -\frac{\partial p}{\partial x_i} + \frac{\partial}{\partial x_j}\left(\rho_0 \nu \left(\frac{\partial u_j}{\partial x_i} + \frac{\partial u_i}{\partial x_j} - \frac{2}{3}\frac{\partial u_k}{\partial x_k}\right)\right) + \frac{\partial}{\partial x_j}\left(\lambda\left(\delta_{ij}\frac{\partial u_k}{\partial x_k}\right)\right) \,. \tag{1.10b}$$

The speed of sound for the $D2Q9$ model (also for the $D3Q19$ one) is $c_s = 1/\sqrt{3}$; and, for pressure, an equation of state for ideal gases is derived: $p = \rho c_s^2$. The kinematic viscosity in the Navier-Stokes equations is related to the relaxation coefficient s_ν by the equation: $\nu = 1/3(1/s_\nu - 1/2)$. Since viscosity is positive, $1/s_\nu > 1/2$ is required as a stability condition. Among the remaining relaxation parameters, those related to the conserved quantities have no influence on the flow; thus, $s_\rho = s_\chi = 0$. Due to athermal compressibility, a bulk viscosity of the flow appears, $\zeta = \lambda + \frac{2}{3}\mu$, which is defined by the s_e relaxation parameter: $\zeta = 1/6(1/s_e - 1/2)$, being λ the second viscosity coefficient, and μ the dynamic viscosity. The relaxation parameter s_q is related to the exact location of walls referring to the last fluid node; a relation between s_q and s_ν is selected in such a way that the error associated to this location is minimized [30, 31].

Considering not the Knudsen number (which is the relation between the mean free path and the characteristic length) $Kn \to 0$, the only two dimensionless numbers which define the flow are the Mach number:

$$Ma = \frac{u_0}{c_s} \,, \tag{1.11}$$

which must fulfill $Ma < 0.3$ to be within the incompressible limit; and the Reynolds number:

$$Re = \frac{u_0 L}{\nu} \,; \tag{1.12}$$

being $L = N\delta x$ the characteristic length, N the number of lattice points in the characteristic length, δx the lattice spacing, and u_0 a reference velocity of the flow.

The lattice timing δt and spacing δx determine the lattice dimensions. In this Thesis they are always $\delta t = \delta x = 1$. As different units than in the real world are used, to compare results between lattice Boltzmann simulations and real measurements it must be done through normalized variables and dimensionless numbers.

It is possible to recover the single-relaxation-time (SRT) collision operator, also called BGK after its authors [32], by selecting the same value for all relaxation parameters: $s_e = s_\epsilon = s_q = s_\nu = 1/\tau_s$. This leads to the SRT evolution equation described by

Qian et al. [15]:

$$f_\alpha(x_i + e_{i\alpha}\delta t, t + \delta t) - f_\alpha(x_i, t) = -\frac{1}{\tau_s}[f_\alpha(x_i, t) - f_\alpha^{eq}(x_i, t)] \ ; \tag{1.13}$$

where, now, τ_s is the only relaxation factor, and it applies to all the dependences described above; therefore, with this collision operator it is not possible to define separately the shear and bulk viscosity and neither it is possible to fix arbitrarily the wall location in relation to the neighboring lattice nodes.

1.2 Basic boundary conditions

When fluid flow is simulated with lattice Boltzmann methods it is necessary to specify a value for each f_α at the boundaries. The velocity distribution functions can be specified, as a first approach, from the conserved macroscopic variables, u and ρ, through the equilibrium distribution function Eq. (1.9). To complete the non-equilibrium part of the distribution function additional information is required, which can be obtained from the derivatives of the macroscopic variables or from the distribution functions themselves, as detailed below.

The boundary treatments in LB methods may be conveniently classified from a physical point of view as: *hydrodynamic*, when they are primarily based on the specification of macroscopic variables; or *kinetic*, when are based on a set of wall-collision rules for the distribution functions. Moreover, hydrodynamic boundary conditions may be classified according to the following expression [33]:

$$\mathrm{w}_1 u_i + \mathrm{w}_2 \frac{\partial u_i}{\partial r} = \mathrm{w}_3 \ . \tag{1.14}$$

(Boundary conditions for velocity are used to illustrate the description; however the definitions are valid for any other variable.) Thus, boundary conditions are defined as:

- **Dirichlet**, when the speed of the fluid u_i is imposed ($\mathrm{w}_2 = 0$).
- **Neumann**, when derivatives of the velocity $\partial_j u_i$ are known at the boundary ($\mathrm{w}_1 = 0$).
- **Robin**, when a relation between Dirichlet and Neumann conditions are defined for a boundary ($\mathrm{w}_1 \neq 0$ and $\mathrm{w}_2 \neq 0$). The case $u_i = K\partial_j u_i$ ($\mathrm{w}_3 = 0$ and K =-$\mathrm{w}_2/\mathrm{w}_1$) will be studied in this work, with K a constant free parameter related to the slip length; and
- **Mixed**, when the same surface has different boundary conditions in different regions.

There are, nevertheless, other possible classifications. For example, from an implementation perspective, boundary conditions for LB can be: link-based, volumetric, extrapolated, immersed, or local. On the other hand, boundary conditions for fluid flow may be classified using their physical function, for instance as wall or open boundary conditions. Further descriptions of these approaches are given in Chapters 2 and 3.

In the following, a brief overview is presented of the basic and most common initial and boundary conditions used in lattice Boltzmann methods for hydrodynamics simulations: first, the treatment of initial conditions is described; second, three options to impose Dirichlet velocity and pressure boundary conditions, both in walls or in open boundaries are detailed; and, finally, some considerations about special treatments for open boundaries are discussed.

1.2.1 Initial conditions

A first approach to compute the initial values for the distribution functions is approximate them to the equilibrium distributions function values, Eq. (1.9), $f_\alpha(t=0) = f_\alpha^{eq}(\rho_0, \mathbf{u})$; where initial fields are, typically, constant (or somehow specified) density ρ_0 or, equivalently, pressure and velocity u_0 fields. Density and velocity can be also interpolated from solutions of other grid resolutions (e.g. results of Sec. 2.3.1). This approximation is indeed acceptable for steady or unsteady periodical flows, but if the initial starting point is relevant in the simulation, improved approaches must be used. When the values for the non-equilibrium distribution functions are not specified, the initial error (in the form of Knudsen layers [34]) is propagated through the domain and deteriorates the unsteady solution.

To obtain second order initial values for the distribution functions in the whole domain two different methods can be applied. The first one is based on the construction of the distribution function as $f_\alpha = f_\alpha^{eq} + f_\alpha^{neq}$, the non-equilibrium part being computed using density and velocity derivatives [35] to complete expressions for f_α^{neq} derived from the Chapman-Enskog expansion. The second approach consists in the numerical computation of the distribution functions by running the collision-propagation algorithm with freezing initial macroscopic conditions [34, 36, 37].

1.2.2 Dirichlet conditions

Usually, the Dirichlet velocity condition is used for inlets and walls, and the Dirichlet pressure condition for outlets. Three different schemes are described below for the implementation of this set of conditions. (See Fig. 1.2.)

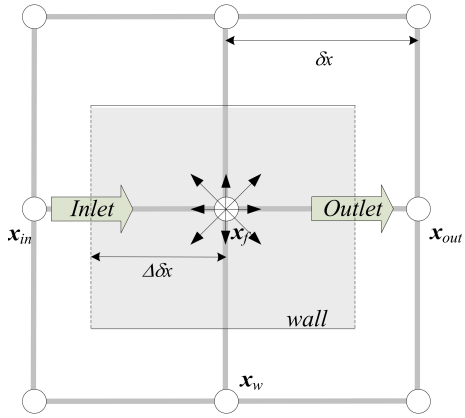

Figure 1.2: Minimal representation of a channel. Boundaries of the fluid domain (grey area) are typically halfway between fluid and boundary nodes (walls or open boundaries).

Equilibrium boundary conditions

When equilibrium boundary conditions are used (this is a first order approach), the distribution functions at inlets (or walls) are computed as:

$$\tilde{f}_\alpha(\mathbf{x}_{in}) = f_\alpha^{eq}(\rho(\mathbf{x}_{in} + \delta x), u_0)\,; \tag{1.15}$$

and similarly at the outlet:

$$\tilde{f}_\alpha(\mathbf{x}_{out}) = f_\alpha^{eq}(\rho_0, u(\mathbf{x}_{out} - \delta x))\,. \tag{1.16}$$

Bounce-back method

For solid walls (Dirichlet velocity condition with $u_i = 0$), the most widely used conditions are based on bounce-back methods. The standard bounce-back method consists in reflecting at the collision step the distribution functions moving from a fluid node $\mathbf{x}_f$ to a solid one $\mathbf{x}_w$ in the opposite direction: $\tilde{f}_\alpha(\mathbf{x}_w) = \tilde{f}_{\bar{\alpha}}(\mathbf{x}_f)$, where the bar over α indicates the opposite direction to α, and $\tilde{f}_\alpha$ is the post-collision distribution function. This simple bounce-back method can be considered as a particular case of link-based techniques, which allows to place the wall at an arbitrary location between two nodes [30, 31, 38]. When a velocity different from $u_i = 0$ want to be imposed, the modification by Bouzidi et al. [38] is the first approach (also called in this Thesis velocity bounce-back, UBB):

$$\tilde{f}_\alpha(\mathbf{x}_w) = \tilde{f}_{\bar{\alpha}}(\mathbf{x}_f) - 2\omega_\alpha \rho_0 c_s^2 (e_{i\alpha} u_i)\,; \tag{1.17}$$

Further description of extended bounce-back methods, and how to apply them to impose Dirichlet velocity and pressure conditions, can be found in Chapter 3.

Zou boundary conditions

In the open boundary condition by Zou and He [39], the speed u_0 is fixed at the inlet (and the density ρ_0 at the outlet); the density (and the velocity) is computed by solving the system $\rho = \sum_\alpha f_\alpha$, and $\rho \mathbf{u} = \sum_\alpha \mathbf{e}_\alpha f_\alpha$; and the non-equilibrium part is calculated taking into account the following relation: $f_\alpha^{neq} = f_{\bar{\alpha}}^{neq} = f_{\bar{\alpha}} - f_{\bar{\alpha}}^{eq}$. The following expression for the inlet condition results:

$$\tilde{f}_\alpha(\mathbf{x}_{in}) = f_\alpha^{eq}(\rho(u_0), u_0) + (\tilde{f}_{\bar{\alpha}} - f_{\bar{\alpha}}^{eq}) \,; \tag{1.18}$$

and for the outlet:

$$\tilde{f}_\alpha(\mathbf{x}_{out}) = f_\alpha^{eq}(\rho_0, u(\rho_0)) + (\tilde{f}_{\bar{\alpha}} - f_{\bar{\alpha}}^{eq}) \,. \tag{1.19}$$

1.2.3 Open boundaries

Possible pairs of inflow-outflow boundary conditions for isothermal lattice Boltzmann simulations of fluid flow can roughly classify in three groups: (a) fixed velocity at inlet and fixed density at outlet; (b) fixed velocity at inlet and some kind of zero gradient at outlet; and (c) non-reflecting modifications of the boundary conditions of type (a). For group (a) the Dirichlet conditions, introduced in Sec. 1.2.2, are used; for group (b) a possible approach is described below; and for group (c) see Chap. 2.

Yu boundary conditions

Yu et al. [40] set the reference velocity and density at the inlet through the equilibrium distribution function and reflect the non-equilibrium part:

$$\tilde{f}_\alpha(\mathbf{x}_{in}) = f_\alpha^{eq}(\rho_0, u_0) + (\tilde{f}_{\bar{\alpha}} - f_{\bar{\alpha}}^{eq}) \,; \tag{1.20}$$

At the outlet a convective condition for f_α is fixed, $\partial_t f_\alpha + e_{i\alpha} \partial_i f_\alpha = 0$, which can be approximated by the following implementation:

$$\tilde{f}_\alpha(\mathbf{x}_{out}) = \tilde{f}_\alpha(\mathbf{x}_{out} - \mathbf{e}_\alpha \delta t) \,. \tag{1.21}$$

This scheme is expected to behave approximately as other outflow boundary conditions with zero gradients at the outlet. For further discussion see Ref. [41].

As formulated here, for this boundary condition at the inlet $\rho_0 u_0$ is fixed, but not ρ_0 and u_0 separately; the actual values for ρ and $\mathbf{u}$ are subsequently determined from the calculation.

1.3 Stability analysis

When new lattice Boltzmann methods are built it is important to ascertain their stability limits, as stability is arguably the most important restriction when real flows are simulated with LB methods. For this purpose linear stability analyses are performed in this work, which are intended to be a screening tool to aid for the design of new methods (see Chapter 5).

Linear-stability, or von Neumman, analysis is a standard tool to study the stability of linear and linearized systems, and has been used previously to study the stability of lattice Boltzmann methods [42], and to optimally construct new lattice Boltzmann models [24].

It is well known that all lattice Boltzmann models have stability limits [42]. The general stability behavior is as follows: (i) The relaxation time τ_s (with the SRT collision operator) must be grater than one-half; (ii) the mean flow speed must be smaller than a maximum stable one that is function of the other parameters; and (iii) as τ_s increases from one-half, the maximum stable speed increases monotonically until a limit is reached. Often, the high Reynolds numbers encountered in real applications bring the method close to its stability limits, viz., a relaxation factor very close to one-half and mean speed greater than the maximum stable one.

To perform the von Neumman linearized stability analysis we restrict ourselves to a steady flow, in two dimensions, with constant density ($\rho_0 = 1$), velocity $\mathbf{u}_0 = (u_0, 0)$ and wave numbers $\mathbf{k} = (k_x, 0)$ parallel to the constant velocity $\mathbf{u}_0$. These settings provide the worst stability conditions [42] (see [43] for further discussion). Non-linear terms are also included with a linearization about global equilibrium values. Earlier stability analyses of lattice Boltzmann methods, where non-linear terms are not taken into account, can be found in Ref. [8]. Thus, taking into account the non-linear terms, the distribution function may be expressed as its equilibrium value and a small superimposed fluctuation:

$$f_\alpha(x_i, t) = f_\alpha^{eq} + \delta f_\alpha(x_i, t) \,. \tag{1.22}$$

This formulation implies that f_α^{eq} have constant values, which do not vary neither in space nor in time, and depend only on ρ_0 and u_0. Fluctuating quantities $\delta f_\alpha(x_i, t)$ differ from the non-equilibrium values of f_α because the linearization around equilibrium is based on mean values.

Combining Eq. (1.2) and Eq. (1.22) with the equilibrium moments of Eq. (1.8) a linearized lattice Boltzmann equation for the fluctuations is obtained:

$$\begin{aligned} \delta f_\alpha(x_i + e_{i\alpha}\delta t, t + \delta t) &= \delta f_\alpha(x_i, t) + \Omega_\alpha^{eq} \delta f_\alpha(x_i, t) = \\ &= \delta f_\alpha(x_i, t) + M_{\alpha\beta}^{-1} C_{\alpha\beta} M_{\alpha\beta} \delta f_\alpha(x_i, t) \,. \end{aligned} \tag{1.23}$$

The last term is the linearized collision operator, where $C_{\alpha\beta}$ can be expressed as:

$$C_{\alpha\beta} = \frac{M_{\beta\gamma}M_{\beta\delta}}{M_{\alpha\gamma}M_{\alpha\delta}}\frac{\partial\Delta m_\alpha}{\partial m_\beta}\,. \tag{1.24}$$

Here, $\partial\Delta m_\alpha/\partial m_\beta$ is the variation of moments due to collision. Using the collision formulation of Eq. (1.2), this variation can be expressed as:

$$G_{\alpha\beta} := \frac{\partial\Delta m_\alpha}{\partial m_\beta} = -S_{\alpha\beta}\delta_{\alpha\beta} + S_{\alpha\beta}\delta_{\alpha\beta}\frac{\partial\Delta m_\alpha^{eq}}{\partial m_\beta}\,. \tag{1.25}$$

For the D2Q9 model the following matrix is obtained:

$$G_{\alpha\beta} = \begin{pmatrix} 0 & 0 & 0 & 0 & 0 & 0 & 0 & 0 & 0 \\ -2s_e & -s_e & 0 & 6s_e u_0 & 0 & 6s_e v_0 & 0 & 0 & 0 \\ s_\epsilon & 0 & -s_\epsilon & -6s_\epsilon u_0 & 0 & -6s_\epsilon v_0 & 0 & 0 & 0 \\ 0 & 0 & 0 & 0 & 0 & 0 & 0 & 0 & 0 \\ 0 & 0 & 0 & -s_q & -s_q & 0 & 0 & 0 & 0 \\ 0 & 0 & 0 & 0 & 0 & 0 & 0 & 0 & 0 \\ 0 & 0 & 0 & 0 & 0 & -s_q & -s_q & 0 & 0 \\ 0 & 0 & 0 & 2s_\nu u_0 & 0 & -2s_\nu v_0 & 0 & -s_\nu & 0 \\ 0 & 0 & 0 & s_\nu v_0 & 0 & s_\nu u_0 & 0 & 0 & -s_\nu \end{pmatrix}. \tag{1.26}$$

In Fourier space, Eq. (1.23) can be expressed as:

$$A_{\alpha\beta}\delta f_\alpha(k_i, t+1) = \left[\delta_{\alpha\beta} + M^{-1}_{\alpha\beta}C_{\alpha\beta}M_{\alpha\beta}\right]\delta f_\alpha(k_i, t)\,, \tag{1.27}$$

where $A_{\alpha\beta} = -exp(ie_{i\alpha}k_i)\delta_{\alpha\beta}$ is the advection operator. Therefore, the evolution equation may be rewritten in this form: $\delta f_\alpha(k_i, t+1) = L_{\alpha\beta}\delta f_\alpha(k_i, t)$, with the following expression for the linearized evolution operator:

$$L_{\alpha\beta} = A_{\alpha\beta}[\delta_{\alpha\beta} + M^{-1}_{\alpha\beta}C_{\alpha\beta}M_{\alpha\beta}]\,. \tag{1.28}$$

The linear stability analysis performed in this work is based on the value of the maximum eigenvalue of the linearized evolution operator $L_{\alpha\beta}$,

$$\lambda_{max} = \text{Max. Eigenvalue}[L_{\alpha\beta}(k_i)]\,,$$

which must be less than one for the system to be stable. It has been computed numerically with *Mathematica* [44].

2

Non-Reflecting Open Boundaries

2.1 Introduction

Open boundaries are an essential feature of practical fluid flow computations. In lattice Boltzmann methods, although a significant research effort has been made to characterize the accuracy of different boundary-condition implementations [16, 30, 31], little attention has been paid so far to the study of the interaction of these open boundaries with the fluid domain; some exceptions are the work by Yu et al. [40] and by Yang [41]. It has been extensively shown that the choice of initial and boundary conditions influence the accuracy of the method [16, 36]. However, even if the spurious behavior of these conditions in the form of small numerical waves (wiggles) and initial layers is suppressed, it is still necessary to formulate a mechanism to treat the physical waves generated in the bulk of the fluid. In fact, research in numerical methods for compressible fluid flow computations over the last 30 years has shown that the typical boundary conditions employed are reflective and they may have a significant influence on the solution of unsteady compressible flows even at low Mach and Reynolds numbers [45].

When solving the fluid-flow equations with compressible solvers, the presence of open boundaries close to the zones where vortices or pressure waves are generated requires a mechanism for modeling the far field environment, so that the truncation of the physical domain does not bear an influence on the simulated processes. The correct truncation of the domain becomes a more serious problem for complex flows, e.g. turbulent combustion with acoustic coupling [46]. Additionally, this problem is related to the well-posedness of the boundary conditions. And, further, it is necessary

to guarantee not only a good behavior in terms of wave suppression, but also the preservation of the order of the method [45].

Some solutions have been proposed to address this source of error in classical CFD approaches [47]. In lattice Boltzmann methods, the most popular boundary-condition implementations have indeed a reflecting nature, as they entail that part of the numerical information reaching the boundary is reflected back to the inside of the computational domain. A thorough comparison of different boundary conditions for lattice Boltzmann methods will help select the most appropriate ones among those commonly used; and it can help determine if more classical CFD solutions [47] should be ported to lattice Boltzmann.

Previous work on the analysis of open boundaries in LB methods [41] is based on the recovery of the incompressible Navier-Stokes equations, instead of being based on the compressible NS equations. This has a substantial influence on the definition of the inlet and outlet boundary condition. Consequently, here the study of open boundaries starting with the assumption that the flow is compressible, although only slightly since simulations are allways within the incompressible limit ($Ma < 0.3$). Additionally, the analysis presented here is for low-Reynolds-number simulations, but the motivation for studying such phenomenon is even greater in flows at high Reynolds numbers. Indeed, higher Reynolds numbers involve smaller relaxation times and, consequently, numerical perturbations may not be easily dampened. The presence of unphysical pressure waves becomes a more critical issue in this situation [48].

With the aim of performing an analysis of the effects of the interaction between the open boundaries and the fluid domain, the confined unsteady flow past a square cylinder is selected as the main benchmark case, with other simpler additional test cases being used as well. The square-cylinder case exhibits some properties that make it very suitable for the purpose of the present analysis. The fact that all boundary planes (inlet, outlet, lateral walls and square cylinder walls) are either parallel or perpendicular to the main flow direction significantly simplifies the analysis; and the continuous vortex shedding generates periodic pressure waves, which makes it a very challenging problem for non-reflecting boundaries. Moreover, results of previous simulations of this test case with the lattice Boltzmann method and with the finite volume method are available in the literature [49] used as reference data.

The techniques for artificial boundary modeling may be classified into two main groups [47]: characteristic boundary conditions and absorbing layers. It is intended that some of these techniques should be applied for most of the simulations with LB methods, including those in which it is desired to recover the incompressible solution.

This Chapter is organized as follows: first two different artificial boundary conditions are proposed, one based on density filtering and the other one based on Euler characteristics. Then the filtering condition is used to analyze the influence of pressure waves and open boundary conditions in unsteady periodic simulations; and the char-

acteristic boundary condition is studied to evaluate the degree of wave-interaction suppression.

2.2 Non-reflecting proposals

Two different non-reflecting boundary conditions are presented: the first one is only valid for steady-state Dirichlet conditions for velocities and is based on the temporal filtering of the density; the second one is valid for Dirichlet (and Neumann, see Chapter 3), steady and unsteady boundaries for density and velocity, and is based on the analysis of information traveling through Euler characteristics.

2.2.1 Density-filtering: formulation

A non-reflecting boundary condition for steady-state Dirichlet conditions for velocities is presented as a simplified example of an absorbing layer. This boundary condition has been previously used by the author to simulate turbulent flows [48]. It is appropriate for boundary conditions in which density at the inlet is extrapolated or calculated with the known distribution functions [39, 50] and the velocity is fixed. In this scheme, the density is filtered in order to reduce the effect of pressure waves that reach the inlet.

The proposed scheme involves filtering the density in time with a low-pass filter, so that the high frequencies are dampened and only gradual changes in the density at the inlet are allowed. A first-order low-pass filter is proposed due to its simplicity. It can be expressed in terms of Fourier transform as:

$$\bar{F}(i\omega) = \frac{1}{1 + i\omega T_c} \; ; \tag{2.1}$$

where T_c is the time period associated with the cutoff frequency $\omega_c = 2\pi/T_c$.

When the filter, Eq. (2.1), is applied, the scheme becomes:

$$\bar{\rho}_{in}(i\omega) = \bar{F}(i\omega)\bar{\rho}_e(i\omega) = \frac{1}{1 + i\omega T_c}\bar{\rho}_e(i\omega) \; ; \tag{2.2}$$

where ρ_{in} is the density at inlet (where the velocity is set), ρ_e is the extrapolated value of the density, and the bar over the function symbols indicates that they are expressed in the Fourier space.

In the temporal domain, a differential equation is obtained:

$$\rho_{in} + T_c \frac{d\rho_{in}}{dt} = \rho_e \; . \tag{2.3}$$

Finally, and approximating the time derivative with a first-order-upwind finite-difference expression, a new equation to calculate the filtered density at the inlet $\bar{\bar{\rho}}_{in}$ at time step n is obtained:

$$\bar{\bar{\rho}}_{in} = \rho^n_{in} = \frac{\rho^n_e + T_c \rho^{n-1}_{in}}{1 + T_c} \; ; \tag{2.4}$$

where the double overbar indicates temporal filtering.

In order to assign an appropriate value to T_c, several aspects should be considered. Firstly, the value of T_c determines the capacity of the filter to dampen the undesired frequencies. These undesired frequencies may be related to a characteristic frequency in the domain, defined through a characteristic length L and a characteristic velocity u_0. The cutoff frequency should be smaller than this characteristic frequency in order to ensure the filtering of higher frequencies:

$$\omega_c < 2\pi u_0 / L \; . \tag{2.5}$$

Secondly, the response time of the scheme needs also be taken into account. It is well known through systems theory [51] that a first order system, as the one proposed, has a response time of approximately $t_r \simeq 3T_c$, the response time being defined as the time taken to react to a step in the input and achieve a value within 5% of the step. In the case of the inlet density, this means that given an abrupt change in density $\Delta\rho$ in the neighborhood of the inlet and ignoring any other influence, the difference between the value of the density at the inlet and the value in the neighboring nodes would be smaller than 5% of $\Delta\rho$ after $3T_c$ temporal steps (note that here time is equivalent to the number of temporal steps, expressed in lattice units). It is advisable to make the total time of a simulation at least a number of times the response time, so as to assure the convergence to the inlet density value after any changes produced in the density during a simulation. Thus $t_{max} > 10t_r$ is used.

Compiling these considerations, an indicative range of appropriate values for T_c can be given:

$$\frac{L}{u_0} < T_c < \frac{t_{max}}{30} \; . \tag{2.6}$$

It should be noted that all these variables are expressed in the dimensionless lattice units.

2.2.2 Density-filtering: implementation

In this Chapter, the filtering scheme will be applied to the Equilibrium and to the Zou boundary condition at inlet (Section 1.2.2). As the boundary inflows considered must be steady for this filtering to be applicable, Zou's modified inlet condition can be expressed as:

$$\tilde{f}_\alpha(\mathbf{x}_i) = f^{eq}_\alpha(\bar{\bar{\rho}}(u_0), u_0) + (\tilde{f}_{\bar{\alpha}} - \tilde{f}^{eq}_{\bar{\alpha}}) \; ; \tag{2.7}$$

2.2.3 Characteristic boundary conditions: formulation

In this Section a formulation of a characteristic boundary condition for the standard LB method [15] is proposed, which is based on the characteristics of the Euler equations and their extension to the Navier Stokes ones; these are the so-called Navier-Stokes Characteristic Boundary Condition (NS-CBC), developed by Poinsot and Lele [45].

For simplicity the characteristic boundary conditions for LB are presented for two-dimensions (MRT $D2Q9$). The extension to three dimensions and the use of other collision operators do not need additional considerations. Slightly modified equilibrium moments are used:

$$e^{eq} = -2(2-\kappa)\rho + \rho_0(u^2+v^2)\,, \tag{2.8a}$$

$$\epsilon^{eq} = \rho + \rho_0(u^2+v^2)\,, \tag{2.8b}$$

$$q_x^{eq} = -\rho_0 u\,, \tag{2.8c}$$

$$q_y^{eq} = -\rho_0 v\,, \tag{2.8d}$$

$$p_{xx}^{eq} = \rho_0(u^2-v^2)\,, \text{ and} \tag{2.8e}$$

$$p_{xy}^{eq} = \rho_0 uv\,; \tag{2.8f}$$

where κ is the specific-heat ratio. The derivation of the Navier-Stokes system equivalent to the LB one is made through a Chapman-Enskog expansion in the low-Knudsen number and low-Mach-number limit. The resulting speed of sound c_s is:

$$c_s = \sqrt{\kappa RT} = \sqrt{\kappa\frac{p}{\rho}}\,; \tag{2.9}$$

where κ takes the value of 1 for the D2Q9 method [24], and therefore $c_s^2 = 1/3$. The transport coefficients are related to the relaxation factors, and thus the shear and bulk viscosity are respectively:

$$\nu = \frac{1}{3}\left(\frac{1}{s_\nu} - \frac{1}{2}\right)\,; \text{ and} \tag{2.10}$$

$$\zeta = \frac{2-\kappa}{6}\left(\frac{1}{s_e} - \frac{1}{2}\right)\,. \tag{2.11}$$

A minimal working scheme of the NS-CBC is formulated for LB based on the same procedure followed in the original work [45]. The goal is to derive non-reflective Dirichlet boundary conditions for both the velocity and the pressure. A non-reflective Dirichlet pressure condition can be used as the far-field boundary condition usually applied in compressible fluid-flow simulations. The local one-dimensional inviscid (LODI) equations expressed in primitive variables $\mathbf{U} = (\rho, u, v, E)$ are solved at the boundary. These are the Euler equations without the transverse terms; for an open boundary normal to the x direction these are:

$$\frac{\partial \rho}{\partial t} + u\frac{\partial \rho}{\partial x} + \rho\frac{\partial u}{\partial x} = 0\,; \tag{2.12a}$$

$$\frac{\partial u}{\partial t} + u\frac{\partial u}{\partial x} + \frac{1}{\rho}\frac{\partial p}{\partial x} = 0\,; \tag{2.12b}$$

$$\frac{\partial v}{\partial t} + u\frac{\partial v}{\partial x} = 0\,; \tag{2.12c}$$

$$\frac{\partial \rho E}{\partial t} + \frac{\partial \left[u(\rho E + p)\right]}{\partial x} = 0\,. \tag{2.12d}$$

It should be noticed that the energy equation is included here for consistency, but the LB model is athermal; the consequences of this are discussed below. Expressing the LODI equations in vector form results in:

$$\frac{\partial}{\partial t}\mathbf{U} + \mathbf{\Gamma}_x\frac{\partial}{\partial x}\mathbf{U} = 0\,; \tag{2.13}$$

from which the amplitude variations $\mathbf{L}$ can be computed as $\mathbf{L} = \mathbf{\Lambda}\mathbf{Q}\frac{\partial}{\partial x}\mathbf{U}$, $\mathbf{Q}$ being a matrix of left eigenvectors of $\mathbf{\Gamma}_x$ and $\mathbf{\Lambda}$ the diagonal matrix of the eigenvalues of $\mathbf{\Gamma}_x$. Therefore, the LODI relations can be rewritten in compact form as:

$$\frac{\partial}{\partial t}\mathbf{U} + \mathbf{Q}^{-1}\mathbf{L} = 0\,. \tag{2.14}$$

The resulting expressions for the amplitude variations are:

$$\mathbf{L} = \begin{Bmatrix} L_1 \\ L_2 \\ L_3 \\ L_4 \end{Bmatrix} = \begin{Bmatrix} (u - c_s)\left(\frac{\partial p}{\partial x} - \rho c_s \frac{\partial u}{\partial x}\right) \\ u\frac{\partial v}{\partial x} \\ u\left(c_s^2\frac{\partial \rho}{\partial x} - \frac{\partial p}{\partial x}\right) \\ (u + c_s)\left(\frac{\partial p}{\partial x} + \rho c_s \frac{\partial u}{\partial x}\right) \end{Bmatrix}\,; \tag{2.15}$$

Figure 2.1 shows the wave amplitude directions in each open boundary.

Considering the isothermal nature of the LB method used (the energy equation is suppressed), and using Eqs. (2.12) and (2.15) the LODI relations can be recast as:

$$\frac{\partial \rho}{\partial t} + \frac{1}{2c_s^2}\left(L_4 + L_1\right) + \frac{1}{c_s^2}L_3 = 0\,; \tag{2.16a}$$

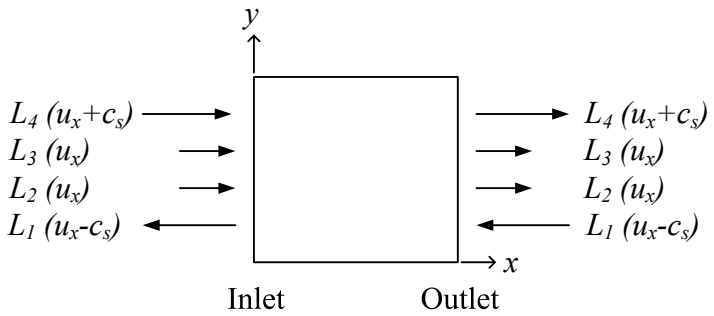

Figure 2.1: Wave amplitude variations for boundaries located on the y-axis.

$$\frac{\partial u}{\partial t} + \frac{1}{2\rho c_s}\left(L_4 - L_1\right) = 0\,; \tag{2.16b}$$

$$\frac{\partial v}{\partial t} + L_2 = 0\,. \tag{2.16c}$$

The implementation of NS-CBC in the LB equation follows the same conceptual steps as for the Navier-Stokes equations: (i) physical boundary conditions are imposed, which implies the selection of boundary conditions for the Euler equations and for the viscous terms; (ii) the wave amplitude variations $\mathbf{L}$, Eqs. (2.15), are computed; and (iii) the conservation Eqs. (2.16) are solved at the boundary using the wave amplitudes previously computed and the viscous boundary conditions.

In the third step, the adaptation of the algorithm to the LB equation requires some discussion. As a result of the isothermal compressible nature of the LB method, an artificial bulk viscosity appears which can be modulated with the relaxation factor s_e [24]; but, additionally, the non-conservation of energy prevents the pressure wave to be completely suppressed at the boundary when the pressure is specified. To correct this effect the characteristic amplitude related to the energy equation is included in the continuity LODI Eq. (2.16a).

Considering Eq. (2.9), $L_3 = 0$ for $\kappa = 1$ (which is the original value of κ in the D2Q9 lattice Boltzmann method). In Nature, the specific heat ratio takes values $\kappa > 1$ for the different gases depending of the degrees of freedom (e.g. $\kappa = 5/3$ for monoatomic gases). As κ increases, two different consequences are noteworthy: on one hand the bulk viscosity becomes smaller, and this cannot help suppress, via viscous dissipation, the excess of energy due to the isothermal character of the LB representation of the flow; on the other hand the energy-related equilibrium moment e^{eq} is modified, which approximates the scheme towards its lost thermodynamical consistency. Therefore, a tradeoff between these two behaviors is desirable. It is found numerically that using a value of $\kappa \approx 1.2$ in the boundary condition is the best for non-reflecting purposes.

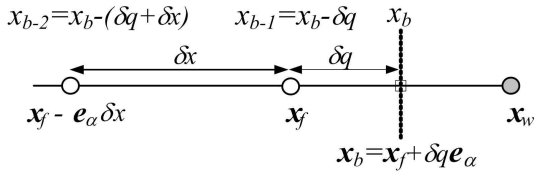

Figure 2.2: The open boundary cuts the link between $\mathbf{x}_f$ and $\mathbf{x}_w$ at δq. For the Euler equations, the values on the x-axis are considered: x_b, x_{b-1}, x_{b-2}.

Thus, this specific heat ratio is used (only in the boundary, and not within the fluid domain) to correct the behavior of the NS-CBC for LB.

2.2.4 Characteristic boundary conditions: implementation

The characteristic boundary conditions (CBC) can be applied at every boundary (inlets, outlets, walls), although the implementation details depend on boundary type. In general, the incoming wave amplitudes need to be modeled whereas the outgoing ones are computed from the LODI relations, Eq. (2.16) (see Fig. 2.1). The implementation described here is for open boundaries lying on the y-axis, with $\delta q = 1/2$ as it is the most common case. In Fig. 2.2 the nomenclature applied is shown. For link-type LB boundary-conditions the work by Ginzburg et al. [31] is followed; this reference can be used also to derive higher order extension for the boundary conditions proposed here, or to adapt them to arbitrary geometries. For the Euler equations solved at the boundary the spatial derivatives are computed in the x-direction instead of along the links. This avoids problems when dealing with corners. In the following, the implementation of the outflow far-field pressure-condition (i.e. non-reflecting Dirichlet-condition for pressure) and of the inflow non-reflecting Dirichlet-condition for velocity are detailed.

Outlet

For an outlet with $\delta q = 1/2$ where the reference pressure is fixed $p_b = p(x_b)$, the pressure anti-bounce-back (PAB) boundary condition can be applied [31]:

$$\begin{aligned} f_{\bar{\alpha}}(\mathbf{x}_f, t+1) &= -\tilde{f}_\alpha(\mathbf{x}_f, t) \\ &+ 2f_\alpha^{eq+}(\mathbf{x}_b, \hat{t}) \\ &+ (2-s_\nu)\left(f_\alpha^{+}(\mathbf{x}_f, t) - f_\alpha^{eq+}(\mathbf{x}_f, t)\right) ; \end{aligned} \tag{2.17}$$

where $\tilde{f}_\alpha$ are the post-collision distribution functions, and $\bar{\alpha}$ is the opposite direction to α. In Eq. (2.17) the first term is the anti-bounce-back, the second term is for the

Dirichlet pressure setting, and the last one is a correction to eliminate second-order error terms. The symmetric equilibrium distribution functions f_α^{eq+} are computed as:

$$f_\alpha^{eq+} = \omega_\alpha \rho + \frac{1}{2}\omega_\alpha \rho_0 c_s^{-4} \left[(\mathbf{e}_\alpha \cdot \mathbf{u})^2 - c_s^2 (\mathbf{u} \cdot \mathbf{u}) \right] . \tag{2.18}$$

When f_α^{eq+} are used for the error correction term at ($\mathbf{x}_f$,t), values are stored during the collision step to be used during boundary-condition implementation at post-collision step. The same stands for the symmetric distribution functions:

$$f_\alpha^{+} = \frac{1}{2} \left(f_\alpha + f_{\bar{\alpha}} \right) . \tag{2.19}$$

To impose the Dirichlet pressure condition, f_α^{eq+} at ($\mathbf{x}_b$,$\hat{t}$) must be computed using the desired $\rho_b = p_b c_s^{-1}$ and the actual velocity values, which are approximated as:

$$\mathbf{u}(\mathbf{x}_b, \hat{t}) \approx \mathbf{u}(\mathbf{x}_{b-1}, t) + \frac{1}{2} \left(\mathbf{u}(\mathbf{x}_{b-1}, t) - \mathbf{u}(\mathbf{x}_{b-2}, t) \right) . \tag{2.20}$$

The time $\hat{t}$ is a notional intermediate time for the conditions to be set at time t. For PAB $\hat{t} = t + 1/2$.

To introduce the CBC in the PAB scheme, alternative values must be computed at ($\mathbf{x}_b$,$\hat{t}$) for ρ and $\mathbf{u}$ according to the LODI relations. It is proceeded first by computing the outgoing wave amplitudes (L_2, L_3 and L_4) from Eq. (2.15). A second order backward stencil is used for the unknown spatial derivatives:

$$\begin{aligned} \frac{\delta \phi}{\delta x}(x_b, \hat{t} - 1) &\approx \frac{1}{3}[8\phi(x_b, \hat{t} - 1) \\ &- 9\phi(x_{b-1}, \hat{t} - 1) + \phi(x_{b-2}, \hat{t} - 1)] . \end{aligned} \tag{2.21}$$

The incoming amplitude L_1 is modeled by the means of a linear relaxation model:

$$L_1(\mathbf{x}_b, \hat{t} - 1) = k_1 (p(\mathbf{x}_b, \hat{t} - 1) - p_b) ; \tag{2.22}$$

where:

$$k_1 = \sigma_1 (1 - Ma^2) \frac{c_s}{L} , \tag{2.23}$$

being L the length between inlet and outlet. A value of $\sigma_1 = 0$ means that no information is coming into the domain; however, this does not allow to properly impose the reference pressure. To eliminate the pressure reflection and, at the same time, fix the reference pressure, σ_1 should be in the range $0.58 < \sigma_1 < \pi$ [52]. Consequently, the boundary condition becomes partially-reflective.

To explicitly solve the LODI relations at $\mathbf{x}_b$, Eqs. (2.16), a first-order time-derivative stencil is applied:

$$\rho(\hat{t}) \approx \rho(\hat{t} - 1) - \frac{\delta t}{2 c_s^2} \left(L_4(\hat{t} - 1) + L_1(\hat{t} - 1) \right) - \frac{1}{c_s^2} L_3(\hat{t} - 1) ; \tag{2.24a}$$

$$u_x(\hat{t}) \approx u_x(\hat{t}-1) - \frac{\delta t}{2\rho c_s}\left(L_4(\hat{t}-1) - L_1(\hat{t}-1)\right) \; ; \tag{2.24b}$$

$$u_x(\hat{t}) \approx u_x(\hat{t}-1) - \delta t L_2(\hat{t}-1) \; . \tag{2.24c}$$

Inlet

For an inlet where a velocity $\mathbf{u}_b$ is imposed, the velocity bounce-back boundary (UBB) condition can be applied [31]:

$$f_{\bar{\alpha}}(\mathbf{x}_f, t+1) = \tilde{f}_{\alpha}(\mathbf{x}_f, t) - 2f_{\alpha}^{eq-}(\mathbf{x}_b, \hat{t}) \; . \tag{2.25}$$

For this condition no error-correction term is needed. The anti-symmetric equilibrium function is computed as:

$$f_{\alpha}^{eq-} = \omega_{\alpha}\rho_0 c_s^{-2}(\mathbf{e}_{\alpha} \cdot \mathbf{u}) \; ; \tag{2.26}$$

where $\mathbf{u}$ is the prescribed value at ($\mathbf{x}_b$,$\hat{t}$), with $\hat{t} = t + 1/2$.

To incorporate the CBC into the UBB scheme the outgoing wave amplitude L_1 is computed from Eq. (2.15) using second-order forward spatial derivatives:

$$\begin{aligned} \frac{\delta\phi}{\delta x}(x_b, \hat{t}-1) \;&\approx\; \frac{1}{3}[-8\phi(x_b, \hat{t}-1) \\ &+\; 9\phi(x_{b-1}, \hat{t}-1) - \phi(x_{b-2}, \hat{t}-1)] \; . \end{aligned} \tag{2.27}$$

The incoming wave amplitudes (L_2, L_3 and L_4) are modeled using linear relaxation approaches as for the outlet:

$$L_i(\mathbf{x}_b, \hat{t}-1) = k_i(u(\mathbf{x}_b, \hat{t}-1) - u_b) \; ; \; \text{i=2,3,4} \tag{2.28}$$

where k_i can be computed as in Eq. (2.23), and the discussion about σ_i also holds.

2.3 Analysis of open-boundary behavior

Two different studies are performed: a first one to evaluate the behavior of open boundaries in lattice Boltzmann simulations; and a second one to demonstrate the ability of the characteristic boundary condition presented to suppress pressure waves arriving at open boundaries.

2.3.1 Vortex shedding in the wake of a square cylinder

The geometry of the domain is shown in Fig. 2.3. The relevant lengths are: $H = 8$, $L_{tot} = 52$, $L_{in} = 11.5$, and $L_{out} = 39.5$. Different grid sizes are applied, corresponding each to a parameter N, which represents the number of nodes that discretize the side of the square cylinder. The total number of nodes in the domain is $N_{tot} = L_{tot} H N^2$, and the different discretizations used in simulations are $N = 10, 20, 30, 40$ and 60. All grids are Cartesian and uniform.

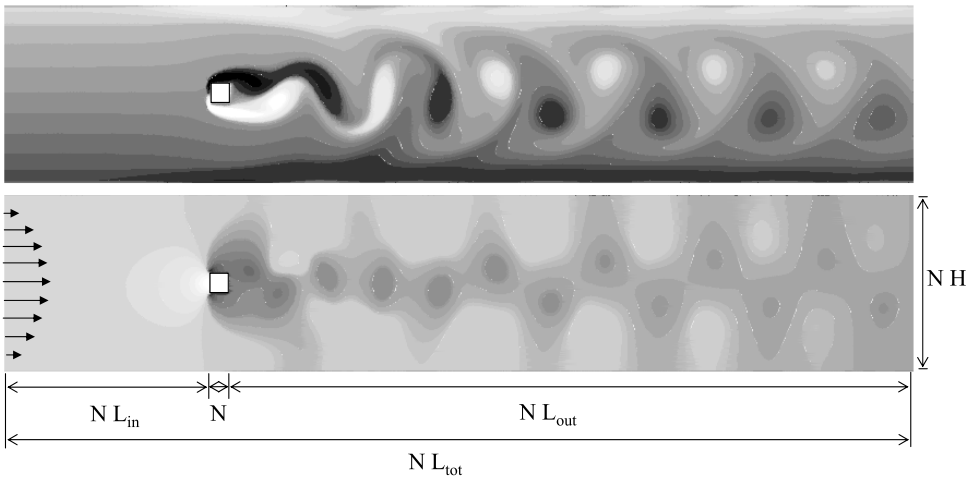

Figure 2.3: Vorticity (top) and pressure (bottom) isocontours ($Re = 100$) with Zou boundary conditions; and characteristic lengths of the computational domain.

The lateral (top and bottom) boundaries are solid walls with the no-slip boundary-condition; at the inlet, a parabolic velocity profile is imposed, whose maximum velocity at the symmetry axis is the reference velocity u_0; and, at the outlet, a reference density ρ_0 is fixed (Zou boundary condition, Sec. 1.2.2, is applied to obtain results for validation purposes in this Section).

The relevant dimensionless numbers in the flow are the Reynolds, Mach and Strouhal numbers, defined in lattice units respectively as $Re = Nu_0/\nu$ or $Re = (3Nu_0)/(\tau_s - 1/2)$; $Ma = u_0/c_s$; and $St = Nf/u_0$. In the latter expression, $f = \omega/(2\pi)$ is the characteristic frequency of the periodic flow. This frequency is dictated by the vortex shedding in the wake of the square cylinder; the shedding can be observed, for example, in the vorticity and pressure contours of the flow at $Re = 100$, Fig. 2.3. Flows with several Reynolds numbers are simulated for the present study ($Re = 65 - 200$), all of which are in the laminar and unsteady flow regime. In order to study the influence of the reference velocity u_0, the Mach number was varied ($Ma = 0.07 - 0.17$), but always kept within the incompressible range ($Ma < 0.3$).

Results presented in this Section are used as a validation for the flow considered of the lattice Boltzmann code. Time-averaged values of the drag coefficient C_d, the lift coefficient C_l and the Strouhal number St are shown. The forces over the cylinder boundaries are computed using the momentum exchange algorithm [53].

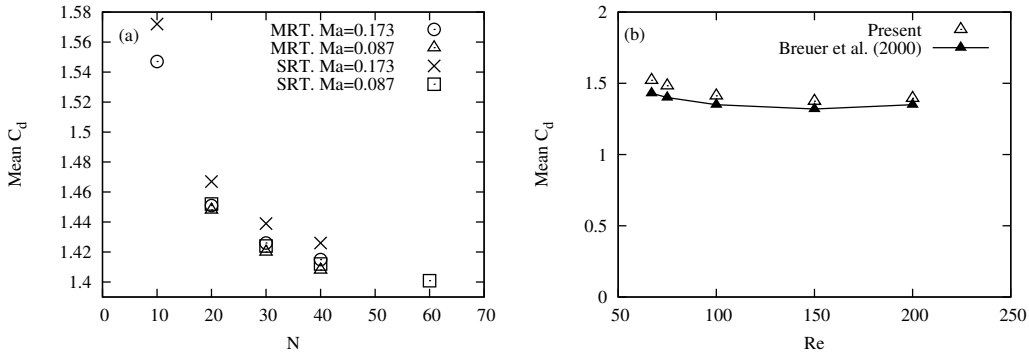

Figure 2.4: Drag coefficient values: (a) grid convergence analysis for different Mach numbers (Re=100); and (b) the evolution with the Reynolds number of the asymptotic value from the grid convergence analysis.

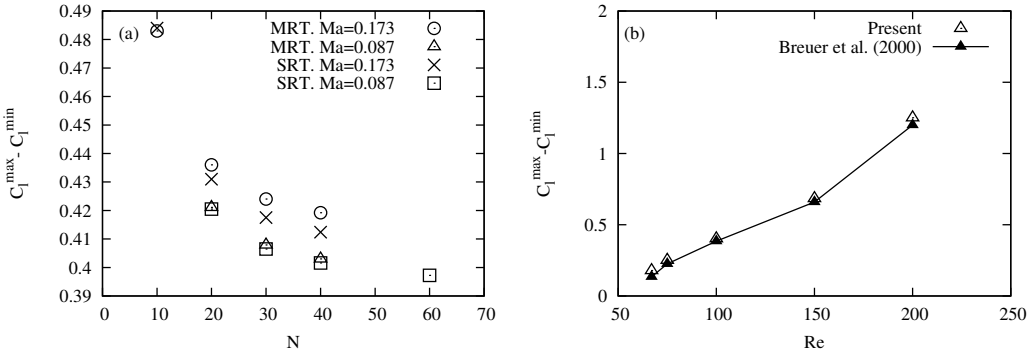

Figure 2.5: Peak-to-peak value of the lift coefficient: (a) grid convergence analysis for different Mach numbers (Re=100); and (b) the evolution with the Reynolds number of the asymptotic value from the grid convergence analysis.

Figures 2.4, 2.5 and 2.6 show the grid convergence analysis (for different Mach numbers) and the asymptotic values obtained performing a Richardson extrapolation of the C_d, peak-to-peak value of C_l and the Strouhal number. Results are compared with a finite volume calculation [49] used as the reference solution.

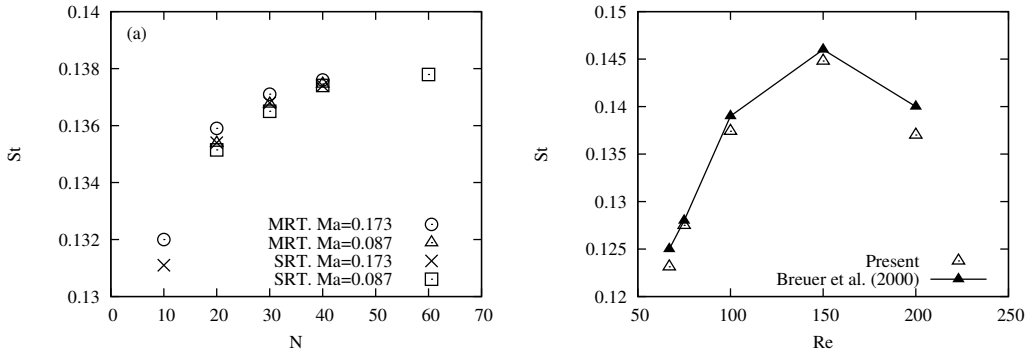

Figure 2.6: Strouhal values: (a) grid convergence analysis for different Mach numbers ($Re = 100$); and (b) the evolution with the Reynolds number of the asymptotic value from the grid convergence analysis.

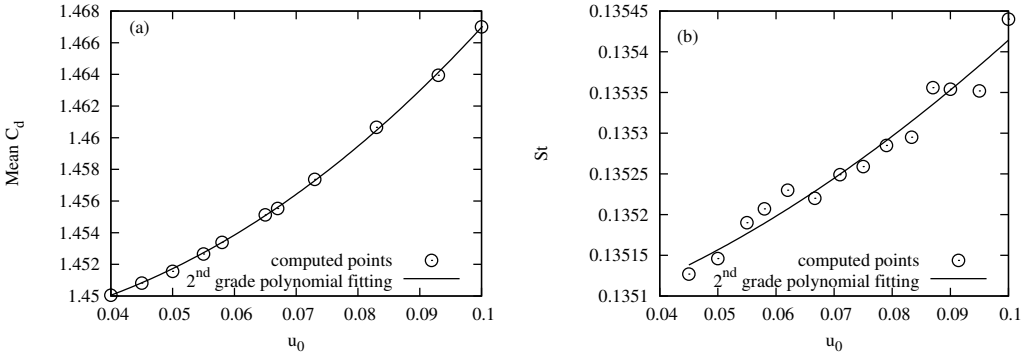

Figure 2.7: Dependence with the reference speed (i.e. Mach number) of: (a) mean value of the drag coefficient; and (b) Strouhal number.

2.3.2 Comparison of open boundary conditions

The reflection of some numerical information back to the domain, although necessary to conserve the macroscopic quantities (ρ and $\mathbf{u}$), provides a mechanism for undesired numerical waves to be reflected as well; such waves may interact with the solution of the flow. For low Reynolds numbers, this interaction may not alter significantly certain results such as time averaged quantities, but it does influence values such as the peak-to-peak value of the drag coefficient, $\Delta C_d = C_d^{max} - C_d^{min}$. For the case of the square cylinder, this is shown in Fig. 2.8.

Data plotted in Fig. 2.8 has been obtained from a series of simulations of the 2D square cylinder where: the reference velocity u_0, and therefore the Mach number, is different in each simulation in order to study its influence on the solution; the relaxation parameter τ was adjusted appropriately to keep a constant Reynolds number

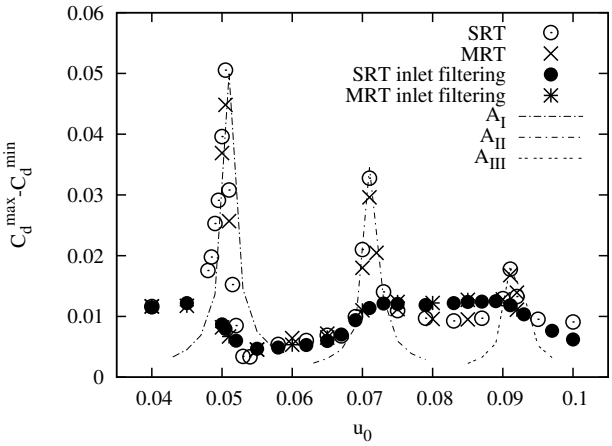

Figure 2.8: Peak-to-peak values of the temporal evolution of the drag coefficient versus the Mach number for $Re = 100$ using equilibrium boundary conditions with the SRT and MRT collision operator, and with density-filtering at the inlet.

($Re = 100$); the mesh size was also kept constant, with $N = 20$; at inlet and outlet equilibrium and filtered equilibrium boundary conditions are used as explained in Sec. 1.2; both SRT and MRT collision operators are considered in order to determine the influence of the dissipation due to a higher bulk viscosity (s_e up to 1.6 has been used with MRT) [24].

The main result in Fig. 2.8 is the presence of three clear peaks for ΔC_d that can be observed for three values of u_0: $u_0^I = 0.0505$, $u_0^{II} = 0.071$ and $u_0^{III} = 0.091$. These three peaks are expected to be related to the acoustic nature of the interaction between the open boundaries and the inner fluid.If this is the case, the behavior of ΔC_d as a function of u_0 can be approximately modeled using simple acoustic theory. Let us consider that the phenomenon studied can be likened to a forced oscillator with an angular frequency ω_f in a medium with a natural frequency of oscillation ω_o and with damping Γ. The equation that governs this system is the following:

$$\frac{d^2x}{dt^2} + \Gamma\frac{dx}{dt} + \omega_o^2 x = A_f cos(\omega_f t)\,; \tag{2.29}$$

where $x = \Delta C_d$ in this case; and A_f is the amplitude of the forced frequency. Solving this equation the following expression for the amplitude at steady state is obtained:

$$A = \frac{A_f}{\sqrt{(\omega_0^2 - \omega_f^2)^2 + \omega_f^2\Gamma^2}}\,. \tag{2.30}$$

Natural frequencies can be assumed to be related to the distance between inlet and outlet, L_{tot}. As a fixed velocity at inlet and a fixed density at outlet acts as and

Table 2.1: Comparison of values of ΔC_d at $u_0 = 0.05$ for different first and second order boundary conditions.

Boundary Condition	Collision Operator	Filtering	$C_d^{max} - C_d^{min}$
Equilibrium	SRT	No	0.0396
Equilibrium	MRT	No	0.0369
Equilibrium	SRT	Yes	0.0087
Equilibrium	MRT	Yes	0.0082
Zou & He (1997)	MRT	No	0.0222
Yu et al. (2005)	MRT	No	0.0081
Zou & He (1997)	MRT	Yes	0.0159

open-closed system for the pressure waves, the standing waves that are generated verify: $\omega_0 = 2\pi(2n-1)c_s/(4L_{tot})$, where n is a natural number. Forced frequencies are computed considering that pressure pulses are generated with a frequency which is twice the frequency of the vortex shedding. Thus, from the $St = 0.136$ and the reference speed u_0: $\omega_f = 4\pi St u_0/N$. The amplitude of the forced oscillations is fixed at $A_f = 1.8\,10^6$ to fit the first peak. The peaks appear when $\omega_0 = \omega_f$ and this occurs for the third ($\omega_0^I = 2\pi 0.00068$), fourth ($\omega_0^{II} = 2\pi 0.00095$), and fifth harmonic ($\omega_0^{III} = 2\pi 0.00122$) of the natural frequency. In Fig. 2.8 evolution of the amplitude for these three situations (A_I, A_{II} and A_{III}) has been plotted, considering an initial value for the damping $\Gamma_I = 0.00005$. The next value of Γ satisfies the relation $\Gamma_I/\Gamma_{II} = \nu_I/\nu_{II}$, where $\nu = Nu_0/Re$; and analogously for Γ_{III}.

The results in Fig. 2.8 have been computed using first order boundary conditions based on the equilibrium distribution functions. Viscous terms at boundaries (related to non-equilibrium distribution functions) act only as dissipative sources of pressure waves, but they do not appear in the Euler characteristics responsible for the wave propagation. To analyze the effect of using second order boundary conditions at open boundaries, values for ΔC_d at $u_0 = 0.05$ (close to the first peak) are collected in Table 2.1. It is observe that low values of ΔC_d (no peak) are obtained when the filtering at inlet is used and, especially, when the convective condition for f_α (Yu boundary condition) is applied. The use of a second order boundary condition reduces the peak due to the viscous effect but it does not eliminate it, as the origin of the peak is the coupling between vortex shedding and the natural (acoustic) frequencies of the system.

The temporal evolution of different variables is analyzed, Fig. 2.9, in order to compare the behavior of the boundary conditions described in Sec. 1.2. The evolution toward the periodic state of the drag coefficient, and the mass balance between inlet and outlet, shows that when the density is fixed at the outlet (Zou boundary condition) the behavior deteriorates. However this is often the appropriate boundary condition as pressure is usually known at outlets when a real case is modeled. On the other

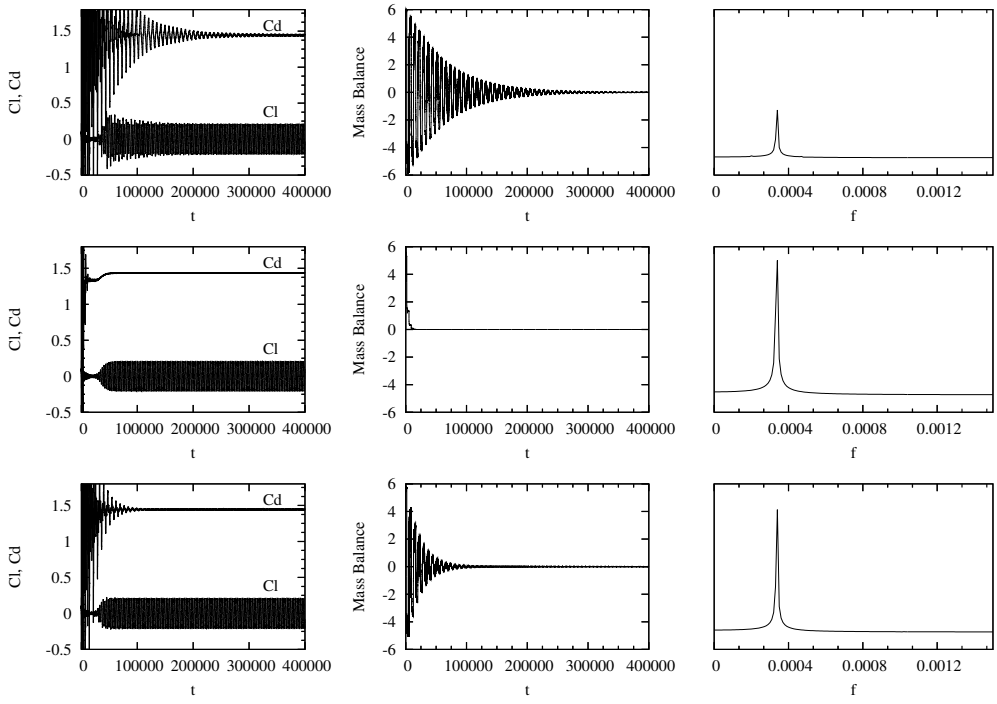

Figure 2.9: Comparison of: the temporal evolution of drag and lift coefficients (first column), the mass balance between inlet and outlet, and the FFT of the periodic temporal evolution of the lift coefficient (last column), from simulations using different open boundary conditions: Zou (first row), Yu and filtered Zou (last row).

hand, when the Yu boundary conditions are applied the periodic state is reached in fewer time steps, as the interaction of the boundaries with the domain interior has been avoided. Finally, the filtered-Zou condition preserves the desired density at outlet and also reduces the effect of the interaction by filtering the density at the inlet, needing fewer time steps to reach the periodic state than with the Zou boundary condition.

2.4 Test cases for Characteristic Boundary Conditions

Three cases are presented to test the several desirable properties of open boundary conditions. A one-dimensional pressure wave is simulated to check the difference between usual (reflective) boundary conditions (UBB for inlets and PAB for outlets, see Sec. 2.2.4) and non-reflective ones (CBC with $k_i = 0$); a laminar two-dimensional channel is used to quantify the mass balance within the domain due to the application of different boundary conditions; and the unsteady laminar two-dimensional flow

around a square cylinder is used to evaluate the benefit of using CBC in realistic geometries.

2.4.1 One-dimensional wave

A 2D one-directional flow in which a pressure perturbation is introduced at $t = 0$ is simulated. The boundary conditions used are: at the inlet a uniform velocity $u_x = u_0$ is imposed; at the outlet a reference density, $p_0 = c_s^2\rho_0 = 1/3$ is fixed; and the upper and lower boundaries have periodic boundary conditions. The flow is characterized by a Mach number $Ma = 0.1$ and a Reynolds number $Re = 1.732$ (based on the lattice space unit). The domain length in lattice units is $N_x = 2500$ ($N_y = 10$). As initial conditions, a uniform velocity field of $u_x = u_0$ and a Gaussian pressure pulse in the middle of the domain are imposed:

$$p = p_0 + (p_{max} - p_0)exp\left(\frac{-(X - X_0)^2}{2\varsigma^2}\right) ; \tag{2.31}$$

with the values selected for the free parameters being $p_{max} = \rho_{max}c_s^2 = 1.1c_s^2$, $X_0 = 0.5$ and $\varsigma = 50$. The velocity distribution functions are initially computed from their equilibrium distribution functions.

The variables used to report the results are: a dimensionless time $T = t(c_s/N_x)$, and a dimensionless coordinate $X = x/N_x$. All the simulations presented use the following relaxation factors: s_ν takes the value dictated by the resolution and the Reynolds and Mach numbers; $s_e = s_\epsilon = s_\nu$ unless otherwise specified below; and $s_q = 8(2 - s_\nu)/(8 - s_\nu)$ according to the relation stated in [31] (for $\Lambda_{eo} = 3/16$) to reduce the error at the boundaries. For inlets and outlets equilibrium boundary conditions are applied to recover first-order accuracy, and UBB at inlets and PAB at outlets to obtain second-order boundary conditions. For CBC $k_i = 0$ and $\kappa = 1$ are used unless some other values are specified.

To show the behavior of the proposed boundary condition and to assess the gain obtained, the temporal evolution of the initial pressure peak is plotted in Fig. 5.1 for different inlet-outlet boundary conditions. For all cases the peak splits as expected into two different pressure waves which travel at $u_0 + c_s$ and $u_0 - c_s$ respectively.

For the equilibrium boundary condition, these pressure waves are completely reflected at boundaries, changing their phase when they reach the fixed-pressure boundary condition. When adding the viscous correction at boundaries (UBB and PAB boundary conditions), the reflection may become even greater. The use of CBC partially suppresses the reflection at inlet and outlet; and when the κ-modified CBC is applied, the performance of the scheme is further improved.

To quantify the performance of the boundary conditions, the degree of reflection r is

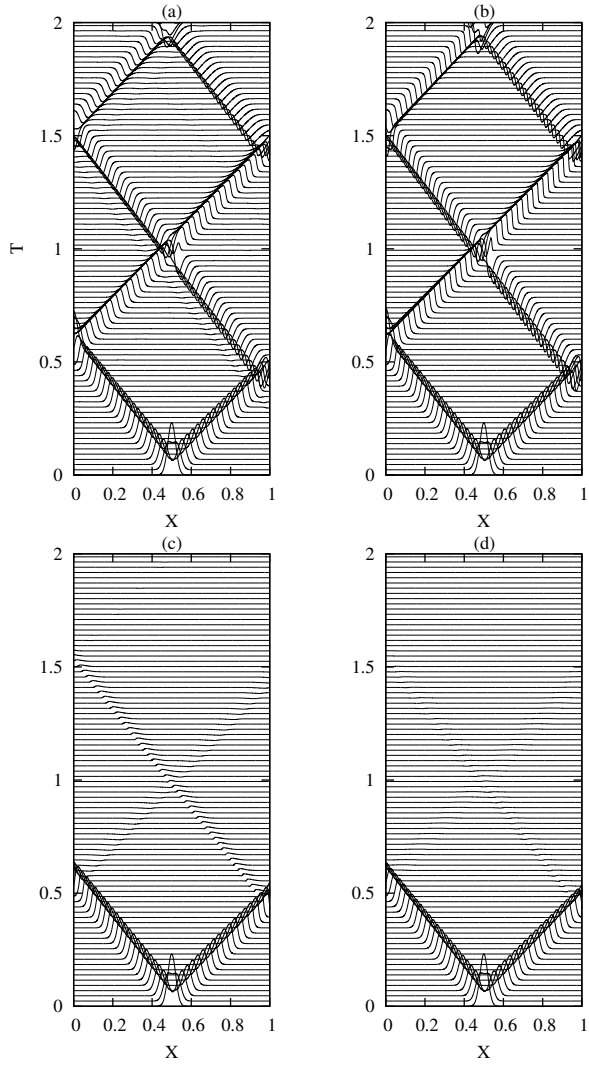

Figure 2.10: Spatial-temporal evolution of the pressure. The inlet and outlet boundary conditions applied are: (a) first order; (b) inlet: UBB, outlet: PAB; (c) CBC with $\kappa = 1.0$ and $s_e = s_\nu$; and (d) CBC with $\kappa = 1.2$ and $s_e = 0.65$

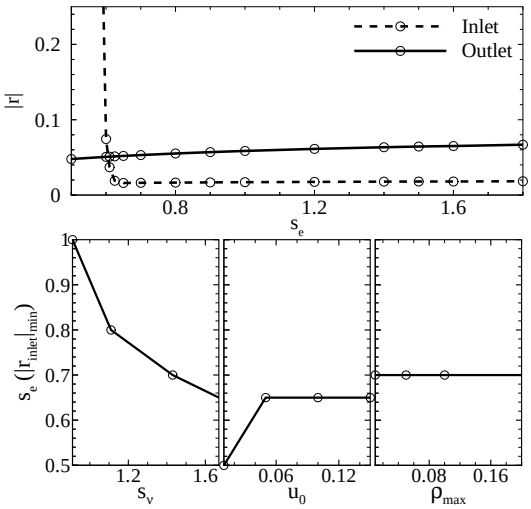

Figure 2.11: Reflection ratio as a function of s_e; and optimal s_e values depending on the viscous relaxation factor, the reference velocity and the initial amplitude of the pressure pulse.

defined as:

$$|r| = \frac{|L^+|}{|L^-|}\,; \tag{2.32}$$

where L^+ is the incoming wave amplitude and L^- is the outgoing one.

The influence of s_e through the bulk viscosity Eq. (2.11) can be used to reduce the reflection ratio. The smallest reflection is found numerically to occur when $s_e \approx 1/s_\nu$, Fig. 2.11. Results show that: $|r|$ is almost independent of the reference velocity and of the maximum value of the pressure peak; and the influence of s_e is noticed mainly at inlets.

The best-performing value of κ has been selected by carrying out several numerical tests (see Fig. 2.12), resulting in an optimal value in the range $1.0 < \kappa < 1.3$, which turns out to be slightly dependent on the viscous relaxation factor, on the reference velocity, and also on the amplitude of the pressure wave arriving at the boundary. There is no influence of κ at the inlet as it does not appear in the definition of the boundary.

From the test case presented, it can be concluded that the use of CBC in athermal lattice Boltzmann methods can reduce the reflection up to $|r| = 5\%$; and this reflection can be further reduced up to $|r| = 1\%$ using the κ-modified CBC.

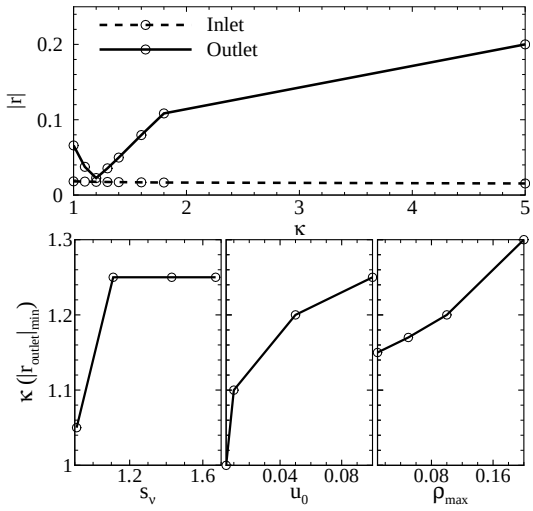

Figure 2.12: Reflection ratio as a function of κ; and optimal κ values for different values of the viscous relaxation factor, the reference velocity and the initial amplitude of the pressure pulse.

2.4.2 Laminar channel

A two-dimensional laminar channel with a parabolic velocity profile at the inlet and a reference pressure at the outlet is simulated to evaluate the mass imbalance in the fluid domain when the CBC is applied. The channel dimensions are $N_x = 520\delta x$ and $N_y = 160\delta x$, and is simulated at $Re = 800$ and $Ma = 0.087$. The domain is initialized with $u = 0.0$, $\rho_0 = 1.0$ and using equilibrium distribution functions. To evaluate the mass imbalance, the temporal evolution of three quantities is reported in Fig. 2.13: the total mass leaving the domain at the outlet as the sum of the outgoing distribution functions; the total mass coming into the domain at the inlet; and the total amount of mass in the entire fluid domain. The incoming and outgoing mass fluxes are normalized with the incoming mass flow through the inlet at $T = 0$; and the total mass in the domain is normalized with its value at $T = 0$. The temporal coordinate is defined as $T = t(c_s/N_x)$. The optimal values for κ and s_e found above are used when the CBC is applied.

Three different boundary-condition sets have been compared in Fig. 2.13: (i) non-reflecting CBC with $k_i = 0$, which is not able to properly fix the reference values and, consequently, the mass in the domain progressively increases without bounds until the simulation fails; (ii) partially-reflecting CBC with the value for k_i derived from the lower limit of Eq. (2.23), which is the only set of boundary conditions which is able to suppress pressure reflections and preserve mass, providing a faster convergence; and (iii) the Dirichlet velocity and pressure boundary conditions UBB

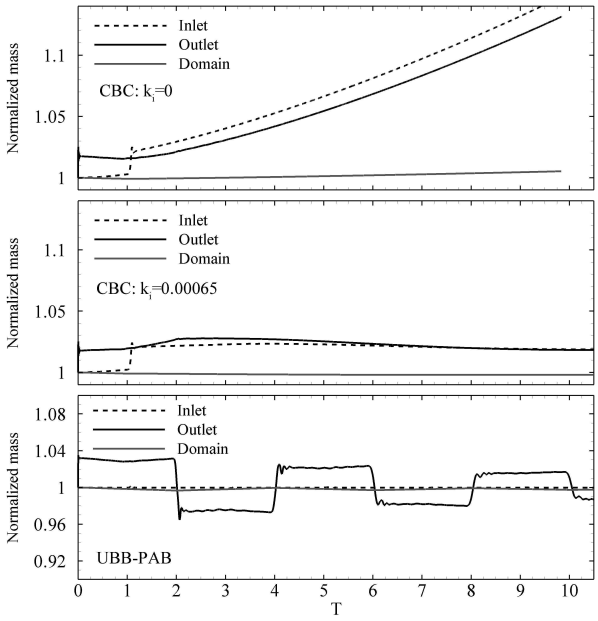

Figure 2.13: Temporal evolution of the normalized mass through the inlet and the outlet and within the domain for: (top) CBC with $k_i = 0$; (middle) CBC with k_i=0.00065; and (bottom) UBB-PAB boundary conditions

and PAB respectively, which generate an oscillation around the reference value of the total mass within the domain due to pressure wave reflection.

2.4.3 Vortex shedding

The two-dimensional unsteady flow around a confined square cylinder at Re=100 and Ma=0.087 is simulated to evaluate the behavior of the CBC versus the UBB-PAB in more complex configurations. The domain dimensions are $N_x = 26N_s$ and $N_y = 8N_s$, with $N_s = 20$ being the number of nodes which discretize the side of the square. The square is deliberately placed far from the inlet to avoid any interaction, and close to the outlet to analyze the effect of the interaction between the vortices generated in the wake of the cylinder and the outlet. The distance between the downstream face of the square and the outlet is $13.5N_s$, which is much less than $40N_s$ as usually applied to avoid the interaction.

Two remarks can be made from the comparison between CBC and UBB-PAB in this test case. The first and main point is that the interaction of the vortices with the outlet reflects pressure waves which deteriorate the solution: see for example the shape of the time evolution of the C_d at the periodic steady state in Fig. 2.14. The

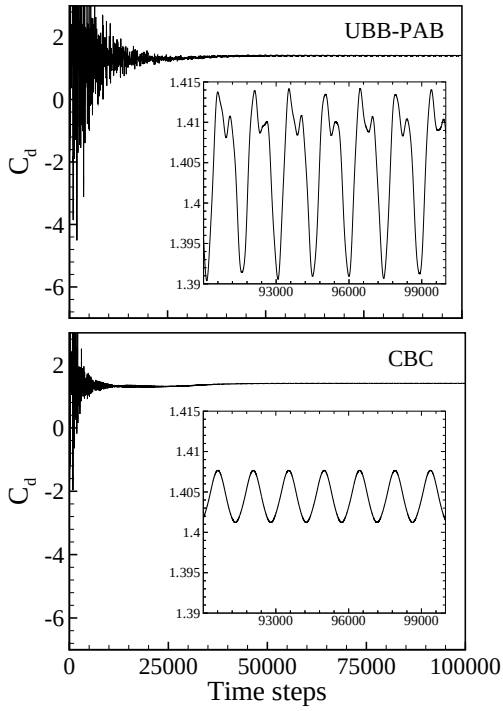

Figure 2.14: Temporal evolution of the drag coefficient of the square cylinder for two different set of open boundaries: UBB-PAB (top) and optimal CBC (bottom). The periodic steady state is magnified in the inset.

pressure-wave reflection between inlet and outlet affects the pressure pattern in the flow. It can be observed in Fig. 2.15 that when a vortex is shed from the cylinder the pressure is higher behind the cylinder when UBB-PAB is applied; additionally, unphysical pressure patterns appear, generating high-pressure and low-pressure zones near walls. The undesired influence of this interaction can be supported also by the peak which appears in the Fourier transform of the C_d signal at frequencies different from the one related to the vortex shedding, Fig. 2.16.

The second remark concerns the greater amplitude of C_d when UBB-PAB conditions are used, Fig. 2.14. This is caused by (numerical) resonance appearing as the vortex shedding frequency corresponds to a natural mode of the domain. The increased amplitude appears as a higher peak for the vortex shedding frequency in Fig. 2.16.

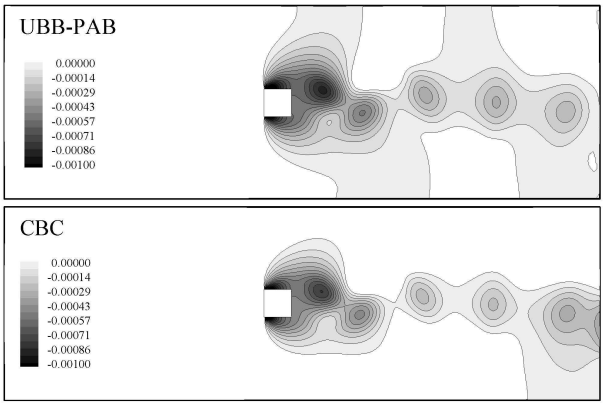

Figure 2.15: Pressure iso-contours at the same time step ($t = 95200\delta t$) for two set of open boundaries: UBB-PAB (top) and optimal CBC (bottom).

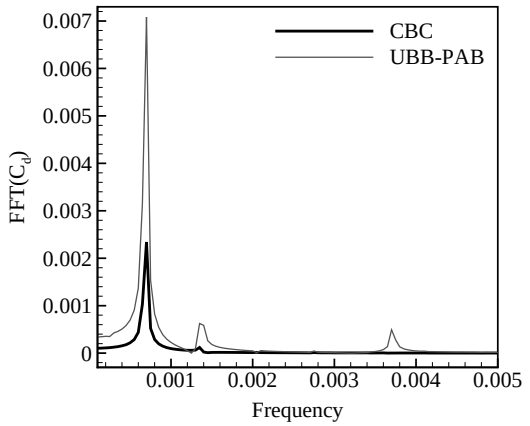

Figure 2.16: Fast Fourier transform of the C_d signal for the periodic flow using both sets of boundary conditions of Fig. 2.14

2.5 Conclusions

Several open boundary conditions have been studied to evaluate their performance when unsteady laminar fluid flows are simulated using lattice Boltzmann methods. Furthermore, two new non-reflecting boundary conditions have been presented and evaluated. The conclusions, with a brief discussion, of the results obtained are presented next.

The most commonly-used open boundary-conditions are reflective in nature (e.g. Zou boundary condition). The pressure wave reflections deteriorate the convergence towards a steady or periodic solution, and they can have a relevant influence in the solution itself. The convective boundary condition for f_α at the outlet, Eq. (1.21), solves the problem of the interaction between the open boundaries and the fluid domain; but the new problem arises of how to properly impose the reference pressure (or density). On the other hand, partially-reflecting and non-reflecting approaches can preserve the well-posedness of the boundary conditions while eliminating the interactions between the open boundaries and the flow domain.

When the periodic solution is reached, open boundary conditions introduce errors related to acoustics in the amplitude of the drag coefficient. These acoustic effects have been modeled for a benchmark problem as a forced oscillator with damping.

The effects of wave reflection are related to the convective term, and the viscous contribution can lessen the problem but not entirely avoid it. This means that a more accurate (i.e. higher order) boundary condition is not a solution. The same analysis has been performed with both SRT and MRT collision operators leading to the same results; the dissipation due to higher bulk viscosities is therefore irrelevant. The MRT collision operator has been implemented in its *incompressible* version, which is mainly a correction of the round-off error generated during the computation.

The characteristic non-reflective boundary condition presented for athermal LB methods can reduce the fluid-boundary interaction up to 99% and does not need additional absorbing layers nor extended domains. The new boundary conditions are expected to be useful not only for the simulation of the acoustic field, but also for many laminar and turbulent simulations in which pressure waves interact with the boundary condition. For the development of characteristic boundary conditions for LB the best choice of primitive variables are $\mathbf{U} = (\rho, u_x, u_y)$.

3

Gradient-based boundary conditions

3.1 Introduction

One of the strengths of the lattice Boltzmann methods is the ability to simulate complex geometries with the addition of little computational effort. Simulations with detailed geometries of porous media [54], blood vessels [55], indoor environments [56] or flow aerodynamics [7, 57] are some successful examples. Different implementations of Dirichlet conditions for arbitrary geometries have been developed; however, little research has been published related to the implementation of Neumann boundary conditions. This deficit is probably due to several factors, which can be illustrated using the stress boundary-condition as example. First, the stresses are macroscopic moments related to the non-equilibrium part of the distribution functions that have an $O(\partial_j u_i)$ influence on the accuracy of the boundary condition, which is sometimes neglected; additionally, many configurations do not require these kind of boundary conditions, and in the most common case where it is needed (zero tangential stresses for symmetry planes) the link-based approach can be applied through a specular reflection; furthermore, it is a hydrodynamic boundary condition and kinetic ones are often preferred (specially for microflows).

The use of Neumann conditions would allow to extend the applicability of the lattice Boltzmann method by setting, for example, effects related to $\partial_j u_i$ (e.g. stress over a porous wall, wall models for turbulent flows, hydrophobic-hydrophilic wall treatments) and to reduce the complexity of the domain (e.g. symmetry axis). From a macroscopic point of view these stresses at walls are usually treated as surface or volume forces (using Gauss transformation), which affects the fluid volume near the

wall, but ignoring the real behavior of the fluid just at the wall. The latter is relevant, because the macroscopic behavior is dictated by the microscopic interaction of the fluid with the wall, through collisions.

In the following, the evolution of boundary conditions in lattice Boltzmann methods is discussed to evaluate the best way to implement Neumann conditions. In this discussion, only macroscopic boundary conditions for the momentum equations are considered. However, the conclusions presented can be extended to any other macroscopic variable.

The first approximation to model walls in LB is the use of the bounce-back scheme [58] for the non-slip condition, and the application of a specular reflection for the complete slip or zero-stress condition. From this very straightforward starting point it is possible to observe the obvious relation between the stress at the wall, the wall-collision, and the slip condition.

Some first attempts to improve the accuracy of the bounce-back boundary condition (e.g. [39, 59, 60, 61]) have been applied to different lattices. Subsequent research established the influence of the relaxations parameters on the wall location [62] and the influence of the definition of the non-equilibrium part of the distribution functions on wall (and initial) conditions [35].

A first work on including arbitrary geometries was the one by Filippova and Hänel [63] based on modifications to the bounce-back using interpolations; this approach was improved by Mei et al. [64] and Bouzidi et al. [38], and generalized by Ginzburg et al. [30, 31]. Other approach to simulate curved geometries is based on the volumetric scheme by Chen et al. [65] which has been also improved [66]. The work by Verberg and Ladd [67] can be considered a different way to impose volumetric boundary conditions. One further approach is the extrapolation proposed by Chen et al. [50] and extended to curved geometries by Guo et al. [68]. Two additional concepts have been introduced, related to local boundary conditions [69, 70, 71], and immerse boundary conditions for lattice Boltzmann methods [72].

The development of Neumann boundary treatments in LB largely focuses on the definition of slip boundaries, or stress-related conditions, as they are linked to the development of wall boundary-conditions for microflows [73, 74]. Although, the use of kinetic boundary conditions to impose a predefined stresses has been attempted for straight walls, no satisfactory result has been obtained in curved geometries, for which their application becomes complex or impossible [74, 75].

Some attempts to simulate configurations which need Neumann conditions can be found in the literature [75, 76]. The best-suited hydrodynamic approach for setting Neumann conditions at boundaries, even with complex geometries, is often claimed to be the volumetric approach by Chen et al. [65].

The preceding review of boundary conditions for lattice Boltzmann methods provide some guidelines for an efficient implementation of Neumann boundary conditions. Thus, any method proposed should: (i) preserve the simplicity and good stability behavior of bounce-back-based schemes; (ii) be second-order (or higher) for arbitrary geometries; (iii) avoid the use of extrapolations related to hydrodynamic treatments [50]; and (iv) avoid the use of non-lattice distribution functions as in kinetic methods with non-zero off-diagonal kernels [73, 77].

The approach presented here treats the problem in a general efficient way preserving well-established boundary treatments [31] and including macroscopic-gradients with a low degree of added complexity. It is a practical approximation to solve the problem that can be formulated in a modular way to introduce improvements without changing the basic structure.

3.2 Macroscopic-gradient boundary conditions

Following the desirable requirements detailed above, the present proposal is based on:

- An interpolation scheme to set Dirichlet boundary-conditions for arbitrary walls. For first- and second-order approximations the scheme by Bouzidi et al. [38] can be applied. For higher-order approximations the multireflection boundary condition by Ginzburg and d'Humières [30] should be used. For a generalized approach the work by Ginzburg et al. [31] can be consulted.

- A pre-defined stencil for the derivative of the macroscopic variable. The stencil could use non-lattice values obtained by interpolating macroscopic quantities computed on the lattice.

This boundary treatment is described in the following for velocity- and pressure-gradient conditions. The work by Ginzburg et al. [31] is followed to define the different interpolation schemes applied. Some concepts have been already introduced in previous Chapters, but are included here again for completeness.

Some definitions, used to simplify the description of these schemes, are introduced next. The equilibrium distribution function can be split in a symmetric:

$$f_\alpha^{eq+} = \omega_\alpha \rho + \frac{1}{2}\omega_\alpha \rho_0 c_s^{-4}\left[(e_{i\alpha}u_i)^2 - c_s^2(u_i u_i)\right] \; ; \tag{3.1}$$

and anti-symmetric part:

$$f_\alpha^{eq-} = \omega_\alpha \rho_0 c_s^{-2}(e_{i\alpha}u_i) \, . \tag{3.2}$$

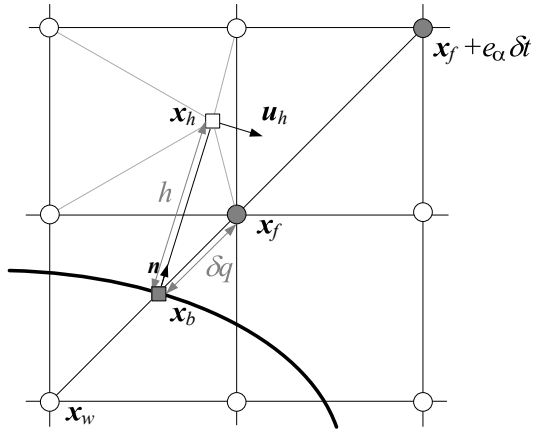

Figure 3.1: Schematic view of the wall treatment.

A similar description is used for distribution functions $f_\alpha = f_\alpha^+ + f_\alpha^-$, the components of which are computed as:

$$f_\alpha^+ = \frac{1}{2}(f_\alpha + f_{\bar{\alpha}}) \,, \tag{3.3}$$

$$f_\alpha^- = \frac{1}{2}(f_\alpha - f_{\bar{\alpha}}) \,; \tag{3.4}$$

where $\bar{\alpha}$ is the direction opposite to α in a link.

The non-equilibrium distribution function are then computed as:

$$f_\alpha^{neq+} = f_\alpha^+ - f_\alpha^{eq+} \,; \tag{3.5}$$

$$f_\alpha^{neq-} = f_\alpha^- - f_\alpha^{eq-} \,. \tag{3.6}$$

3.2.1 Velocity-gradient conditions

The distribution function in Dirichlet-velocity boundaries (see Fig. 3.1) can be generically computed through three terms [31]:

$$\begin{aligned} f_{\bar{\alpha}}(\mathbf{x}_f, t+1) &= R_\alpha^{(u)}(\mathbf{x}_f, t) \\ &+ F_\alpha^{p.c.(u)}(\mathbf{x}_f, t) \\ &+ W_\alpha^{(u)}(\mathbf{x}_b, \hat{t}) \,; \end{aligned} \tag{3.7}$$

where $R_\alpha^{(u)}(\mathbf{x}_f, t)$ is the interpolation scheme, $F_\alpha^{p.c.(u)}(\mathbf{x}_f, t)$ is the error correction to match the desired accuracy derived from a Chapman-Enskog expansion, and $W_\alpha^{(u)}(\mathbf{x}_b, \hat{t})$ is the Dirichlet condition at the boundary $\mathbf{x}_b$ and at a time $\hat{t} = t + \Delta t$ which depends on the interpolation scheme applied. The time $\hat{t}$ is the most appropriate time

(after theoretical and numerical analysis of the boundary condition [31]) to impose a time-dependent boundary condition; however, since only time-independent boundary-conditions are applied in the test cases described below, the implementation and the solutions obtained are independent of Δt.

3.2.1.1 UBB

The velocity bounce-back (UBB) [31] is the simplest scheme with the following terms:

$$R_\alpha^{(u)}(\mathbf{x}_f, t) = \tilde{f}_\alpha(\mathbf{x}_f, t)\,; \tag{3.8a}$$

$$F_\alpha^{p.c.(u)}(\mathbf{x}_f, t) = 0\,; \tag{3.8b}$$

$$W_\alpha^{(u)}(\mathbf{x}_b, \hat{t}) = -2f_\alpha^{eq-}(\mathbf{x}_b, \hat{t})\,; \tag{3.8c}$$

where $\tilde{f}$ are post-collision distribution functions. For these cases $\delta q = 1/2$ for every boundary link, $\hat{t} = t + 1/2\delta t$ and the accuracy obtained is second order for the anti-symmetric part of the distribution function (symbolized as $u^{(2)}$), and first order for the symmetric part (symbolized as $\Pi^{(1)}$).

3.2.1.2 ULI/DLI

The upwind linear interpolation (ULI) [31] are used for $0 \leq \delta q \leq 1/2$:

$$\begin{aligned} R_\alpha^{(u)}(\mathbf{x}_f, t) &= 2\delta q \tilde{f}_\alpha(\mathbf{x}_f, t) \\ &+ (1 - 2\delta q)\tilde{f}_\alpha(\mathbf{x}_f + \mathbf{e}_\alpha \delta t, t)\,; \end{aligned} \tag{3.9a}$$

$$F_\alpha^{p.c.(u)}(\mathbf{x}_f, t) = 0\,; \tag{3.9b}$$

$$W_\alpha^{(u)}(\mathbf{x}_b, \hat{t}) = -2f_\alpha^{eq-}(\mathbf{x}_b, \hat{t})\,. \tag{3.9c}$$

The downwind linear interpolation (DLI) [31] are used for $\delta q \geq 1/2$:

$$\begin{aligned} R_\alpha^{(u)}(\mathbf{x}_f, t) &= \frac{1}{2\delta q}\tilde{f}_\alpha(\mathbf{x}_f, t) \\ &+ \frac{2\delta q - 1}{2\delta q}\tilde{f}_\alpha(\mathbf{x}_f + 2\mathbf{e}_\alpha \delta t, t)\,; \end{aligned} \tag{3.10a}$$

$$F_\alpha^{p.c.(u)}(\mathbf{x}_f, t) = 0\,; \tag{3.10b}$$

$$W_{\alpha}^{(u)}(\mathbf{x}_b,\hat{t}) = -\frac{1}{\delta q} f_{\alpha}^{eq-}(\mathbf{x}_b,\hat{t})\,. \tag{3.10c}$$

The accuracy obtained is $u^{(2)}$ and $\Pi^{(1)}$; and $\hat{t} = t + 1/2\delta t$.

3.2.1.3 MR1

Among the different schemes within the multireflection family the MR1 is selected [31], which has the following terms:

$$\begin{aligned} R_{\alpha}^{(u)}(\mathbf{x}_f,t) &= \tilde{f}_{\alpha}(\mathbf{x}_f,t) \\ &+ \frac{1-2\delta q-2\delta q^2}{(1+\delta q)^2} \\ &\left[\tilde{f}_{\alpha}(\mathbf{x}_f+\mathbf{e}_{\alpha}\delta t,t) - \tilde{f}_{\bar{\alpha}}(\mathbf{x}_f,t)\right] \\ &+ \frac{\delta q^2}{(1+\delta q)^2} \\ &\left[\tilde{f}_{\alpha}(\mathbf{x}_f+2\mathbf{e}_{\alpha}\delta t,t) - \tilde{f}_{\bar{\alpha}}(\mathbf{x}_f+\mathbf{e}_{\alpha}\delta t,t)\right]\,; \end{aligned} \tag{3.11a}$$

$$F_{\alpha}^{p.c.(u)}(\mathbf{x}_f,t) = \frac{2s_q-4}{(1+\delta q)^2}\left(f_{\alpha}^{neq-} + \frac{1}{2}w_{\alpha}\mathbf{e}_{\alpha}\mathbf{F}\right)\,; \tag{3.11b}$$

$$W_{\alpha}^{(u)}(\mathbf{x}_b,\hat{t}) = -2\left(1+\frac{1-2\delta q-\delta q^2}{(1+\delta q)^2}\right) f_{\alpha}^{eq-}(\mathbf{x}_b,\hat{t})\,. \tag{3.11c}$$

The accuracy obtained is $u^{(3)}$ and $\Pi^{(2)}$; and $\hat{t} = t + 1/2\delta t$. Simulations performed with this boundary condition have shown that, although it is possible to obtain more accurate results, the stability of the whole simulation is affected by its application. Therefore, this boundary condition should be used carefully.

3.2.1.4 Derivative stencils

The most common velocity-gradient conditions are related to the tangential stress at the wall. A first order stencil for the derivative along the normal direction n of the wall-tangential velocity u_θ is considered, which is used to compute the tangential stress (see Fig. 3.1 for nomenclature):

$$\tau_{\theta b} = \rho_0\nu\frac{\partial u_\theta}{\partial n} \approx \rho_0\nu\frac{u_{\theta h}-u_{\theta b}}{h}\,; \tag{3.12}$$

where $h = \delta x$ for $q < 0.5$ and $h = 1.5\delta x$ $q \geq 0.5$. This is a somewhat arbitrary selection of h but it allows to compute $u_{\theta h}$ within a region next to the wall in which stable interpolation schemes can be applied. A bilinear interpolation of macroscopic variables is used in this work because higher order interpolations are not expected to generate better or more stable results [78], and because other mixed interpolation techniques used in immerse boundary methods for the Navier-Stokes equations increase the complexity of the implementation [79]. The length h and the corresponding weights for the bilinear interpolation can be computed in a preprocessing, as it is done for δq values. This preprocessing is performed only once for stationary geometries.

The first order approximation assumes a linear profile of the stress, which makes it applicable to laminar flows and to turbulent ones with enough resolution near the wall. Wherever this assumption is no longer valid (e.g. non-newtonian fluids), higher-order stencils can be considered. Furthermore, for some special cases (e.g. turbulent flows with coarse near-wall resolution [80] or even for microflows [81]) predefined velocity profiles, namely wall laws, could be applied.

For the case of a Neumann boundary condition the velocity to be added to the wall to account for the imposed stresses, considering Eq. (3.12), is:

$$\rho_0 \nu \frac{\partial u_\theta}{\partial n} \,|_{\mathbf{x}_b} = \tau_{\theta b} \Longrightarrow u_{\theta b} \approx u_{\theta h} - \frac{\tau_{\theta b} h}{\rho_0 \nu} \,. \tag{3.13}$$

When a Robin condition is applied, the equivalent wall-slip velocity is computed as:

$$u_{\theta b} = K \frac{\partial u_\theta}{\partial n} \Longrightarrow u_{\theta b} \approx \frac{u_{\theta h}}{1 + \frac{h}{KH}} \,. \tag{3.14}$$

Finally, to introduce $u_{\theta b}$ into the momentum transfer correction equations, i.e. the Dirichlet term in Eq. (3.7), a projection of the tangential velocity $u_{\theta b}$ into the x and y directions is needed:

$$\mathbf{u}_b = \frac{u_{\theta b} \mathbf{n}}{\|\mathbf{n}\|} \,. \tag{3.15}$$

3.2.2 Pressure-gradient conditions

As for velocities, the Dirichlet condition for pressure can be generically expressed as [31]:

$$\begin{aligned} f_{\bar{\alpha}}(\mathbf{x}_f, t+1) &= R_\alpha^{(p)}(\mathbf{x}_f, t) \\ &+ F_\alpha^{p.c.(p)}(\mathbf{x}_f, t) \\ &+ W_\alpha^{(p)}(\mathbf{x}_b, \hat{t}) \,; \end{aligned} \tag{3.16}$$

where the several terms have the same meaning as in Eq. (3.7) but applied to pressure. For the computation of $W_\alpha^{(p)}(\mathbf{x}_b, \hat{t})$ the velocity at the wall is approximated, for all interpolations schemes, as:

$$\mathbf{u}(\mathbf{x}_b, \hat{t}) \approx \mathbf{u}(\mathbf{x}_b + \mathbf{e}_\alpha \delta t, t) + \frac{1}{2}\left(\mathbf{u}(\mathbf{x}_b + \mathbf{e}_\alpha \delta t, t) - \mathbf{u}(\mathbf{x}_b + 2\mathbf{e}_\alpha \delta t, t)\right) . \tag{3.17}$$

3.2.2.1 PAB

The simplest Dirichlet pressure-scheme is the pressure anti-bounce-back (PAB)[31], which has the following terms in Eq. (3.16):

$$R_\alpha^{(p)}(\mathbf{x}_f, t) = -\tilde{f}_\alpha(\mathbf{x}_f, t) ; \tag{3.18a}$$

$$F_\alpha^{p.c.(p)}(\mathbf{x}_f, t) = (2 - s_\nu) f_\alpha^{neq+}(\mathbf{x}_f, t) ; \tag{3.18b}$$

$$W_\alpha^{(p)}(\mathbf{x}_b, \hat{t}) = 2 f_\alpha^{eq+}(\mathbf{x}_b, \hat{t}) . \tag{3.18c}$$

The accuracy obtained is $u^{(2)}$ and $\Pi^{(2)}$.

3.2.2.2 PLI

A pressure linear interpolation (PLI) scheme[31] allows to work with varying δq values. The corresponding terms are:

$$\begin{aligned} R_\alpha^{(p)}(\mathbf{x}_f, t) &= (\frac{1}{2} - \delta q)\tilde{f}_\alpha(\mathbf{x}_f, t) \\ &+ (\delta q - 1)\tilde{f}_\alpha(\mathbf{x}_f + \mathbf{e}_\alpha \delta t, t) \\ &+ \frac{1}{2}\tilde{f}_{\bar{\alpha}}(\mathbf{x}_f, t) ; \end{aligned} \tag{3.19a}$$

$$F_\alpha^{p.c.(p)}(\mathbf{x}_f, t) = [1 - (\delta q - 1)s_\nu] f_\alpha^{neq+}(\mathbf{x}_f, t) ; \tag{3.19b}$$

$$W_\alpha^{(p)}(\mathbf{x}_b, \hat{t}) = f_\alpha^{eq+}(\mathbf{x}_b, \hat{t}) . \tag{3.19c}$$

The accuracy obtained is $u^{(2)}$ and $\Pi^{(2)}$.

3.2.2.3 PMR1

A higher order scheme is derived from the pressure multi-reflection (PMR) family:

$$\begin{aligned} R_\alpha^{(p)}(\mathbf{x}_f,t) &= (1-s_\nu)\tilde{f}_\alpha(\mathbf{x}_f,t) \\ &+ \left[\frac{3s_\nu+\delta q(2-3s_\nu)}{4}-1\right]\tilde{f}_\alpha(\mathbf{x}_f+\mathbf{e}_\alpha\delta t,t) \\ &+ \left[\frac{s_\nu(3\delta q-1)}{4}-\frac{\delta q}{2}\right]\tilde{f}_\alpha(\mathbf{x}_f+2\mathbf{e}_\alpha\delta t,t) \\ &+ \left[1-\frac{s_\nu+\delta q(2+s_\nu)}{4}\right]\tilde{f}_{\bar{\alpha}}(\mathbf{x}_f,t) \\ &+ \left[\frac{\delta q(2+s_\nu)-s_\nu}{4}\right]\tilde{f}_{\bar{\alpha}}(\mathbf{x}_f+\mathbf{e}_\alpha\delta t,t)\,; \end{aligned} \tag{3.20a}$$

$$F_\alpha^{p.c.(p)}(\mathbf{x}_f,t)=\frac{s_\nu^2}{4}(3+6\frac{\delta q}{s_\nu}-11\delta q)f_\alpha^{neq+}(\mathbf{x}_f,t)\,; \tag{3.20b}$$

$$W_\alpha^{(p)}(\mathbf{x}_b,\hat{t})=s_\nu f_\alpha^{eq+}(\mathbf{x}_b,\hat{t})\,. \tag{3.20c}$$

The accuracy obtained is $u^{(3)}$ and $\Pi^{(2)}$.

3.2.2.4 Derivative stencils

Boundary conditions involving a pressure gradient are found when the presence of fans or vents on a boundary is to be modeled, or when a pressure drop is generated by a subgrid device. To compute pressure gradients, a first order derivative stencil is considered (see Fig. 3.1 for nomenclature):

$$\frac{\partial p}{\partial n}\approx\frac{p_h-p_b}{h}\Longrightarrow p_b\approx p_h+\frac{\partial p}{\partial n}h\,. \tag{3.21}$$

However, non-linear pressure profiles can be usually found in viscous fluid flow, and hence a second order stencil is desired. The derivative is computed using two points located within the bulk of the fluid in the normal (or tangential) direction. Considering the normal direction, the first point will be located at h_1 and the second point at h_2. The pressure at these points are computed with a bilinear interpolation.

$$\begin{aligned} \frac{\partial p}{\partial n} &\approx \frac{(h_2^2-h_1^2)}{h_1h_2(h_1-h_2)}p_b-\frac{h_2^2}{h_1h_2(h_1-h_2)}p_{h_1}+\frac{h_1^2}{h_1h_2(h_1-h_2)}p_{h_2} \\ \Longrightarrow\quad p_b &\approx \frac{h_1h_2(h_1-h_2)}{(h_2^2-h_1^2)} \\ &\left(\frac{\partial p}{\partial n}+\frac{h_2^2}{h_1h_2(h_1-h_2)}p_{h_1}-\frac{h_1^2}{h_1h_2(h_1-h_2)}p_{h_2}\right)\,. \end{aligned} \tag{3.22}$$

3.2.3 Non-reflecting formulation

The characteristic boundary condition introduced in Chapter 2 can be transformed to be used with Neumann conditions. The transformed LODI relations, Eq. (2.16), considering spatial derivatives in the normal direction to the boundary, are:

$$\frac{\partial \rho}{\partial n} = \frac{1}{c_s^2}\left[\frac{L_3}{u_n} + \frac{1}{2}\left(\frac{L_4}{u_n + c_s} + \frac{L_1}{u_n - c_s}\right)\right] ; \tag{3.23a}$$

$$\frac{\partial u_n}{\partial n} = \frac{1}{2\rho_0 c_s^2}\left(\frac{L_4}{u_n + c_s} - \frac{L_1}{u_n - c_s}\right) ; \tag{3.23b}$$

$$\frac{\partial u_\theta}{\partial n} = \frac{L_2}{u_n} . \tag{3.23c}$$

See Chapter 2 for implementation aspects.

3.2.4 Corners and special boundaries

The term special boundaries is used to refer to those which do not allow to properly implement the boundary condition desired. As this depends on the type of boundary condition, different considerations must be made for the macroscopic-gradient-based conditions and for the non-reflecting formulation.

Since in the proposal made above link-based schemes are applied to take into account arbitrary geometries, the same considerations as in [31] can be made with links where not enough nodes are available in the link direction. If only nodes up to $\mathbf{x}_f + \mathbf{e}_\alpha \delta t$ are available, $\tilde{f}_\alpha(\mathbf{x}_f + 2\mathbf{e}_\alpha \delta t, t)$ can be replaced by $f_\alpha(\mathbf{x}_f + \mathbf{e}_\alpha \delta t, t+1)$. If only $\mathbf{x}_f$ is available, it is possible to switch to UBB for velocity- and to PAB for pressure-related conditions; or, if $\tilde{f}_\alpha(\mathbf{x}_f + \mathbf{e}_\alpha \delta t, t)$ is replaced with $f_\alpha(\mathbf{x}_f, t+1)$, it is possible to switch to ULI/DLI or PLI, respectively.

Regarding the non-reflecting formulation, there should be no problem to compute the normal derivative to each cut between a lattice link and the boundary, as it is a non-lattice computation. For corners the bisectrix can be used as the normal direction. Additionally, it should be remarked that the suppression of the non-reflecting formulation for some specific conflictive points should not drastically deteriorate the solution.

3.3 Test case I: partial slip in planar walls

Two test cases are used to validate the new boundary-condition treatment proposed: (i) the flow between two plates with a partial-slip boundary-condition at walls, for

both a Couette flow and a laminar channel; and (ii) the flow around a circular cylinder with complete slip condition at walls. With these test cases the behavior in steady and unsteady flows, and with planar and curved boundaries is analyzed.

The laminar two-dimensional steady state flow between two plates located at $y = 0$ and $y = H$ is defined by the Navier-Stokes equations without temporal or convective terms:

$$0 = -\frac{\partial p}{\partial x} + \frac{\partial}{\partial y}\left(\rho_0 \nu \frac{\partial u}{\partial y}\right) ; \tag{3.24a}$$

$$0 = \frac{\partial p}{\partial y} . \tag{3.24b}$$

These equations are solved analytically for two different flows, i.e. Couette and Hagen-Poiseuille, with partial-slip boundary-conditions.

3.3.1 Partial-slip Couette-flow

A Couette flow is simulated, where the upper wall drives the flow with $u(H) = u_0$ and the lower wall has a slip behavior defined by two alternative laws: Neumann, $\partial_y u_N(0) = \tau_w$; and Robin, $u_R(0) = KH\partial_y u$. The UBB boundary condition, Eq. (3.8), is used for both walls and periodic conditions are applied at the inlet and at the outlet. Solving Eq. (3.24) with these boundary conditions, the following solutions are obtained for the Neumann condition:

$$u_N(y) = u_0 - \frac{\tau_w}{\rho_0 \nu}(H - y) ; \tag{3.25}$$

and for the Robin one:

$$u_R(y) = u_0 \left[1 + \frac{y - H}{K + H}\right] . \tag{3.26}$$

The respective slip velocities u_s at the lower wall for both conditions is:

$$u_s = u_N(0) = 1 - \frac{\tau_w}{u_0 \rho_0 \nu}; \quad u_s = u_R(0) = \frac{K}{H + K} . \tag{3.27}$$

Simulations to reproduce several slip velocities u_s at the lower wall are performed. The parameters for the Neumann and Robin boundary conditions are computed from Eq. (3.27) for u_s= 0, 1/3, 2/3 and 1. Results are plotted using normalized variables in Fig. 3.2, where are compared with the analytical solution Eq. (3.25) and (3.26).

To validate the behavior of the boundary condition for unsteady simulations the time-dependent equation is solved for the Couette flow with the boundary condition

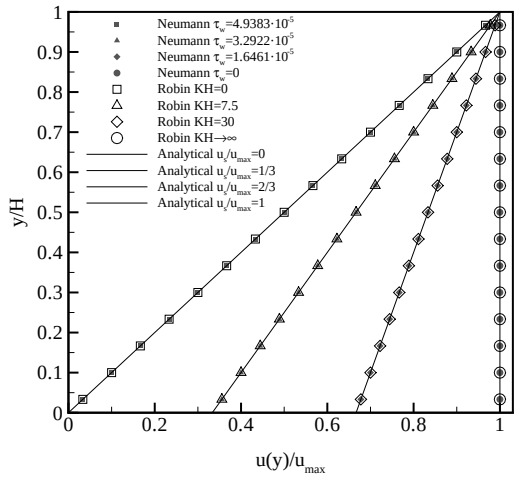

Figure 3.2: Solutions of the Couette flow for several values of the Robin and Neumann boundary conditions. $Re = 10$, $s_\nu = 5/3$, $H = 15\delta x$ and $\delta q = 0.5$.

at the lower wall $\partial_y u(0) = 0$. A Laplace transform procedure is applied (see, for example, [82]) to obtain the analytical solution:

$$\begin{aligned} u(y,t) &= u_0 - \frac{4u_0}{\pi}\sum_{n=0}^{\infty}\frac{(-1)^n}{2n+1} exp(-\frac{(2n+1)^2\pi^2}{4}\frac{\nu t}{H^2}) \\ &\times \quad cos\frac{(2n+1)\pi y}{2H}\,; \end{aligned} \tag{3.28}$$

where the series are computed up to the $n = 1000th$ term to compare with the lattice Boltzmann results. The comparison is shown in Fig. 3.3, for several dimensionless times $T = \nu t/H^2$.

3.3.2 Partial-slip channel

The laminar flow in a two-dimensional channel with partial-slip conditions is simulated. Equation (3.24) is solved here using a Robin condition in the lower and upper wall, $u(0) = u(H) = KH\partial_y u$, and with stream-wise periodic condition. The solution is:

$$u(y) = -\frac{1}{2\rho_0\nu}\frac{dp}{dx}(H^2K + Hy - y^2)\,. \tag{3.29}$$

In this case, the ULI/DLI scheme is used, Eq. (3.9) and (3.10), with a first order stencil for the velocity derivative. The flow is driven by a body force where the acceleration dp/dx is computed from Eq. (3.29) considering the parameters of the

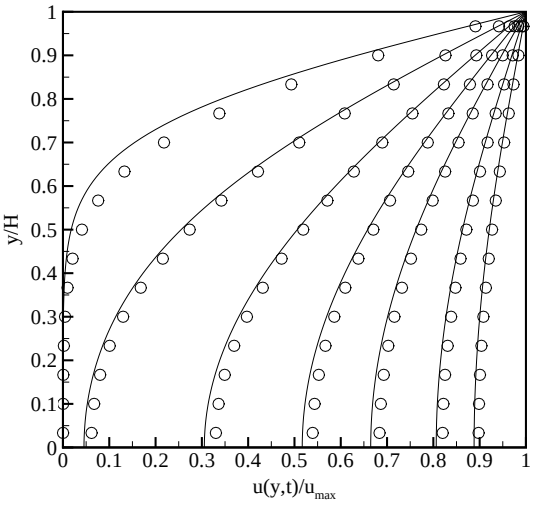

Figure 3.3: Temporal evolution towards the steady state. $Re = 10$, $s_\nu = 5/3$, $H = 15\delta x$ and $\delta q = 0.5$. From left to right results for T = 0.022, 0.096, 0.244, 0.393, 0.541, 0.763 and 0.985. The solid lines are the analytical solutions from Eq. (3.28).

flow. The ULI/DLI scheme allows to evaluate the behavior of the Robin condition for different δq values. In Fig. 3.4 the velocity profile for several δq in the lower wall is shown (which implies $1 - \delta q$ in the upper one, as the walls are parallel to the lattice), and compared with the analytical solution.

To test the accuracy of the scheme several simulations are performed with different resolutions and with different δq. In Fig. 3.5 (left) the spatial second order of the method is confirmed; and in Fig. 3.5 (right) the dependence of the solution on the δq value is plotted. The information in both graphics could be combined to plot the error as a function of the pair H–δq.

3.4 Test case II: slip flow past a cylinder

The two-dimensional flow around a circular cylinder with slip boundary conditions ($\tau_b = 0$) is used to validate the scheme proposed to account for curved boundaries. This validation is based on the following definition of the drag coefficient:

$$C_d = \frac{F_d}{\frac{1}{2}\rho_0 u_0^2 D}\,. \tag{3.30}$$

The analytical and experimental expressions to validate the boundary condition proposed in this work are for the low-Reynolds and low-Eotvos number regimes [83],

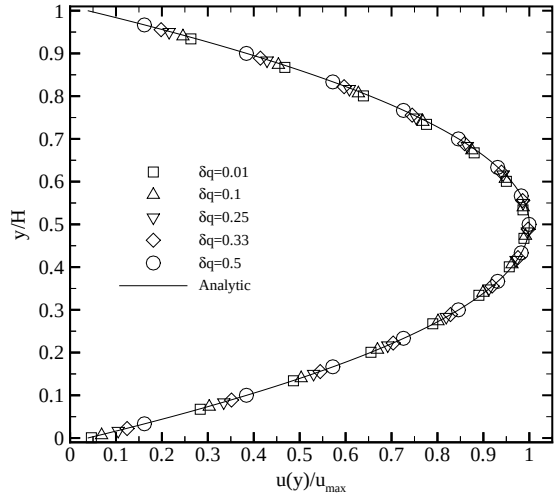

Figure 3.4: Velocity profile in the slip channel with K=0.01 for several δq in the lower wall. $Re = 10$, $s_\nu = 5/3$ and $H = 15\delta x$.

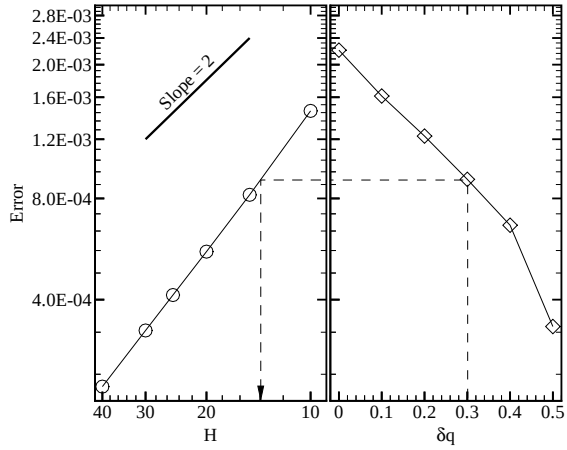

Figure 3.5: Error as a function of resolution (left) for $Re = 10$, $s_\nu = 5/3$, $K = 0.01$ and $\delta q = 1/3$; and δq (right) for $Re = 10$, $s_\nu = 5/3$, $K = 0.01$ and $H = 15\delta x$.

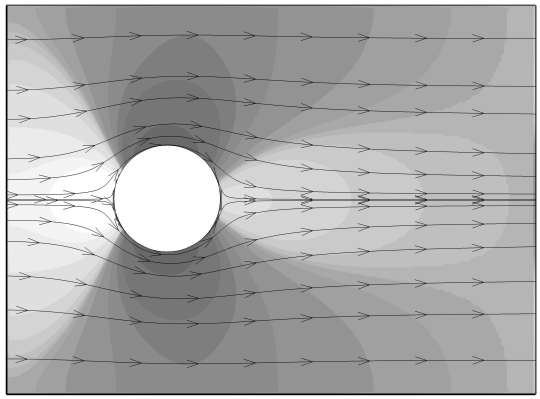

Figure 3.6: Pressure contours and streamlines of the flow around a cylinder with slip boundary conditions, $Re = 30$.

which prevail, for instance, in the slow motion of bubbles in a liquid. An analytical analysis allows to recover the following expressions for very low Reynolds:

$$C_d = \frac{16}{Re}\,, \tag{3.31}$$

which is the drag coefficient for the Stokes flow [83]; and

$$C_d = \frac{16}{Re}\left(1 + \frac{Re}{8}\right)\,, \tag{3.32}$$

which is the Oseen correction for finite Reynolds [83]. For moderate Reynolds numbers $Re > 2$, the following expression can be used [83]:

$$C_d = 14.9 Re^{-0.78}\,; \tag{3.33}$$

and for high Reynolds numbers ($Re >> 1$) the Moore drag estimate is [83]:

$$C_d = \frac{48}{Re}\left[1 - \frac{2.21}{Re^{1/2}}\right]\,. \tag{3.34}$$

The main characteristic of the flow around a cylinder or a sphere with total slip at boundaries is the absence of a recirculation region downstream. The flow around a two-dimensional cylinder is represented in Fig. 3.6, where streamlines and pressure isocontours are plotted. In Fig. 3.7 the evolution of the drag coefficient as a function of the Reynolds number obtained by numerical simulations with the LB method is plotted and compared with Eqs. (3.31)-(3.34).

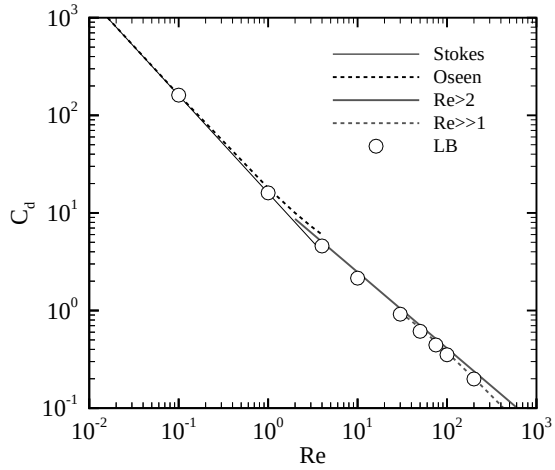

Figure 3.7: Evolution of the drag coefficient C_d as a function of the Reynolds number for a 2D circular cylinder with slip boundary conditions. LB results, and analytical and experimental-correlated expressions.

3.5 Conclusions

An approach to prescribe macroscopic-gradient boundary conditions in lattice Boltzmann methods, in which finite difference stencils are use for macroscopic variables, has been introduced and validated.

The proposed approach to implement velocity-gradient conditions (i.e. stresses) is similar in concept to the treatment used in immerse boundary methods for Navier-Stokes equations [79, 84]. Extensions of the method, not presented here, could include the application to impose boundary conditions for other variables related to velocity derivatives, such as vorticity.

The structure of the scheme tested is flexible an it is applicable to the lattice Boltzmann equation with any collision operator; additionally, the second order approach for curved geometries can be switched to any other if the accuracy [31] or the localness [16] need to be improved. The extension to three-dimensional flows is straightforward and it does not require further considerations.

The stability of the scheme is dictated by the Dirichlet approach applied. For example, for complex geometries, although the MR1 scheme has better accuracy [31], is unstable for some flow-parameter combinations, and hence, the ULI/DLI one [38] is preferred.

4

Preconditioning: derivation

4.1 Introduction

The main purpose of preconditioning is the acceleration of the flow toward the steady state. This is achieved by manipulating the eigenvalues of the Navier-Stokes system in order to reduce its stiffness and to obtain better solvability conditions. The use of time-derivative preconditioners in CFD was initially applied to compressible non-viscous flows [85]; the works by Turkel [86] and by Choi and Merkle [87] extended its application to viscous-flow solvers. In the case of viscous flows it becomes essential for compressible, low-Mach-number flows, as those addressed in many lattice Boltzmann simulations. At this low-compressibility limit, the stiffness arises from the disparity between the mean velocity of the flow and the speed of sound. See the review by Turkel [88] for a comprehensive insight into this technique. (In classical CFD, preconditioning is also applied when solving the linear problem in implicit methods; but this is a different use of preconditioning from the one studied in this work.)

Due to the poor computational performance of the standard explicit collision-propagation algorithm for steady-state computations, many different approaches to accelerate lattice Boltzmann simulations have been described in the literature. To provide an overview of these techniques, first the methods to solve the discrete Boltzmann equation (DBE) are divided in lattice and non-lattice methods. Within lattice methods, only those based on the explicit collision-propagation algorithm (which is the approach used in this Thesis) are considered. The approaches for the acceleration of this scheme may be classified into three groups, which are:

- body-force approaches, first proposed in [89], which apply a body force at each lattice node, proportional to the temporal variation of momentum, to accelerate the convergence to the steady state;

- preconditioning of the recovered Navier-Stokes equations [90], relating the preconditioning techniques applied in Computational Fluid Dynamics to lattice Boltzmann methods; and

- grid-based techniques, such as multi-block [91, 92], grid refinement [93] or multigrid [94], among others, which exploit different concepts related to the grid construction and resolution to reduce the time and memory usage needed for a specific simulation.

Notice here that these latter techniques are conditioned by the space-time coupling existing in lattice Boltzmann methods. On the other hand, non-lattice methods can be divided into two main groups: those built by the space-time discretization (using the same velocity sets as in LB methods) of the DBE (e.g. [95, 96, 97]); and those built from the discretization of the Taylor-series expansion along characteristics of the discrete Boltzmann equation [20, 22]. Both groups involve the solution of the corresponding partial differential equation using some kind of finite difference [95], finite element [20, 22] or finite volume method [96, 97]. These methods, based on non-lattice approaches, are an interesting framework to import acceleration techniques applied in classical compressible and/or pseudo-compressible CFD approaches. Some of them have already been applied in lattice Boltzmann methods: the use of unstructured grids [20]; modification of the CFL number [20]; the preconditioning of the implicit linear matrix built to solve the system [98]; or the spatial multigrid method [99]. All these approaches are, however, beyond the scope of this work.

A method for the acceleration of lattice Boltzmann steady-state computations should have the following desirable properties:

- ideal acceleration ratio, which implies a linear relation between acceleration and resolution;

- generalized formulation, so that it can be applied to all flow conditions and to any lattice Boltzmann method;

- simplicity in its implementation, because among two techniques with similar properties the simplest one will be preferentially adopted;

- preservation of the collision-propagation algorithm, which confers some of the most appealing properties to the LB approach for fluid flow simulations (e.g. local computation of the collision); and

- flexibility to be combined with other acceleration or stabilization techniques, or to be ported to variable time-step and/or non-lattice schemes.

Existing acceleration techniques for the collision-propagation lattice Boltzmann scheme do not fulfill every one of these ideal conditions. Body force approaches present some problems for their generalization to recirculating or to complex-flow configurations; they also provide acceleration ratios which are far from the ideal ones. Grid-related techniques are based on quite different principles. For example, multi-block and grid-refinement save time by adapting the resolution of the grid only where it is necessary, their acceleration rate depends on the flow configuration, and a trade-off between computing time and accuracy can be reached. Multigrid techniques applied to lattice Boltzmann are promising but, as occurred in traditional CFD techniques, problems in the prolongation and restriction steps near complex walls have not yet been fully addressed. Finally, preconditioning emerges as a well balanced approach to fulfill all ideal properties, its mayor drawback being the lack of knowledge about its actual stability limits and about the acceleration potential.

Although preconditioning techniques have been extensively used during the last two decades [88], and the explicit lattice Boltzmann collision-propagation algorithm seems to be a perfect candidate, their application has not become widespread. Indeed, only one recent publication [90] is known to the author to relate Navier-Stokes preconditioning schemes and LB. The main problem is the not-so-obvious translation between the LB and NS worlds, specially when importing ideas from NS to LB. Pioneer work in this field was done by Guo et al. [90], who proposed a modification of the quadratic terms of the equilibrium distribution function, adding a free parameter, and related it to preconditioned NS systems. With a linear stability analysis they predicted the stability limits and numerical work confirmed the gain obtained using the new scheme.

The aim of this Chapter is to complete the work existing on this topic by systematically identifying all possible time-derivative preconditioning of Navier-Stokes systems which can be derived from the lattice Boltzmann equation with a modified equilibrium distribution function. Once these preconditioners are obtained, they are analyzed using tools typically applied for Navier-Stokes equations, studying the influence of the preconditioning parameters in the condition number of the system. This is done instead of using stability analysis of the linearized lattice Boltzmann equation, as in a previous publication [90]; thus, complementary information to aid in the construction of preconditioners is obtained. This Chapter starts with Section 4.2, which analyzes the generalized lattice Boltzmann method by Lallemand and Luo [24] (first proposed by d'Humières [23]), and how the parameters which define the scheme must be reduced to achieve isotropy and Galilean invariance of the system. The Navier-Stokes equations derived from the remaining generalized lattice Boltzmann equation are studied. It can be concluded that further simplifications are needed to correctly recover the NS equations. Then, the necessary modifications to build NS precondi-

tioners are performed, and again a reduction of available parameters is needed. This process results in a two-parameter (β-γ) preconditioner, which is split into two different preconditioners, whose condition numbers are studied. Numerical results shown in later sections confirm theoretical deductions.

4.2 Generalized LB method

The generalized lattice Boltzmann equation [23] is constructed in moment space, instead of discrete velocity space, and it is based on a multi-relaxation-time collision operator which allows a different relaxation for each moment. Furthermore, additional adjustable parameters can be defined within the equilibrium moments [24], leading to a generalized hydrodynamics with properties that are optimized by the means of the aforementioned collision-relaxation factors and equilibrium-adjustable parameters.

The generalized two-dimensional model with nine discrete velocities (D2Q9) by Lallemand and Luo [24] is used as the starting point. The equilibrium moments for non-conserved quantities are:

$$e^{eq} = \alpha_2 \rho + \gamma_2 \rho_0 (u^2 + v^2) \,, \tag{4.1a}$$

$$\epsilon^{eq} = \alpha_3 \rho + \gamma_4 \rho_0 (u^2 + v^2) \,, \tag{4.1b}$$

$$q_x^{eq} = \beta_1 \rho_0 u \,, \tag{4.1c}$$

$$q_y^{eq} = \beta_1 \rho_0 v \,, \tag{4.1d}$$

$$p_{xx}^{eq} = \gamma_1 \rho_0 (u^2 - v^2) \,, \text{ and} \tag{4.1e}$$

$$p_{xy}^{eq} = \gamma_3 \rho_0 uv \,. \tag{4.1f}$$

The seven adjustable parameters $\alpha_{2,3}$, β_1 and γ_{1-4}, in conjunction with the nine relaxation factors s_i, define the fluid flow behavior. These relaxation factors are related to some macroscopic properties.

In the work by Lallemand and Luo [24] relationships between the equilibrium free parameters and fluid flow behavior are described. These are summarized next. To eliminate first order effect of the velocity in the bulk viscosity a value of $\alpha_2 = -2\alpha$ and $c_s^2 = 1/3$ (c_s being the sound speed) should be taken. α_3 is a free parameter, but to reduce them to a single parameter α the relation $\alpha_2 = -2\alpha_3$ is chosen. To prevent

shear wave attenuation from having an anisotropic dependence on the velocity, while keeping a free parameter, $\beta_1 = -\beta$ should be chosen. To preserve Galilean invariance (up to first order in velocity) but, additionally, preserving a free parameter, the following relations are used: $\gamma_1 = \gamma_3 = \gamma_a$ and $\gamma_2 = 3\gamma_a$. Finally, to combine all γ_1, γ_2 and γ_3 effects into two parameters (γ_a, γ_b), the relation $\gamma_b = 2\gamma_4/3 - \gamma_a$ is chosen.

Taking into account these considerations, and performing a flow re-scaling using β, the resulting equilibrium moments are:

$$\rho^{eq} = \rho \,, \tag{4.2a}$$

$$e^{eq} = -2\alpha\rho + 3\gamma_a\rho_0(u^2 + v^2) \,, \tag{4.2b}$$

$$\epsilon^{eq} = \alpha\rho - \frac{3}{2}(\gamma_a + \gamma_b)\rho_0(u^2 + v^2) \,, \tag{4.2c}$$

$$j_x^{eq} = \beta\rho_0 u \,, \tag{4.2d}$$

$$q_x^{eq} = -\beta\rho_0 u \,, \tag{4.2e}$$

$$j_y^{eq} = \beta\rho_0 v \,, \tag{4.2f}$$

$$q_y^{eq} = -\beta\rho_0 v \,, \tag{4.2g}$$

$$p_{xx}^{eq} = \gamma_a\rho_0(u^2 - v^2) \,, \text{ and} \tag{4.2h}$$

$$p_{xy}^{eq} = \gamma_a\rho_0 uv \,. \tag{4.2i}$$

Therefore, these equilibrium moments are constructed in such a way that, if the free parameters are canceled in the steady state, the solution obtained preserves all desired properties. Indeed, this implies that until the steady state is reached, these properties are not preserved, which is the mechanism used to accelerate the flow solution by changing its hydrodynamic behavior.

The rescaling made in velocity helps to compare this MRT method with its equivalent SRT, particularly, with its equilibrium distribution function; and it also permits to compare the preconditioned system obtained in Sec. 4.3 with typical preconditioners used in classical methods for the solution of Navier-Stokes equations.

The equilibrium distribution functions f_α^{eq} equivalent to the previous equilibrium moments have the form:

$$f_\alpha^{eq} = w_\alpha \left\{ \alpha\rho + \rho_0 \left[3\beta(\mathbf{e}_\alpha \cdot \mathbf{u}) + \frac{9}{2}\left(\gamma_a(\mathbf{e}_\alpha \cdot \mathbf{u})^2 - \frac{1}{3}\gamma_b \mathbf{u}\cdot\mathbf{u} \right) \right] \right\} . \tag{4.3}$$

Notice that α-subscript in f_α is related with the $\mathbb{R}^9$ space of discrete velocities and has nothing with the parameters α, α_2 and α_3 which modify the ρ-terms.

4.3 Preconditioned Navier-Stokes

Preconditioning has been used in Navier-Stokes equations as a numerical artifact to accelerate the convergence to the steady state solution. This modification of the original equations introduces two improvements related to convergence rate and accuracy. First, the changes introduced in the system are equivalent to replacing the sound speed with a pseudoacoustic speed which helps to reduce the disparity between eigenvalues, and, consequently, increases the convergence rate. The second improvement comes from the re-scaling of viscosity, which provides the correct asymptotic solution to the incompressible Navier-Stokes equation when the Mach number tends to zero.

The standard procedure to recover the Navier-Stokes equations from the Boltzmann one is the Chapman-Enskog expansion [11]. If this is applied to the generalized lattice Boltzmann equation with the equilibrium moments of Eq. (4.2), the Navier-Stokes equations are not obtained, because additional terms appear in both the continuity and momentum equation. The resulting continuity equation reads:

$$\alpha\frac{\partial\rho}{\partial t} + \beta\nabla\cdot(\rho_0\mathbf{u}) + 3(\gamma_a - \gamma_b)\rho_0\left(u\frac{\partial u}{\partial t} + v\frac{\partial v}{\partial t} \right) = 0 . \tag{4.4}$$

To cancel the extra terms $\gamma_a = \gamma_b$ is imposed.

Applying again the Chapman-Enskog procedure with the equilibrium moments of Eq. (4.2), but now with $\gamma_a = \gamma_b = 1/\gamma$, the following equations are obtained:

$$\alpha\frac{\partial\rho}{\partial t} + \beta\nabla\cdot(\rho_0\mathbf{u}) = 0 , \tag{4.5a}$$

$$\beta\frac{\partial(\rho_0\mathbf{u})}{\partial t} + \frac{1}{\gamma}\nabla\cdot(\rho_0\mathbf{u}\mathbf{u}) = -\alpha\nabla p + \beta\nabla\cdot(\rho_0\nu\mathbf{S}) . \tag{4.5b}$$

This set of equations is closed with the state equation; in this case, an equation for a perfect gas, $p = \rho/3$.

The system of Navier-Stokes equations Eq. (1.10) can be rewritten in vector form (not considering the LB preconditioning parameters) as:

$$\frac{\partial\mathbf{U}_c}{\partial t} + \frac{\partial\mathbf{E}}{\partial x} + \frac{\partial\mathbf{F}}{\partial y} = \frac{\partial\mathbf{E}_v}{\partial x} + \frac{\partial\mathbf{F}_v}{\partial y} , \tag{4.6}$$

where $\mathbf{U}_c$ are the conserved variables, $\mathbf{E}_v$ and $\mathbf{F}_v$ are the viscous terms; in conjunction with $\mathbf{E}$ and $\mathbf{F}$, they are defined as:

$$\mathbf{U}_c = (\rho, \rho_0 u, \rho_0 v)^\mathsf{T} ; \tag{4.7a}$$

$$\mathbf{E} = (\rho_0 u, \rho_0 v^2 + p, \rho_0 uv)^\mathsf{T} ; \tag{4.7b}$$

$$\mathbf{F} = (\rho_0 v, \rho_0 uv, \rho_0 v^2 + p)^\mathsf{T} ; \tag{4.7c}$$

$$\mathbf{E}_v = (0, \tau_{xx}, \tau_{xy})^\mathsf{T} ; \text{ and} \tag{4.7d}$$

$$\mathbf{F}_v = (0, \tau_{yx}, \tau_{yy})^\mathsf{T} ; \tag{4.7e}$$

with τ_{ij} being the stress tensor. The right-hand side of Eq. (4.6) represents the viscous term, which are function of the kinematic viscosity ν and bulk viscosity ζ. Aditionally, a vector with the variables in the viscous terms, $\mathbf{U}_v$, is defined as:

$$\mathbf{U}_v = (p, u, v)^\mathsf{T} ; \tag{4.8}$$

Time-derivative preconditioning of system (4.6) can be obtained premultiplying the time-derivative term by a preconditioning matrix $\mathbf{P}_c$. Writing all left-hand-side derivatives of Eq. (4.6) using conserved variables, the preconditioned Navier-Stokes equations are:

$$\mathbf{P}_c \frac{\partial \mathbf{U}_c}{\partial t} + \frac{\partial \mathbf{E}}{\partial \mathbf{U}_c}\frac{\partial \mathbf{U}_c}{\partial x} + \frac{\partial \mathbf{F}}{\partial \mathbf{U}_c}\frac{\partial \mathbf{U}_c}{\partial y} = \frac{\partial \mathbf{E}_v}{\partial x} + \frac{\partial \mathbf{F}_v}{\partial y} . \tag{4.9}$$

To study the advantages introduced by the preconditioning, an analysis of the eigenvalues of the $\mathbf{\Gamma}$ matrices is performed. These matrices are defined from Eq. (4.9), as:

$$\mathbf{\Gamma}_{cx} = \mathbf{P}_c^{-1}\frac{\partial \mathbf{E}}{\partial \mathbf{U}_c} , \text{ and } \mathbf{\Gamma}_{cy} = \mathbf{P}_c^{-1}\frac{\partial \mathbf{F}}{\partial \mathbf{U}_c} . \tag{4.10}$$

The basic aim of preconditioning is to scale the eigenvalues of $\mathbf{\Gamma}$ appropriately, in order to reduce the stiffness of the system. Low Mach number preconditioners must address the stiffness of the problem caused by the difference between the speed of sound and the mean velocity of the flow. As a measurement to quantify this goal, the condition number is used. This is defined as:

$$\text{Condition Number} = max \left| \frac{\lambda_i(\Gamma)}{\lambda_j(\Gamma)} \right| ; \tag{4.11}$$

where λ_i and λ_j are two different eigenvalues of $\mathbf{\Gamma}$. The closer to 1.0 the condition number is, the better preconditioned the system will be.

To construct a time-derivative preconditioned system from Eq. (4.5) it is necessary to manipulate this expression to include all parameters in the temporal term. To exemplify this procedure the particular case of $\beta = 1$ and $\gamma = 1$ is taken; thus, only the α parameter remains. As all the terms not influenced by α are multiplied by β or by $1/\gamma$, the α-preconditioner is equivalent to a β-γ-preconditioner where $\beta = 1/\gamma$. Indeed, the same conclusion can be reached from the analysis of the equilibrium distribution function, Eq. (4.3). Thus, the general case of a β-γ-preconditioner and its particular cases are analyzed.

4.3.1 β-γ-preconditioning

Taking into account all the previous considerations a set of equilibrium moments that is modified by two free parameters is obtained:

$$\rho^{eq} = \rho \,, \tag{4.12a}$$

$$e^{eq} = -2\rho + 3\rho_0(u^2 + v^2)/\gamma \,, \tag{4.12b}$$

$$\epsilon^{eq} = \rho - 3\rho_0(u^2 + v^2)/\gamma \,, \tag{4.12c}$$

$$j_x^{eq} = \beta\rho_0 u \,, \tag{4.12d}$$

$$q_x^{eq} = -\beta\rho_0 u \,, \tag{4.12e}$$

$$j_y^{eq} = \beta\rho_0 v \,, \tag{4.12f}$$

$$q_y^{eq} = -\beta\rho_0 v \,, \tag{4.12g}$$

$$p_{xx}^{eq} = \rho_0(u^2 - v^2)/\gamma \,, \text{ and} \tag{4.12h}$$

$$p_{xy}^{eq} = \rho_0 uv/\gamma \,. \tag{4.12i}$$

These equilibrium moments lead to preconditioned Navier-Stokes equations of the form:

$$\frac{1}{\beta}\frac{\partial\rho}{\partial t} + \nabla\cdot(\rho_0\mathbf{u}) = 0 \,, \tag{4.13a}$$

$$\beta\,\gamma\frac{\partial(\rho_0\mathbf{u})}{\partial t} + \nabla\cdot(\rho_0\mathbf{uu}) = -\nabla p^* + \nabla\cdot(\rho_0\nu\mathbf{S}) \,; \tag{4.13b}$$

with the following preconditioning matrix in the conserved variables:

$$\mathbf{P}_c = \begin{pmatrix} \frac{1}{\beta} & 0 & 0 \\ 0 & \beta\,\gamma & 0 \\ 0 & 0 & \beta\,\gamma \end{pmatrix} . \tag{4.14}$$

In these NS equations, a modified pressure is used:

$$p^* = \gamma \frac{\rho}{3} , \tag{4.15}$$

and a redefinition of viscosity is needed:

$$\nu = \beta\,\gamma \frac{1}{3} \left(\frac{1}{s_\nu^*} - \frac{1}{2} \right) ; \tag{4.16}$$

with

$$s_\nu^* = \frac{1}{\tau_p} = \left[\frac{1/s_\nu - 1/2}{\beta\,\gamma} + \frac{1}{2} \right]^{-1} ; \tag{4.17}$$

being the effective relaxation parameter, and where star-superscript accounts for preconditioned values. Additionally, to correct the effect of flow re-scaling, momentum is corrected as:

$$\rho_0 \mathbf{u} = \frac{\mathbf{j}^{eq}}{\beta} . \tag{4.18}$$

The corresponding $\mathbf{\Gamma}$ matrix of this system in conserved variables and x direction is:

$$\mathbf{\Gamma}_{cx} = \begin{pmatrix} 0 & \beta & 0 \\ \frac{1}{3\beta\,\gamma} & \frac{1}{\beta\,\gamma} u & 0 \\ 0 & 0 & \frac{1}{\beta\,\gamma} u \end{pmatrix} ; \tag{4.19}$$

which has the following eigenvalues:

$$\lambda_{\mathbf{\Gamma}_{cx}} = \frac{1}{\beta\gamma} \left\{ u, \frac{1}{2} u \pm \frac{1}{2} \sqrt{u^2 + \frac{4}{3}\,\beta^2\,\gamma} \right\} . \tag{4.20}$$

To compare the preconditioning matrix (4.14) with typical preconditioning matrix used in Navier-Stokes equations, a system where $\rho_0 = \rho$ is considered and $\mathbf{P}_c$ is transformed into viscous variables:

$$\mathbf{P}_v = \frac{\partial \mathbf{U}_c}{\partial \mathbf{U}_v} \mathbf{P}_c = \begin{pmatrix} \frac{3}{\beta} & 0 & 0 \\ \frac{3u}{\beta} & \rho\,\beta\,\gamma & 0 \\ \frac{3v}{\beta} & 0 & \rho\,\beta\,\gamma \end{pmatrix} . \tag{4.21}$$

This preconditioning matrix was first proposed by Turkel [86], and it is equivalent to the preconditioner by Choi and Merkle [87] and also to the Weiss and Smith [100]

one. For selecting parameters for this preconditioner, Turkel [86], Choi and Merkle [87] suggest:

$$\begin{aligned} \beta &= \beta_{min}^2 \quad (Ma \leq \beta_{min}) \,, \\ \beta &= Ma^2 \quad (Ma > \beta_{min}) \,; \end{aligned} \tag{4.22}$$

but for the lattice Boltzmann method, taking into account stability criteria, $\beta_{min} \approx 2u_0$ is chosen, u_0 being the reference velocity.

4.4 Condition Number analysis

The condition number is used in this Chapter to study the performance of preconditioners. This number is constructed as indicated in the Eq. (4.11), and using the eigenvalues from Eq. (4.20). The reference case is the non-preconditioned lattice Boltzmann method, eigenvalues of which are recovered by setting $\beta = \gamma = 1.0$. Figure 4.1 displays values of the condition number for this method as a function of the velocity u; the reference density has been set $\rho_0 = 1.0$ here and in all the following computations. When a condition number smaller than those on this curve is obtained by preconditioning, the convergence behavior will be improved.

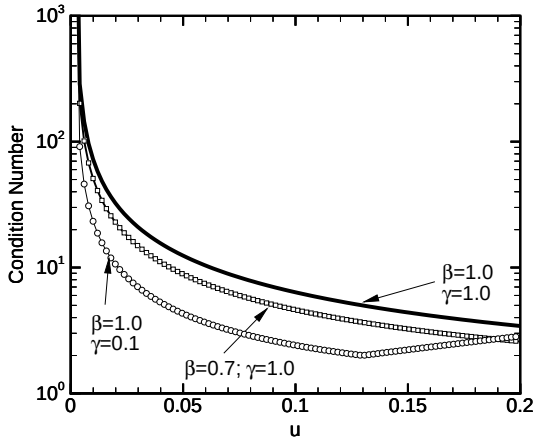

Figure 4.1: Condition number as a function of velocity for the non-preconditioned ($\beta = \gamma = 1.0$), the β-preconditioned and the γ-preconditioned lattice Boltzmann method.

An important remark regarding the condition number dependency on velocity is that, as the Mach number tends to zero, the condition number grows potentially, preventing a fast solution of a fluid flow simulation. On the other hand, when a β-γ-preconditioner is used, condition numbers are reduced for all velocities, with smaller

values as the Mach number increases, as in the reference method. Information for the β-γ-preconditioner can be extracted from Fig. 4.2.

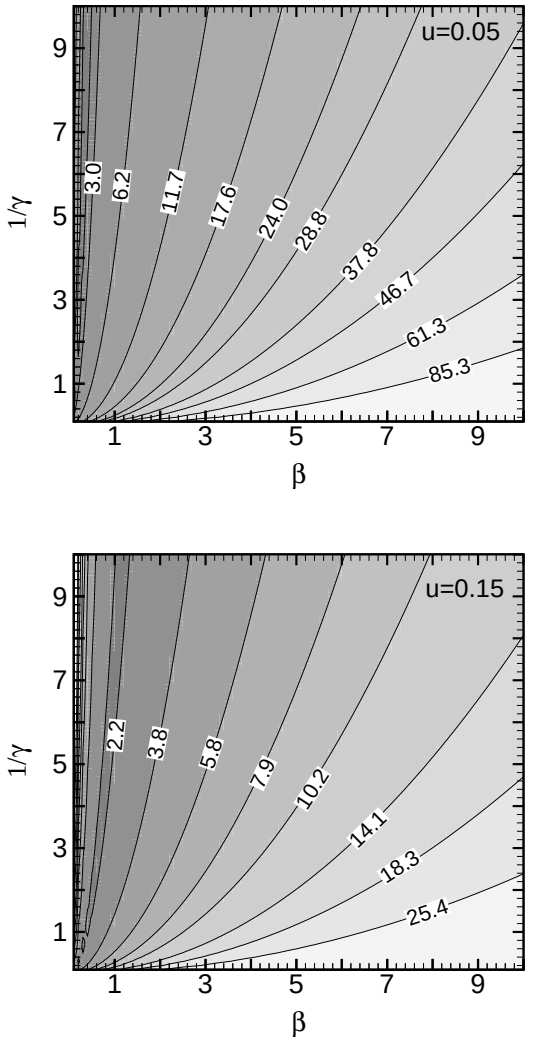

Figure 4.2: Condition number at two different velocities for the β-γ-preconditioner.

Additional information is given in Fig. 4.3, where a condition number map is plotted as a function of velocity for the case of $\beta = 1/\gamma$, which would be equivalent to an α-preconditioner. In this case, low condition numbers are obtained for high velocities, close to the low-Mach-number limit. This is because of the natural dominance of the β-preconditioner over the γ-preconditioner, due to the dependence on u in the first case and on u^2 in the second.

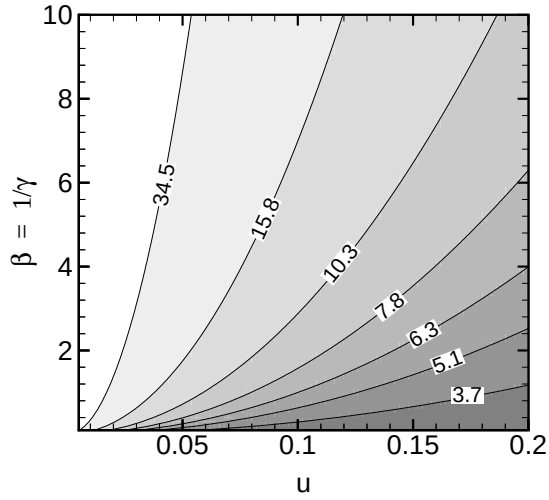

Figure 4.3: Condition numbers as a function of velocity for the $\beta = 1/\gamma$ preconditioner.

A particular case is found when $\gamma = 1.0$. For this situation a linear dependency of the condition number with β exists, with lower condition numbers as β decreases and the Mach number increases. A possible application of this preconditioner would arise in Stokes flows (e.g. porous media), where the quadratic term of the equilibrium distribution function is suppressed, and the β parameter could be used to reduce calculation time to steady state.

An additional interesting case emerges when $\beta = 1.0$, and the preconditioner proposed by Guo et al. [90] is recovered. For this case, as the Mach number decreases, smaller values of γ are needed to maintain a lower condition number; but the lowest γ will be limited by stability criteria [90]. This reveals the importance of the stability analysis to determine the applicability limits. These limits are investigated numerically for both the γ and β-preconditioner in the next Section.

4.5 Numerical results

The previous results are verified in this section using as a test case the lid-driven cavity-flow [101] with a Reynolds number $Re = (Nu_0)/\nu = 100$, $N = 129$, and reference velocity $u_0 = 0.05$. Therefore, $Ma = u_0/c_s = 0.087$ and $s_\nu = 1.448$. The bounce-back boundary condition is used at walls, and for the moving lid a momentum-transfer boundary condition [38] is applied (i.e. UBB, see Chapter 2 and 3), where u_0 must be rescaled according to β. The numerical results for velocity and pressure

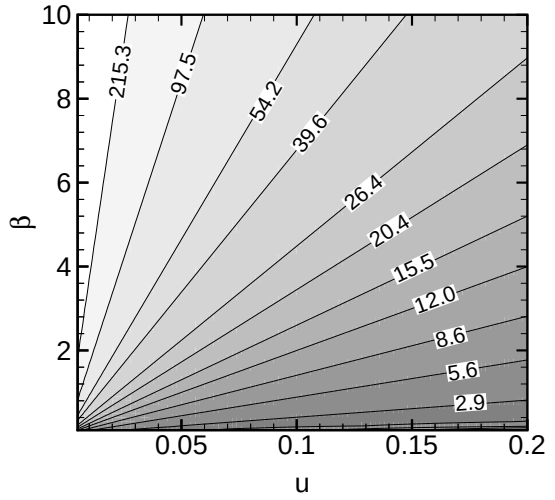

Figure 4.4: Condition numbers as a function of velocity for the β-preconditioner.

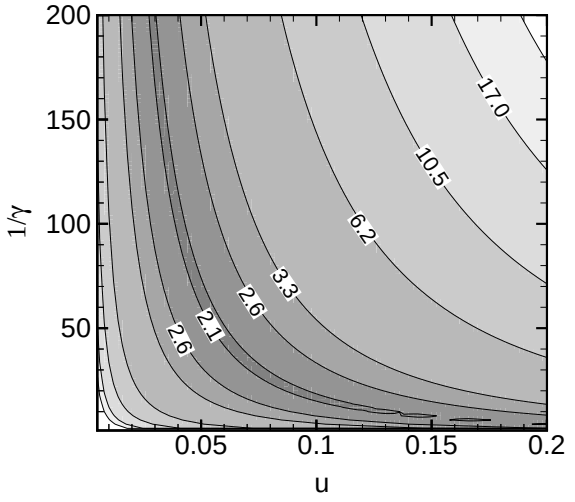

Figure 4.5: Condition numbers as a function of velocity for the γ-preconditioner.

obtained with the non-preconditioned and preconditioned LB for this test problem compare well with incompressible reference data, and evidence or any further discussion are omitted. It will nevertheless recorded that preconditioning results are more accurate, because of the better asymptotics at low Mach number [88, 102]. The convergence behavior is measured with the velocity residual, computed as the error with the L_2 norm of the velocity vector. Results using different pairs of values for β and γ are shown in Fig. 4.6. The velocity residuals shown are indicative of the time needed to reach the steady state with preconditioned and non preconditioned LB methods.

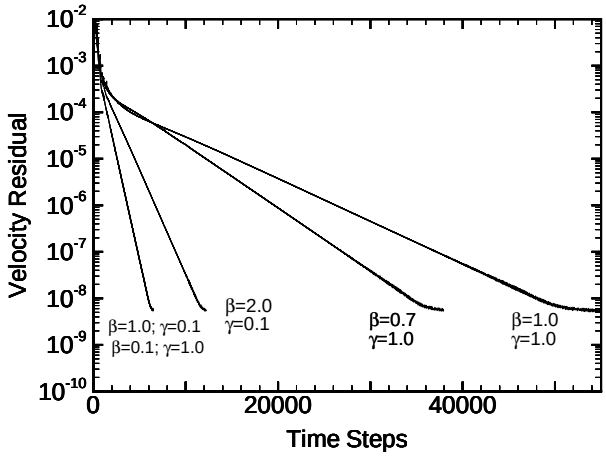

Figure 4.6: Evolution of velocity residuals for the non-preconditioned LB method ($\beta = \gamma = 1.0$) and different versions of the preconditioned LB. The relaxation factor is $s_\nu = 1.448$ for all cases.

Table 4.1: Condition number for different β-γ values and convergence rate obtained in numerical simulations of the test case.

β	γ	CN	$s_\nu^\star = 1/\tau_p$	Time Steps Steady State	% Time Reduction
1.0	1.0	12.0	1.448	55700	0.0
0.7	1.0	8.7	1.295	37900	32.0
2.0	0.1	7.8	0.688	12160	78.2
0.1	1.0	4.0	0.416	6295	88.7
1.0	0.1	4.1	0.416	6290	88.7

The slope of the convergence lines is directly related to the condition number computed as in Section 4.3. In Table 4.1 condition numbers and time steps to reach the steady state are shown for the same cases as in Fig. 4.6. An important point that arises from this Table is that when the stability limit is reached for both β and γ

preconditioners (last two lines in the Table) the same condition number is obtained and the same convergence behavior is observed.

It is also important to remark that the condition-number analysis gives no information on the stability of the system, and for this reason not all points in Figs. 4.1-4.5 are feasible. In order to obtain the stability limits for the preconditioning presented, a numerical study has been performed. Results (Fig. 4.7) show that γ and β have a lower limit (the upper limit of $1/\gamma$ is plotted), and for both the condition number is a minimum at these limits.

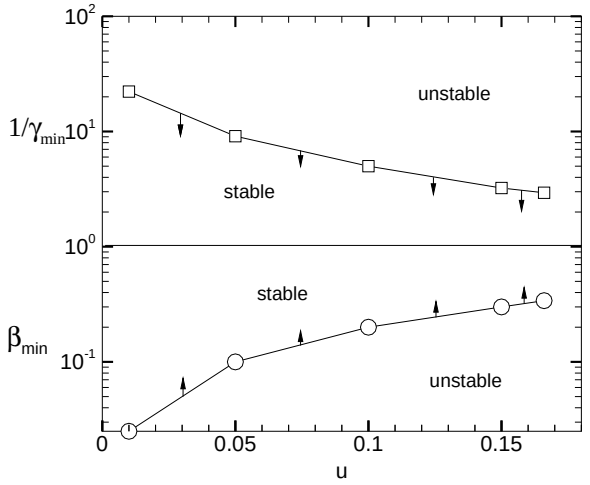

Figure 4.7: Stability limits for the β- and γ-preconditioners.

The condition numbers at the stability limits for the β- and γ-preconditioners are plotted in Fig. 4.8. It is an interesting fact that they are identical except at very low speeds, where the β-preconditioner could yield a better speed-up. This is related to diffusive nature of low speed flow and the $O(u)$ dependence of these terms, which are scaled by β.

4.6 Conclusions

From the study presented in this work and in [90], the complete process to be applied to the study of other new preconditioning schemes for lattice Boltzmann methods can be derived. It should be based on: (i) a Chapman-Enskog procedure to properly recover some preconditioned-like Navier-Stokes system; (ii) a study of the condition number to asses the potential of the method; and (iii) a linear analysis to establish the stability limits.

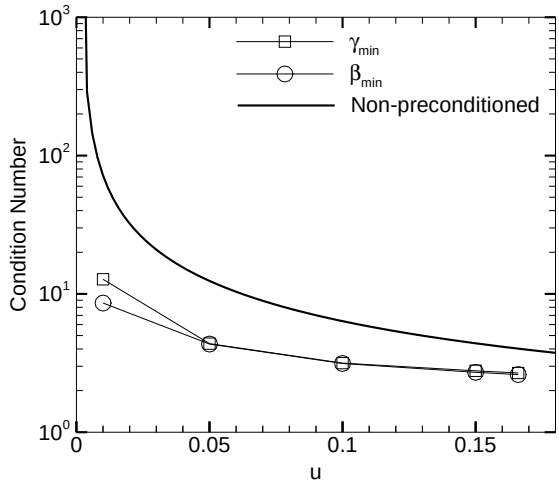

Figure 4.8: Condition numbers obtained at the stability limits for β and γ-preconditioners.

Using this method, a two-parameter β-γ-preconditioner, Eq. (4.12), (4.15) and (4.16), for the lattice Boltzmann equation has been developed considering the Navier-Stokes preconditioning. Specifically, a new preconditioner based on the modification of the linear terms u of the equilibrium distribution function (β-preconditioner) is shown to improve γ-preconditioned results at very low Mach numbers ($Ma < 0.05$). Additionally the method is extended to the generalized MRT collision operator (regarding the original work by Guo et al. [90]) and a theoretical analysis is performed based on the condition number of the Navier-Stokes system recovered from the lattice Boltzmann equation. A comparison of the β-γ-preconditioners with the typical ones used in Navier-Stokes equations reveals that for a particular selection of LB parameters, a NS preconditioner [86, 87, 100] is recovered.

5

Optimal preconditioning

5.1 Introduction

Preconditioning is defined, in a general sense, as the change, or conditioning, of eigenvalues of a system of equations in order to obtain an improvement in its behavior. Therefore, preconditioning can adopt different meanings depending on the system considered or on the improvement desired. In the case of lattice Boltzmann simulation of fluid flow, a definition of preconditioning is needed to avoid misunderstandings. Indeed, three different cases of preconditioning are analyzed in this work: (i) time-derivative preconditioning of Navier-Stokes equations for fluid flow acceleration and its correct asymptotic recovering of the incompressible solution; this is the classical application in CFD, and is applied in lattice Boltzmann methods through a modification of the equilibrium distribution function; (ii) time-derivative preconditioning of the lattice Boltzmann equation, which is compared in this work to under-relaxed schemes; and (iii) the multi-relaxation-times collision operator, which can be seen as a preconditioning of the collision operator in order to improve the stability of the system.

The main objective of the present Chapter is to provide theoretical and numerical results which allow to define the optimal use of the γ-preconditioner. The γ-preconditioner is selected due to its efficiency and simplicity: it works as well as the β-preconditioner for most of the Mach-number range and, the most importantly, the implementation of boundary conditions is easier as it does not involve the rescaling of u-terms. For the sake of simplicity, the study performed is based on the two-dimensional $D2Q9$, but it can be straightforwardly expanded to other lattices. The

three-dimensional $D3Q19$ preconditioned method is in the Appendix B.

5.2 Linear stability analysis

Linear stability analysis, see Sec. 1.3, is a useful tool to study stability of linear and linearized systems. It has been previously used to study the stability of lattice Boltzmann methods [42], and to optimally construct new lattice Boltzmann models [24]. Additionally, it has been used as supplementary tool for the design of preconditioners for both, Euler and Navier-Stokes system of equations [87, 88]. In this section this technique is applied to the analysis of optimal preconditioned lattice Boltzmann schemes.

5.2.1 Lattice Boltzmann equilibrium-based preconditioner

After the work by Guo et al. [90], the general guidelines for the stability criteria of preconditioned SRT lattice Boltzmann methods are known. These are: (i) τ_p must be greater than one-half; (ii) γ must be greater than a certain value which depends on the other parameters (u_i, k_i, τ_s); and (iii) as γ increases, so does the maximum speed for a stable method.

To study the γ-preconditioner, the linear stability analysis for LB MRT methods described in Sec. 1.3 is followed. The eigenvalues of the linearized evolution operator $L_{\alpha\beta}$ are first computed for each configuration defined, and the maximum, λ_{max}, of these values is selected, which dictates the stability of the system. To analyze the results, λ_{max}-iscontours, or stability maps, are plotted for both the MRT and SRT methods. These stability maps summarize a lot of information that otherwise were difficult to analyze.

For the $D2Q9$ γ-preconditioner MRT method the resulting $G_{\alpha\beta}$ matrix, which is used to build the linearized evolution operator, is :

$$G_{\alpha\beta} = \begin{pmatrix} 0 & 0 & 0 & 0 & 0 & 0 & 0 & 0 & 0 \\ -2s_e & -s_e & 0 & 6s_e u_0/\gamma & 0 & 6s_e v_0/\gamma & 0 & 0 & 0 \\ s_\epsilon & 0 & -s_\epsilon & -6s_\epsilon u_0\gamma & 0 & -6s_\epsilon v_0/\gamma & 0 & 0 & 0 \\ 0 & 0 & 0 & 0 & 0 & 0 & 0 & 0 & 0 \\ 0 & 0 & 0 & -s_q & -s_q & 0 & 0 & 0 & 0 \\ 0 & 0 & 0 & 0 & 0 & 0 & 0 & 0 & 0 \\ 0 & 0 & 0 & 0 & 0 & -s_q & -s_q & 0 & 0 \\ 0 & 0 & 0 & 2s_\nu u_0/\gamma & 0 & -2s_\nu v_0/\gamma & 0 & -s_\nu & 0 \\ 0 & 0 & 0 & s_\nu v_0/\gamma & 0 & s_\nu u_0/\gamma & 0 & 0 & -s_\nu \end{pmatrix}. \quad (5.1)$$

The values λ_{max} are first analyzed for the whole range of wave numbers $k_x \in [0, \pi]$, and for $\gamma \in [0, 1]$. Results for $U = (0.0577, 0)$ and $\tau_s = 0.5017$, which are equivalent to $Re_x = (u_0 \delta x)/\nu = 100$ and $Ma = 0.1$, are plotted in Fig. 5.1 for the SRT collision operator and also for the MRT one. The SRT relaxation parameter τ_s is computed with $N = 1$; and the MRT relaxation coefficients are: $s_\nu = 1/\tau_p$ and $s_e = s_\epsilon = s_q = 1.0$. Figure 5.1 displays the isocontours of λ_{max}, and the areas with $\lambda_{max} > 1$ (unstable) are shaded in light-gray. A first remark is that there exists a stability limit for γ (γ_{min}), which is approximately the same for SRT and MRT. This γ_{min} is defined by the upper limit of the isocontour λ_{max}=1.0; and it depends on local Reynolds number Re_x and Mach number Ma. The main difference between the SRT and MRT collision operators is that for γ values equal to or greater than the stability limit, λ_{max} will be smaller for MRT at every wave number, which means a better stability condition.

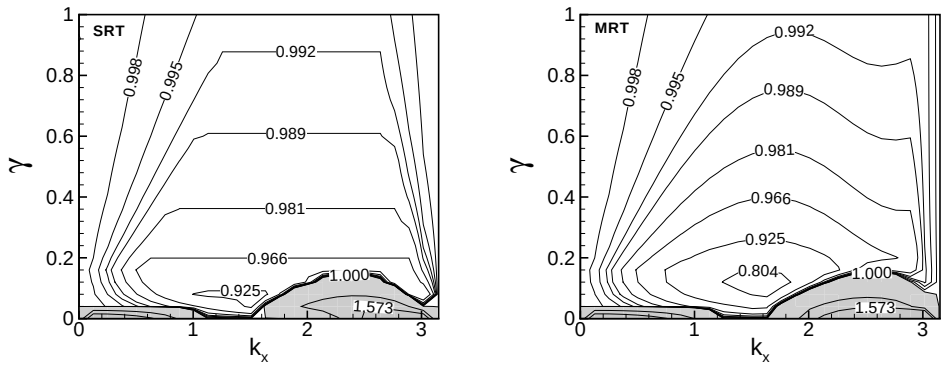

Figure 5.1: Iso-contours of maximum eigenvalue on the γ-k_x plane for the SRT (left) and MRT (right) collision operators.

To analyze the influence of the velocity u_i on the stability, λ_{max} values for different Ma and γ are plotted in Fig. 5.2. The value of τ_s is fixed at 0.502, and τ_p is computed from as a function of γ and τ_s; the MRT relaxation parameters others than $s_\nu = 1/\tau_p$, are fixed to 1.0. Results are plotted within the incompressibility limit $Ma \in [0, 0.3]$. For a given Ma number, the γ_{min} limit turns out to be approximately the same for both collision operators, but with better stability conditions for MRT. Additionally, the plots reveal that the relation between the γ_{min} limit and the Mach number is linear.

Applying the stability analysis to the SRT and MRT preconditioned schemes, based on the preconditioned equilibrium distribution function, the stability criteria [90] can be redefined in the following way: (i) as $\lambda_{max} = 1 - 1/\tau_p$ in the limit when $k_i = 0$, the preconditioned relaxation parameter τ_p must be greater than one half, or equivalently,

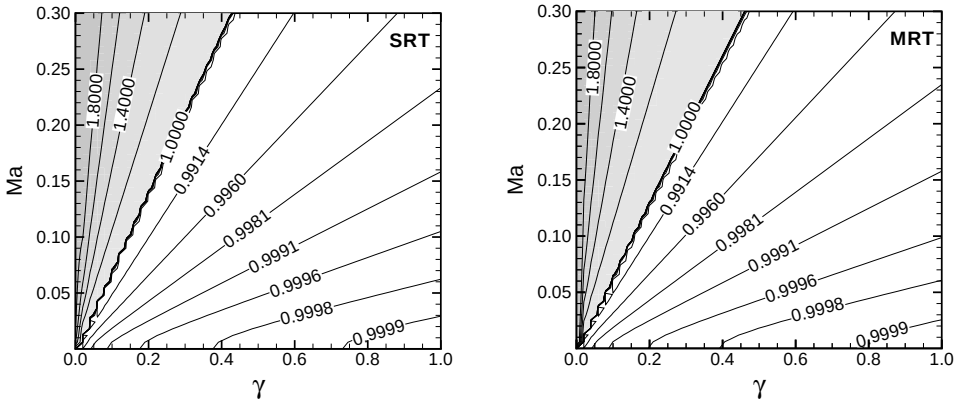

Figure 5.2: Maximum eigenvalue in the whole range of k_x for different γ-Ma values for the SRT and MRT collision operators.

$\tau_s > 1/2$ and $\gamma > 0$ to have a stable preconditioned lattice Boltzmann scheme; (ii) there exists a γ_{min} point close to the stability limit where the λ_{max} is the lowest, meaning grater stability, and this stability is better for MRT; (iii) there is a linear relation between the γ_{min} limit and the Mach number.

5.2.2 Optimal preconditioning parameters

To analyze a possible *a priori* selection of an optimal value for the preconditioning parameter, γ_{op}, a graphical representation of the relationship between γ, τ_s and τ_p is built, Fig. 5.3. Two superimposed relations are plotted: the first one is from the linear stability analysis and it shows the maximum eigenvalue of $L_{\alpha\beta}$ as a function of the preconditioning relaxation parameter τ_p and of γ; the second relationship is the one arising from the Eq. (4.17), which can be expressed for the γ-preconditioner as:

$$\gamma = \frac{\tau_s - 1/2}{\tau_p - 1/2} \,. \tag{5.2}$$

While an analytical expression for γ_{op} could be useful, it is not possible to obtain one from linear stability analysis, and only indications, based on the results, can be provided. Thus, γ_{op} may be restricted between the minimum allowable preconditioning parameter γ_{min} due to stability criteria, and the set of all points on the $\tau_p - \gamma$ plane where for each fixed τ_s the minimum value of λ_{max} is found. This may be expressed as:

$$\gamma_{op}(Re_x, Ma) \in [\gamma_{min}, \gamma[\tau_s(Re_x, Ma), min.\lambda_{max}(Re_x, Ma, s_\alpha)]] \,, \tag{5.3}$$

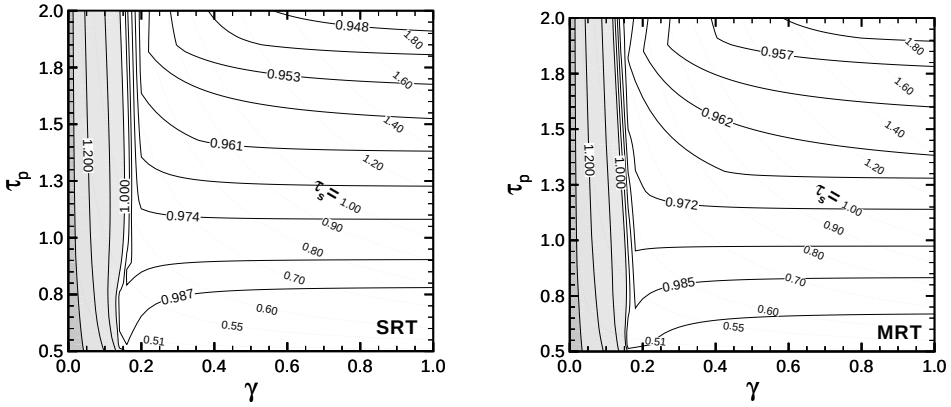

Figure 5.3: Maximum eigenvalue in the whole range of k_x for different γ-τ_p values for the SRT and MRT collision operators. Iso-contours of τ_s as a function of γ and τ_p are plotted with dotted lines.

where γ_{min} can be approximated by data from Fig. 5.2, and ignoring the Re_x dependence, as:

$$\gamma_{min} = \frac{\tau_s(Ma) - \frac{1}{2}}{\tau_p^{max}(Ma) - \frac{1}{2}} \approx 1.5Ma\,. \tag{5.4}$$

In preconditioned lattice Boltzmann simulations using the scheme proposed, the gain obtained can be viewed as a change from the relaxation parameter, τ_s, which determines the actual Reynolds of the flow, to a fictitious preconditioning relaxation parameter, τ_p, which accounts for the behavior of the simulation. Thus, the larger τ_p is, the more stable and better preconditioned the system will be; however large τ_p for a given τ_s fall beyond the stability limit. On the other hand, for large τ_s values, the optimal point could be displaced to γ values larger than γ_{min} because a compromise between large τ_p and small λ_{max} must be reached. This is the case of the microchannel analyzed in Sec. 5.5

5.2.3 Global map of stability limits

In this Section the limits of the MRT preconditioned scheme are explored by means of a more general stability analysis ($\gamma \in (0, \infty)$), and a study of the condition number (CN) of the recovered Navier-Stokes equation.

Figure 5.4 summarizes the results from the analysis. First, in the top-right part of Fig. 5.4 stability maps of τ_s vs. $\gamma \in (0, 1)$ are plotted for different Mach numbers between $Ma = 0$ and $Ma = 1.2$. The analysis performed above is for the incompressible area of this part of the diagram. Isocontours of λ_{max} are plotted in a gray shade

where the method is stable (darker shades indicating more stable schemes), and unstable regions are drawn in white. The main observation is that as the Mach number increases, the stable area is reduced and γ_{min} linearly increases. Additionally, for $Ma \to 0$ the stability contour becomes linear. To complement this information, the ratio between the condition number of each Ma-γ point and the condition number for this point at $\gamma = 1$ (CN/CN_0) is plotted under the stability map. Grey areas indicate acceleration regions, where the convergence rate to the steady state is faster the darker the shade is. The zone of greater acceleration is the same as the one for γ_{min}, and therefore, stabilization and acceleration can be achieved at the same time.

On the left-hand side of Fig. 5.4, the same relations are plotted for $\gamma \in (1, \infty)$. Some interesting remarks can be made. The first one is that the stability of the method is now greater, as it remains stable beyond $Ma = 1$; however, for the incompressible limit, the method is ill-conditioned, and no acceleration is obtained. As the flow is isothermal, the high-Ma region has no physical interest, albeit its study can assist in the development of stabilized methods for lattice Boltzmann compressible flows. An advantage derived from the use of $\gamma \in (1, \infty)$ is that stable and accurate methods can be obtained for $\tau_s > 2$ which is the upper limit dictated by numerical restrictions; this is the case for flows at at very low Reynolds numbers such as Stokes flows (see Sec. 5.4).

5.3 Two-dimensional test case I: lid-driven cavity

A lid-driven cavity flow is chosen as two-dimensional test-case due to its well-researched steady-state solution [101], and to the absence of open boundaries. The present analysis focuses on three aspects: convergence rate, stability, and accuracy. Additionally, the influence of the Reynolds number on the performance of the preconditioner is studied, as is the effect of under-relaxation of f_α within the preconditioned scheme. The domain dimensions and other flow characteristics are defined below for each case. For wall boundary conditions, the half-way bounce-back scheme is used, with the momentum transfer correction of Bouzidi et al. [38] for the moving lid.

5.3.1 MRT versus SRT preconditioned LBE

The performance of the MRT and SRT preconditioned methods is first compared. The study of the convergence behavior is done by monitoring the residual errors of the velocity field at each temporal step, the residual being computed with the L_2-norm. These residuals are shown in Fig. 5.5 for four lattice Boltzmann schemes to compare the convergence rate. As reference case the following is chosen: $Re = 1000$, $Ma = 0.1$ and an $N \times N$ domain with $N = N_x = 129$. Therefore $u_0 = 0.057735$ and $\tau_s = 0.501732$. The main conclusion from Fig. 5.5 is that the optimally-preconditioned

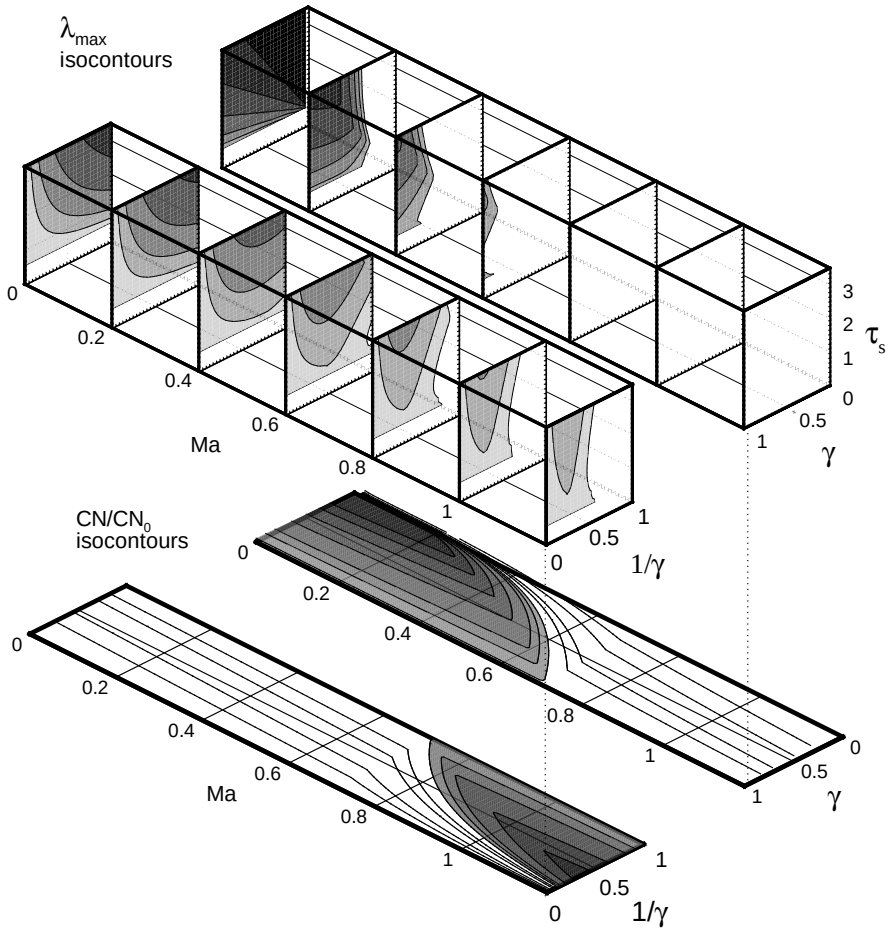

Figure 5.4: (Top) Global map of λ_{max} for different values of Ma and τ_s and for the whole range of γ (above). (Bottom) Isocontours of the ratio between the condition number (CN) and the condition number for $\gamma = 1$ (CN_0) for the same Ma and γ interval.

MRT is the method which first reaches convergence to machine accuracy (after approximately $4 \cdot 10^4$ time steps), while SRT methods remain far from this goal after 10^5 time steps.

As a result of the algorithmic differences between the SRT and MRT methods, the smallest number of time steps required by the MRT does not necessarily imply greater performance efficiency than SRT. The millions of lattice nodes updated per second (MLUPS) is used as a measure to compare performance. MLUPS include the time needed to calculate the collision, the propagation and the velocity residuals. The comparison between MRT and SRT for this two dimensional problem is shown in Fig. 5.6. Simulations to compare performances were carried out on an AMD Athlon 64 at 1.8GHz and with 512KB of cache memory. Results indicate that the SRT collision operator is approximately 4% faster on average than MRT. This is not a significant difference, therefore the comparison between SRT and MRT on the same time scale in Fig. 5.5 is representative of the gain in overall performance. From Fig. 5.6, it can be concluded that efficiencies of MRT and preconditioned MRT are similar over the entire range of N, which indicates that the preconditioning method suggested does not add any additional, significant algorithmic complexity. The remaining results shown in Fig. 5.6 are for the under-relaxed scheme that will be discussed in Sec. 5.3.3.

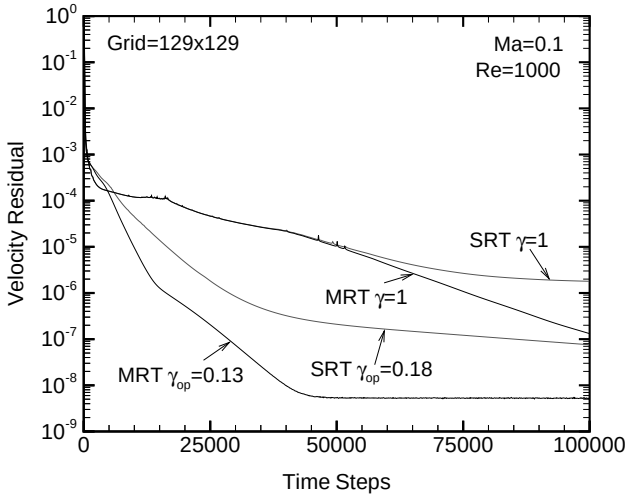

Figure 5.5: Velocity residuals for the lattice Boltzmann equation with SRT and MRT, and optimal preconditioned versions of both collision operators. The used values of γ in each case are indicated.

A visual indication of the stability improvement achieved with preconditioning is shown in the pressure contours of Fig. 5.7. Using either the preconditioned SRT, the MRT or the preconditioned MRT schemes result in a very significant reduction

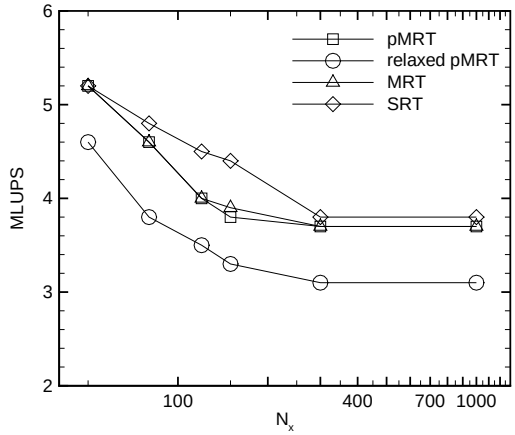

Figure 5.6: Millions of lattice update per second (MLUPS) as a function of the number of cells. The total number of cells is: $N_{total} = N_x^2$.

in the pressure oscillations. However, with both preconditioned SRT and standard MRT some small oscillations do remain close to some the cavity corners; these are completely suppressed with the preconditioned MRT scheme proposed.

The accuracy of the results is measured against the benchmark simulations by Botella and Peyret [103]. This comparison is shown in Fig. 5.8. A relatively coarse lattice dimension of $N = 129$ was chosen to highlight differences in accuracy between non-preconditioned and preconditioned schemes, the latter ones providing more accurate results.

5.3.2 Effect of Re on the preconditioning performance

To study the effect of parameters which define the flow (Re, Ma, N and s_ν) on the MRT preconditioning performance, time steps needed to reach machine accuracy are analyzed versus the Reynolds number as a function of Ma, N and τ_s . This accuracy is $5 \cdot 10^{-9}$ for the conserved macroscopic variables ρ and u_i. Three parametric studies are performed, for the variation respectively of the number of lattice nodes, of the Ma number, and of $s_\nu = 1/\tau_s$. Additionally, the dependence of the optimal value of γ as a function of these parameters is also analyzed.

Figure 5.9 (left) displays the time needed to reach machine accuracy as the number of lattice nodes is increased (for $Ma = 0.1$ and $s_\nu = 1/\tau_s = 1/0.55$). This time increases with the number of nodes for both preconditioned (γ_{op}) and non-preconditioned ($\gamma = 1.0$) MRT methods, but the time is always longer for the non-preconditioned scheme and the difference increases as the dimension does. For the case of the Ma dependency,

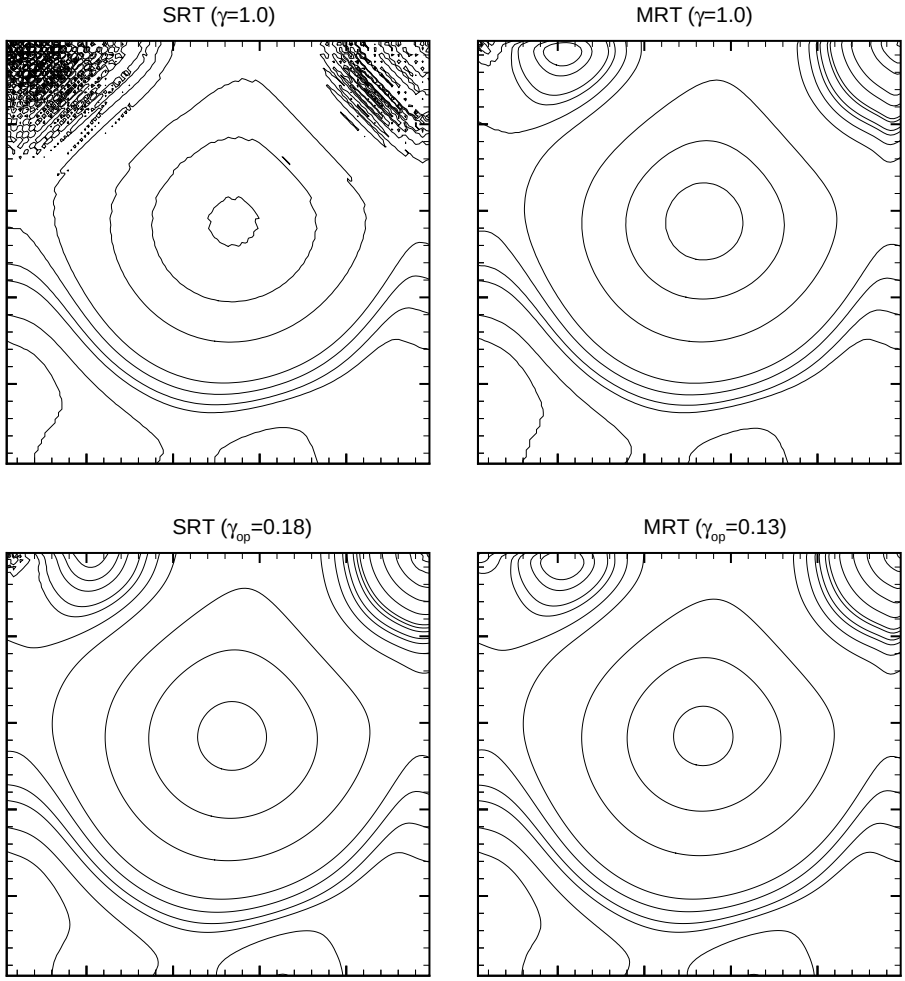

Figure 5.7: Pressure contours taken at a velocity-residual level of 10^{-5} for the same cases as in Fig. 5.5. $N = 129$, $Re = 1000$ and $Ma = 0.1$.

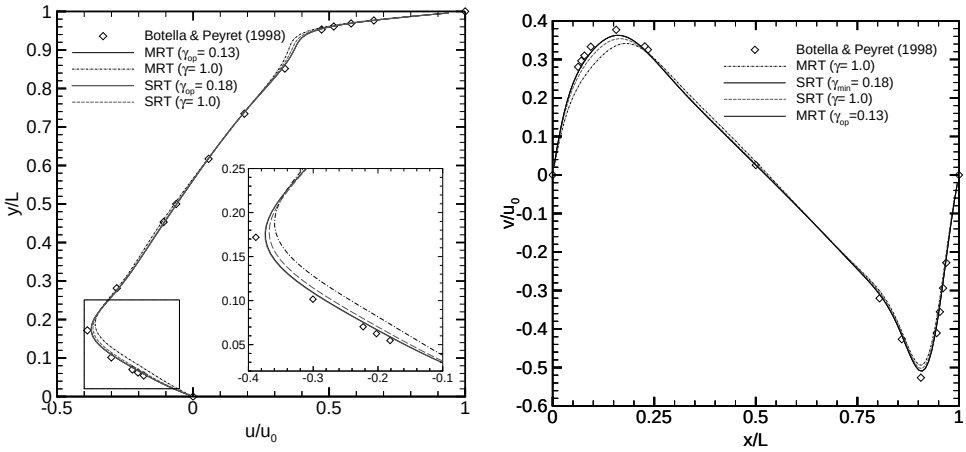

Figure 5.8: Comparison with calculated reference data [103], for the same cases as in Figs. 5.5 and 5.7, of horizontal velocity component u (left), and vertical velocity component v (right).

with $N = 120$ and $s_\nu = 1/\tau_s = 1/0.55$, Fig. 5.10 (left), the trend is different for preconditioned and non-preconditioned schemes. The latter requires a larger Ma number to reduce the computational time, but this implies loosing accuracy due to compressibility effects. The preconditioned method reduces the calculation time as the Mach number decreases, and therefore the difference between both is maximal when $Ma \to 0$. From Fig. 5.11 (left) it can be concluded that time needed to reach machine accuracy increases with both methods with s_ν, for $Ma = 0.1$ and $N = 120$, with the preconditioning MRT providing the shortest times along the entire range.

Summarizing from these results, the best improvements with the MRT preconditioner are obtained at moderate Reynolds numbers, $\tau_s = 1/s_\nu = (0.53, 0.55)$, with low velocities, $Ma < 0.1$, and high-resolution meshes. With these parameters, errors due to compressibility and discretization will also be reduced, and the problem remains well within the stability region $\tau_s > 0.5$.

The evolution of γ_{op} as a function of N, Ma and $s_\nu = 1/\tau_s$ is shown in right-hand-side plots of Figs. 5.9, 5.10 and 5.11. The optimal value has no dependence on $s_\nu = 1/\tau_s$, a weak dependence on N and linear dependence on Ma. The nearly linear relation obtained from the stability analysis Fig. 5.2 is plotted for comparison in Fig. 5.10, as well as the line $\gamma_{op} = Ma$.

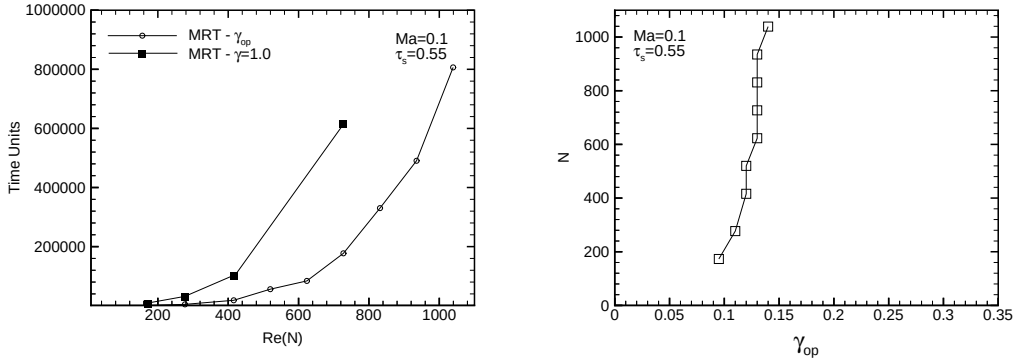

Figure 5.9: (Left) Time units (referred to $N = 120$ for normalization) needed to reach machine accuracy, as a function of Reynolds number which varies by changing N; (Right) optimal value of the preconditioning parameter, γ_{op}, as a function of the number of cells.

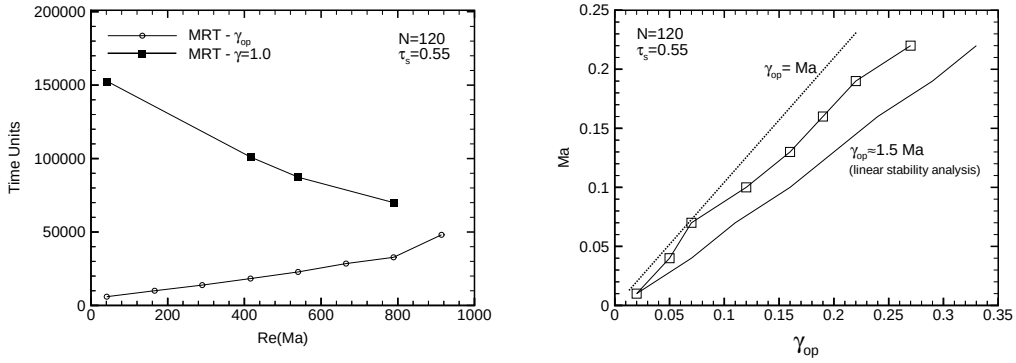

Figure 5.10: (Left) Time units needed to reach machine accuracy versus Reynolds number, computed as a function of Mach number; (Right) optimal value of the preconditioning parameter, γ_{op}, as a function of Mach number.

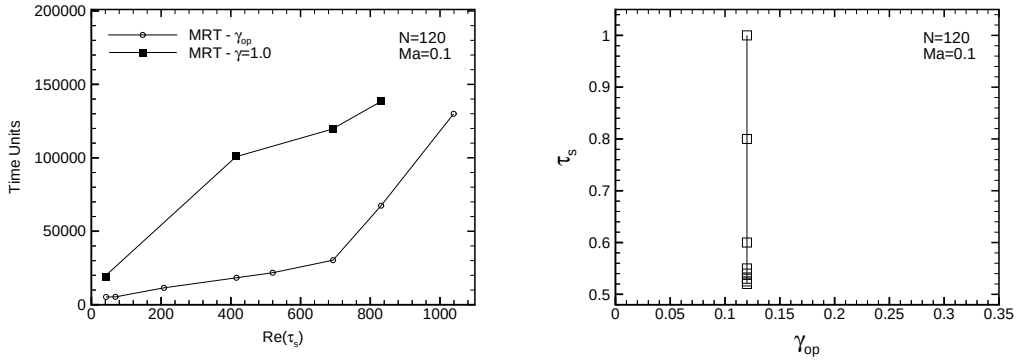

Figure 5.11: Time units needed to reach the machine accuracy versus Reynolds number, computed as a function of relaxation factor $s_\nu = 1/\tau_s$ (left); optimal value of the preconditioning parameter, γ_{op}, as a function of relaxation factor (right).

5.3.3 Under-relaxation effect on preconditioner performance

The DBE Eq. (1.1) can be discretized as (see for example [94]):

$$f_\alpha(x_i + e_{i\alpha}\delta t, t + \delta t) - f_\alpha(x_i + e_{i\alpha}\delta t, t) + \frac{e_{i\alpha}\delta t}{\delta x} f_\alpha(x_i + e_{i\alpha}\delta t, t) - f_\alpha(x_i, t) = \Omega_\alpha(x_i, t)\,; \tag{5.5}$$

where, when $(e_{i\alpha}\delta t)/\delta x = 1$, then $CFL = 1$. In the classical LB method, the discrete temporal and spatial steps are the unity ($\delta t = 1$ and $\delta x = 1$), and they determine the lattice units. Therefore, the second and the third terms are canceled and this makes it possible to split the simulation in the collision and the propagation steps.

Starting from Eq. (5.5), the viability of a direct time-marching preconditioning of the lattice Boltzmann equation is studied, as an alternative to find lattice Boltzmann equations which lead to preconditioned Navier-Stokes systems. To modify this scheme, the temporal term of each equation is multiplied by a diagonal matrix $\Phi_{\alpha\beta} = diag(\phi, ..., \phi)$, with ϕ a constant factor equal for all f_α, which is expected to modify the convergence behavior without introducing any modification to the steady state solution. The following modified discretization results:

$$\begin{aligned} \Phi_{\alpha\beta}[f_\alpha(x_i + e_{i\alpha}\delta t, t + \delta t) &- f_\alpha(x_i + e_{i\alpha}\delta t, t)] \\ &+ \frac{e_{i\alpha}\delta t}{\delta x} f_\alpha(x_i + e_{i\alpha}\delta t, t) - f_\alpha(x_i, t) \\ &= -\delta t M_\alpha^{-1} S_\alpha [m_\alpha(x_i, t) - m_\alpha^{eq}(x_i, t)]\,. \end{aligned} \tag{5.6}$$

Simple algebra with this equation leads to the following collision-propagation algo-

rithm:

$$\begin{aligned} \text{collision: } \tilde{f}_\alpha(x_i,t) &= [\Phi_{\alpha\beta} f_\alpha(x_i,t) + (I_{\alpha\beta} - \Phi_{\alpha\beta}) f_\alpha(x_i, t-\delta t)]\, f^*_\alpha(x_i,t) \\ &- M_\alpha^{-1} S_\alpha [m_\alpha(x_i,t) - m^{eq}_\alpha(x_i,t)]\,, \end{aligned} \tag{5.7a}$$

$$\text{propagation: } f_\alpha(x_i + e_{i\alpha}\delta t, t+\delta t) = \tilde{f}_\alpha(x_i,t)\,; \tag{5.7b}$$

where $f^*_\alpha(x_i,t) = \Phi_{\alpha\beta} f_\alpha(x_i, t-\delta t) + (I_{\alpha\beta} - \Phi_{\alpha\beta}) f_\alpha(x_i, t-2\delta t)$. This scheme can be viewed as a standard collision-propagation algorithm plus a temporal under-relaxation of f_α variables. It is actually a Jacobi iteration. The scheme can be improved by using other classic iterators, as the Gauss-Seidel one, but losing locality in the collision step.

An under-relaxation coefficient $\phi = 0.8$ is selected, and results for preconditioned versions of the SRT and MRT collision operators are shown in Fig. 5.12. In the SRT case, when moving from the optimal preconditioning ($\gamma = 0.18$) to an under-relaxed preconditioning with the same γ, it is possible to reach lower residual values. The under-relaxation modifies the stability behavior and, therefore it is possible to select smaller values of γ. Thus, using the new optimal value of the preconditioning parameter ($\gamma = 0.11$), less time is needed to reach machine accuracy. In the case of MRT (right plot in Fig. 5.12), these improvements are not so obvious, and under-relaxation can even worsen convergence if the value of γ is maintained. However, a new $\gamma_{op} = 0.10$ is found, which slightly improves the convergence behavior. A drawback of the relaxation modification is that it slightly decreases (by a 15%) the computational efficiency of the scheme, because of the increase in the number of operations needed. MLUPS figures for the under-relaxed scheme have been plotted in Fig. 5.6 alongside those for the previous schemes.

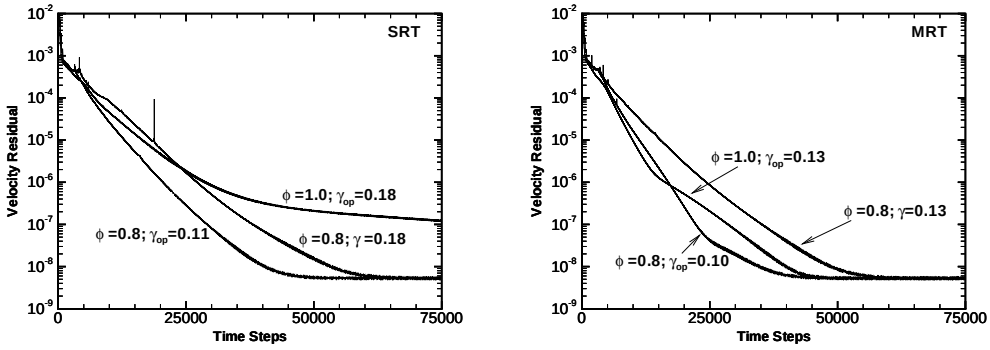

Figure 5.12: Effect of under-relaxation for SRT (left) and MRT collision operators (right).

5.4 Two dimensional test case II: ill-conditioned stokes flow in a slip channel

Incompressible Stokes flows are characterized by very low Reynolds and Mach numbers. A very low Re number implies a high τ_s, which degrades the solution by introducing errors in the non-equilibrium term. This error influences the computation of stresses or forces at walls, and also of the value of the slip velocity at walls [53, 60]. From these accuracy difficulties, the limiting value for the relaxation factor is about $\tau_s = 2$.

As stated above, the value of γ changes the relaxation factor τ_s, redefining the flow viscosity to a τ_p value, which dictates the numerical behavior. This can be used to reduce the error in very-low-Reynolds-number flows by selecting a value for γ which results in $\tau_p < \tau_s$. The results provided in Fig. 5.4 indicate that this range of values for γ are stable but do not accelerate the flow, because the resulting LB method is ill-conditioned, as explained in Sec. 5.2.3.

With the present test case, the effects on performance of the ill-conditioned scheme are studied. Additionally, the modifications in body force terms and in flow-dependent boundary-conditions to be applied with the preconditioning LB method are detailed.

5.4.1 Stability analysis

The application of the modified equilibrium moments alters the stability limits of the method, which have a dependence on the value of the free parameter γ. A linear stability analysis as in Sec. 5.2 is performed to provide guidelines about the new limits. The results presented here correspond to the $Ma \to 0$ plane for the $0 < 1/\gamma < 1$ range in Fig. 5.4.

The study shows that the stability is independent of the Mach number within the incompressible limit ($Ma < 0.3$). On the other hand, the combined influences of γ and the relaxation factor τ_s are shown in Fig. 5.13. In this Figure dashed lines represent λ_{max} isocontours (computed numerically); solid isocontours represent the modified relaxation parameter given by the relation between τ_s and τ_p; and solid circles are the $\gamma - \tau_s$ values used in actual numerical simulations, see below, which follow the iso-contour of $1/s_\nu = \tau_p = 0.505$. The most important conclusion is that the method proposed fulfills the stability criteria of known LB methods but applying the effective relaxation factor τ_p.

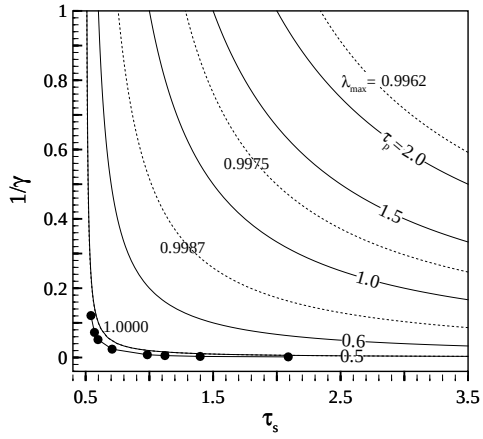

Figure 5.13: Stability map for the ill-conditioned lattice Boltzmann method ($0 < 1/\gamma < 1$) for the $Ma \to 0$ limit.

5.4.2 Application of the ill-conditioned scheme

Simulations of the Stokes flow in a two-dimensional channel with slip boundary conditions have been performed to test the method. To compare the results, an analytical solution has been obtained from the Navier-Stokes equation with the following slip boundary condition:

$$u_w = K\frac{H}{\mu}\tau_w \; ; \tag{5.8}$$

where H is the height of the channel; $\mu = \rho_0\nu$ is the dynamic viscosity; τ_w is the stress at the walls (at $y = 0$ and $y = H$); and K is a parameter defined as $K = Ma/Re$. By using K a relation is prescribed between the slip at the wall and the relaxation factor τ_s. As a result, higher τ_s values result in longer slip lengths.

The solution for the streamwise velocity is:

$$u_x(y) = u_x^{max}\frac{4}{H^2(1+4K)}\left(H^2K + H - y^2\right) \; ; \tag{5.9}$$

with

$$u_x^{max} = -\frac{H^2}{8}\frac{1}{\mu}\frac{dp}{dx}(1+4K) \; . \tag{5.10}$$

The shear stress τ_{yx} has the following expression:

$$\tau_{yx} = u_x^{max}\frac{4\mu}{H^2(1+4K)}\left(H - 2y\right) \; ; \tag{5.11}$$

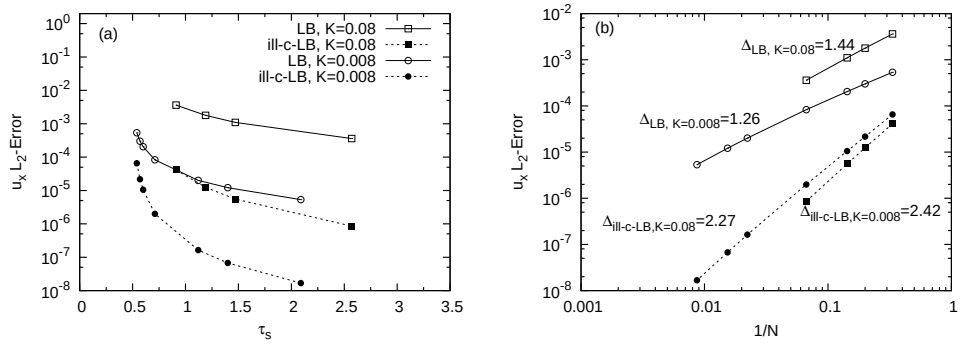

Figure 5.14: (a) Evolution of the streamwise velocity error for two given K, as a function of the inverse of the relaxation factor, for LB and for ill-c-LB. (b) The same error versus the inverse of the resolution, N.

and, therefore, the shear stress at the wall is:

$$\tau_w = \pm u_x^{max} \frac{4\mu}{H(1+4K)} \,. \tag{5.12}$$

The flow in the channel is driven by a body force introduced by a forcing term in Eq. (1.2), with $a_i = (dp/dx, 0)$. Periodic boundary conditions are imposed in the streamwise direction, with density being renormalized with the density at the central point in the inlet, $x = (0, H/2)$.

The approach by Bouzidi et al. [38] is used to impose the slip boundary condition:

$$f_{\overline{\alpha}}(x_i, t) = f_\alpha(x_i, t) + 6w_\alpha(e_{i\alpha}u_{wi}) \,, \tag{5.13}$$

where $e_{i\overline{\alpha}} = -e_{i\alpha}$; and $\mathbf{u}_w = (u_w, 0)$, with u_w being computed with Eqs. (5.8) and (5.12), which implicitly include the influence of γ through ν. This boundary condition allows to fix the exact analytical solution at the boundary and, hence, makes it possible to study the effect on the solution of the method proposed without the influence of the boundary conditions.

Several Stokes flow simulations have been performed with both the standard lattice Boltzmann MRT (LB) and the ill-conditioned lattice Boltzmann method (ill-c-LB). The relaxation factors are selected as follows: $s_\nu = 1/\tau_s$ is chosen to have a fixed value to yield the desired viscosity; $s_e = s_\epsilon = s_\nu$ to properly recover the incompressible limit solution [104]; and $s_q = 8(2 - s_\nu)/(8 - s_\nu)$ to take into account the exact location of the wall between two nodes [30, 31].

The increased accuracy for a given resolution can be seen in Fig. 5.14. Figure 5.14 (a) shows the evolution of the streamwise velocity error for two different values of K as a function of the inverse of the relaxation factor, for both LB and ill-c-LB. Each

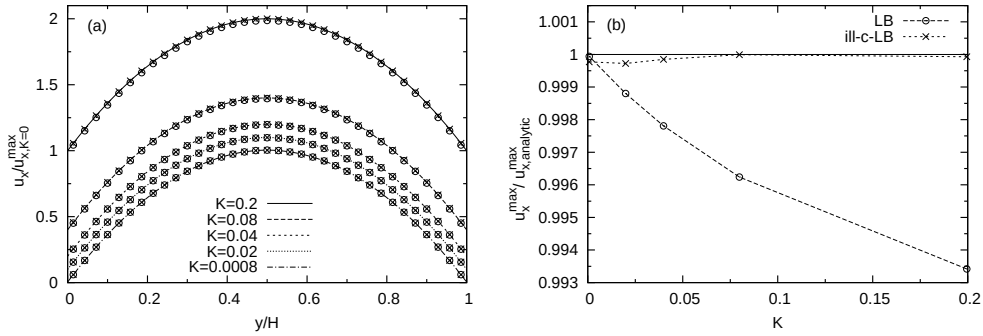

Figure 5.15: (a) Velocity profiles obtained with the LB and with the ill-c-LB for different K values with $N = 35$ and $Re = 1$. (b) Deviation from the exact solution of u_x^{max}.

point has associated an increasing resolution which is related to K and s_ν: $N = 3, 5, 7, 15, 45, 65, 115$ for $K = 0.00798$; and $N = 3, 5, 7, 15$ for $K = 0.07979$. The values of γ used are those to obtain $\tau_p = 0.505$ and $Ma = 0.09798$. In Fig. 5.14 (b) The same error is plotted against the inverse of the resolution. The slopes (Δ) of the curves are also indicated in the Figure for LB and for ill-c-LB.

The ill-c-LB method moves the diffusive order from first to second, albeit the improvement in accuracy involves an implicit increment in the computer time due to the worsened convergence behavior. This is because the non-linear velocity terms (the convective terms), have a decreasing effective importance as $1/\gamma$ becomes smaller. A compromise between accuracy and computational time can be obtained by a proper selection of γ.

When simulations with increasing τ_s values are performed, Fig. 5.15, the solution deteriorates as τ_s increases. This degradation can be avoided by using the proposed ill-c-LB method as shown in Fig.5.15 (b), where the deviation from the exact solution of u_x^{max} Eq. (5.10) is plotted as a function of K for both LB and ill-c-LB. The points are from simulations with $N = 35$, $Re = 1$, and increasing values of $\tau_s = 0.548, 0.709, 2.918, 5.337, 12.592$. The values of γ are selected to obtain $\tau_p = 0.505$.

5.5 Two dimensional test case II: micro-channel

The simulation of the flow of gases in channels or tubes within the micro-scale is relevant in the design of MEMS. These flows are characterized by non-negligible Knudsen numbers ($Kn > 0.001$) and very low Reynolds and Mach numbers. Although Ma is very small, the compressibility effects are important and, thus, the lattice Boltzmann method requires some modifications [105] for the simulation of microdevices [106, 107].

Most of these micro-flow configurations lead to steady state flows; therefore preconditioning, as presented in this work, can be applied. The ill-conditioned method is not attractive due to the lack of good convergence rates.

The flow of a gas in a channel is simulated within the slip regime ($0.1 > Kn > 0.001$). The length of the microchannel is $L = 1000\delta x$ and its height is $H = 20\delta x$. The Reynolds number is set to $Re = 1$ and the Knudsen number varies from $Kn = 0.01$ to $Kn = 0.15$. This last value is slightly off the slip regime but it is used only to validate the preconditioner effect on the flow. The Mach number is defined by the relation $Ma = KnRe(\pi/2)^{-1/2}$ [108]. The boundary conditions applied are: for inlet and outlet, a prescribed pressure is set in order to recover the desired Kn at the outlet; and at the walls, the boundary condition by Sbragaglia and Succi [73] is adapted to incorporate the preconditioning effect. This boundary condition is a linear combination of the specular reflection f_α^s and the bounce-back f_α^{bc} and it can be expressed as:

$$\tilde{f}_\alpha = s f_\alpha^s + (1-s) f_\alpha^{bc} \,, \tag{5.14}$$

where s is computed from the analytical solution of the flow in a microchannel:

$$s = \frac{1}{1 + \frac{3\nu}{HKn}} \,, \tag{5.15}$$

with $\nu = \gamma/3(\tau_s - 0.5)$. This formulation of the boundary condition allows to recover the corresponding slip at the wall as a function of the Knudsen number $O(Kn)$, while preserving the correct effect of γ. The lattice Boltzmann method applied is a $D2Q9$ MRT with and without preconditioning and with the following relaxation factors: $s_e = s_\epsilon = s_\nu = 1/\tau_p$ and $s_q = 8(2 - s_\nu)/(8 - s_\nu)$.

Isothermal gas microflows exhibit rarefaction and compressibility effects [21]. These are modeled through the slip boundary condition and a density dependence of the relaxation factor (and, therefore, of the viscosity):

$$\tau_p = \frac{1}{2} + \frac{\tau_s - 1/2}{\rho\gamma} \,. \tag{5.16}$$

The analytical solution of the viscous flow in a channel with the above conditions leads to the following expression for the x-component of the velocity [108]:

$$\frac{u(X,Y)}{u_o} = \frac{dp/dX}{dp_o/dX} \frac{Y - Y^2 + Kn}{1/4 + Kn_o} \,; \tag{5.17}$$

where $X = x/L$ and $Y = y/H$ are the normalized coordinates, and subscript o refers to the outlet. The pressure profile along the channel is given by:

$$p(X)/p_o = -6Kn_o + \sqrt{(-6Kn_o)^2 + (1 + 12Kn_o)X + (P^2 + 12Kn_oP)(1 - X)} \,, \tag{5.18}$$

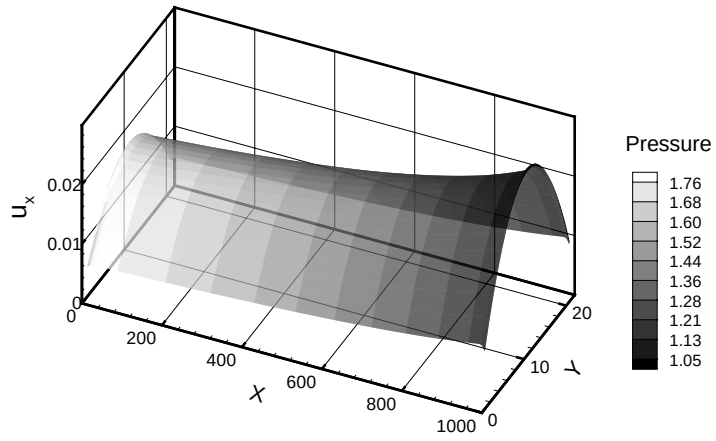

Figure 5.16: Velocity profiles for the whole microchannel with superimposed pressure iso-contours.

where $P = p_i/p_o$ is the ratio between the inlet and outlet pressures. These analytical expressions are used to validate the effect of the preconditioner.

The velocity profile along the x direction from the lattice Boltzmann simulation is shown in Fig. 5.16 to illustrate the non-linear behavior of the gas flow in a microchannel. As the gas moves downstream the pressure drop increases, and so does the Knudsen number; therefore, the slip becomes larger and the mass flow increases.

In Fig. 5.17 the normalized velocity profiles at outlet are plotted for different Knudsen numbers, as well as the normalized pressure profiles along the channel. Results from the non-preconditioned lattice Boltzmann method differs slightly from those obtained from the preconditioned one. However, as it can be seen in Fig. 5.18 (left) the accuracy is always better with the preconditioned lattice Boltzmann approach.

Due to the compressibility effects described above a variable viscosity is used, which serves also the purpose of validating the method for these situations. The optimal values of γ are for this reason very different from those derived from the linear stability analysis, Fig. 5.18 (right). The optimal γ value is conditioned by the maximum τ_s in the domain, and for large values of τ_s, γ_{op} increases as predicted by the linear stability analysis, Fig. 5.3. In this Fig. 5.3, for values $\tau_s > 0.8$ the region with lower λ_{max} is no longer close to the stability limit.

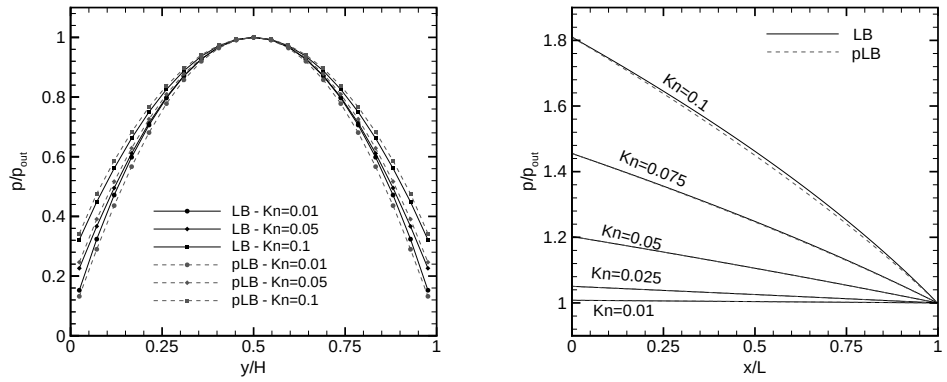

Figure 5.17: Velocity (left) and pressure (right) profiles obtained for the microchannel.

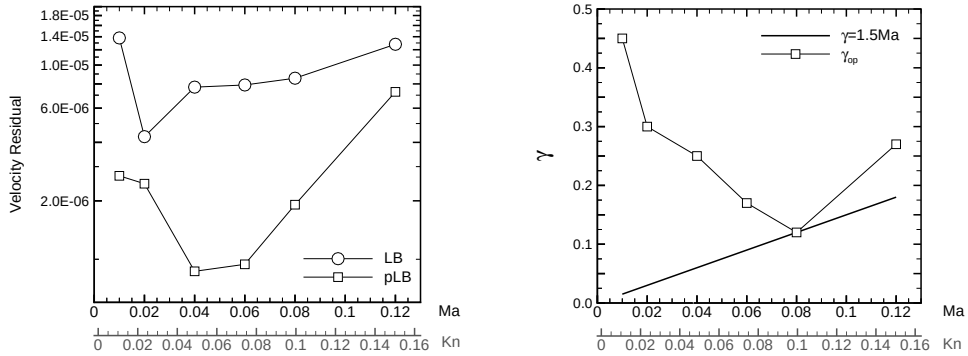

Figure 5.18: Accuracy with (pLB) and without (LB) preconditioning for the microchannel (left); and optimal values for γ (right).

5.6 Three-dimensional test case: backward-facing step

The previous results and analysis for the $D2Q9$ model can be extended for other lattice geometries. Here, the application to the $D3Q19$ model is presented. The description of the model can be found in Appendix B, and in this section some salient results are briefly described.

The backward-facing step is the selected test case. At wall boundaries, the halfway bounce-back condition is used; at the inlet a constant velocity (u_0) is set using UBB; and at the outlet a convective condition for f_α is applied [40] (see Chapter 2 and 3 for boundary-condition definition and behavior). Based on results of Armaly

et al. [109] a Reynolds number equal to 100 has been chosen; therefore, the flow remains laminar. The geometry, streamlines and recirculation length for the test case are plotted in Fig. 5.19; and in Fig. 5.20 a comparison between numerical and experimental results is shown. The reattachment length is $x_r/L = 3.2$, which agrees well with the experimental value of Armaly et al. [109] $x_r/L = 3.1$.

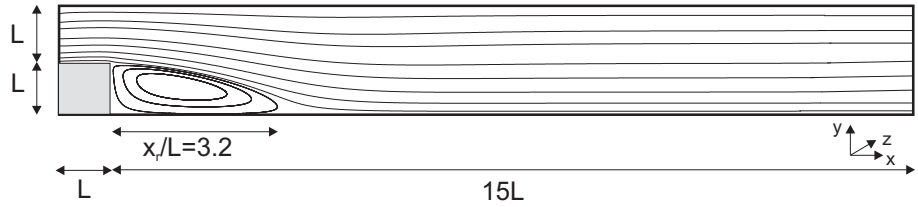

Figure 5.19: Backward-facing step: domain dimensions and streamlines for $Re = 100$.

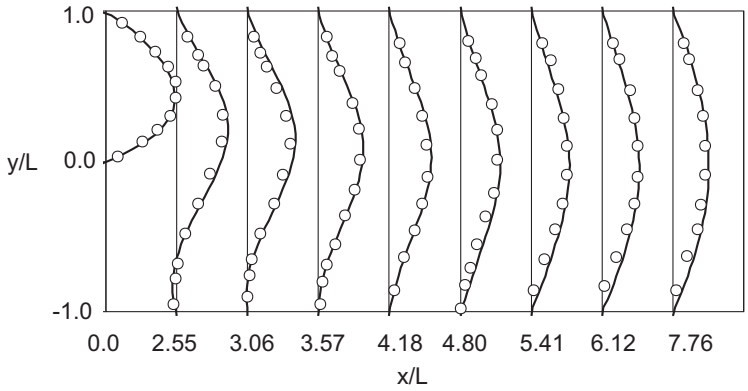

Figure 5.20: Velocity profiles at different dimensionless lengths x/L (black lines); and experimental results for Re=100 from Armaly et al. [109] (white dots).

As in the two-dimensional test-case, the residual evolutions are plotted, Fig. 5.21, to evaluate the improvement in the convergence performance. As for the $D2Q9$ model, preconditioning makes it possible to reduce the time needed to attain a target accuracy. For the $D3Q19$ lattice the optimal value for the preconditioner parameter is found numerically to be $\gamma_{op} = 2Ma$.

5.7 Conclusions

The stabilization of the solution of the lattice Boltzmann equation is an early [23] but a nowadays very active research topic [110, 111, 112] and it seems to be paramount for

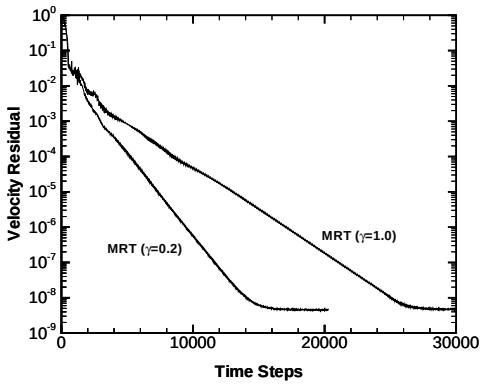

Figure 5.21: Evolution of velocity residual for two MRT simulations of the backward-facing step: preconditioned ($\gamma_{op} = 0.2$) and non-preconditioned ($\gamma = 1$).

the penetration of LBM as a competitive CFD technique. Additionally, acceleration is necessary for the efficient explicit computation of steady states. The optimal preconditioned lattice Boltzmann equation allows to achieve these two desired properties with an additional improvement in accuracy. In summary, the following conclusions can be derived from the work done.

Optimal equilibrium-based preconditioners for lattice Boltzmann methods defined with the aid of Chapman-Enskog expansion, linear stability analysis, and the condition number of the equivalent Navier-Stokes equations, are proved to be a simple and efficient technique to accelerate steady state computations. The main advantage is that, by switching to an MRT collision operator and adding a minor modification to the standard LB algorithm, it is possible to reduce about one order of magnitude the computational time for steady state simulations. This time reduction varies with the flow parameters, and could be even greater. Additionally, better accuracy and stability are obtained. The local definition of the free parameter would improve the preconditioner behavior; however this is not trivial in the standard scheme due to the spatio-temporal constrains which relate all the information within the domain.

The optimal values for γ depend on the characteristics of the flow configuration but lie in the range $\gamma_{op} = (1.0Ma, 1.5Ma)$, as obtained from linear stability analysis and simulations for the $D2Q9$ LB method. From simulations $\gamma_{op} = 2.0Ma$ is obtained for the $D3Q19$ method. For very low Reynolds numbers ($\tau_s > 2$), γ_{op} increases from this values.

Direct preconditioning of the lattice Boltzmann equation can be also applied, but the attempt made in this direction indicates it is less effective than Navier-Stokes based preconditioning. A direct time-derivative lattice Boltzmann preconditioner can be viewed as an under-relaxation which introduces no improvement in the behavior

of preconditioned schemes proposed in this work. Results obtained point to the possibility of successfully replacing under-relaxation by the γ-preconditioner as a smoother in spatial multigrid solvers for the LB method [94].

The preconditioned lattice Boltzmann method has been shown to work well in flows with non-constant viscosity, e.g. in microflows; this may open the door to their application to other kinds of flows, such as turbulent ones, where subgrid scale processes are introduced through a modified viscosity.

The use of the preconditioning scheme to obtain an ill-conditioned system can help to improve the accuracy of the method for very low Reynolds numbers but the significant increase in the time needed to reach the steady state may turn the method impractical, at least for low velocities.

6

Conclusions

This Thesis has presented new treatments and results for two numerical issues, i.e. boundary conditions and preconditioning, in the solution of the lattice Boltzmann equation. Specific conclusions for each topic are at the end of each chapter.

The first part (Chapters 2 and 3) addressed the specification of **boundary conditions** other than the widely-studied Dirichlet-velocity condition. Specifically, classic topics in boundary conditions for fluid flow simulations solving the Navier-Stokes equations are revisited for lattice Boltzmann methods:

- The domain-boundary interaction in pseudo-compressible or compressible solvers, and its role in the specification of non-reflecting boundaries and in the definition of a far-field pressure at outlets.
- The setting of boundary conditions involving spatial derivatives of the macroscopic conserved variables.

The most relevant conclusions and novel contributions for this first part are:

- The well-posed open boundary conditions for hydrodynamic simulations (and their implementation in lattice Boltzmann methods) are reflective in nature: the pressure wave reflections deteriorate the convergence behavior towards a steady or periodic solution, and they can have a relevant influence on the solution.
- A new density-filtering non-reflective boundary condition is presented for Dirichlet-velocity conditions in steady open boundaries. It is used to determine the influence of pressure-wave reflections on the solution.

- A new characteristic non-reflective boundary condition is presented for athermal LB methods. It can reduce the fluid-boundary interaction up to the 99% and does not need additional absorbing layers or extended domains. It can be applied to Dirichlet, Neumann and Robin boundary conditions of macroscopic-conserved variables in steady and unsteady open boundaries and walls.

- A novel flexible structure to account for macroscopic-gradient boundary conditions in complex geometries is proposed. The implementation of this boundary condition is presented in the framework of a recent comprehensive work by Ginzburg et al. [31] about link-wise boundary conditions. Its application allows the reproduction of a great amount of complex phenomena involving pressure of velocity gradients (e.g. hydrophobic-hydrophilic wall treatments, surfactant effects in gas-liquid interfaces, subgrid description of vents and fans, or wall models for turbulent flows).

In the second part of the Thesis (Chapters 4 and 5) a class of modified lattice Boltzmann methods, derived to reproduce time-derivative **preconditioning** of the Navier-Stokes equations, are studied. The main conclusions are:

- The complete process to the study of other new preconditioned schemes for lattice Boltzmann should be based on: (i) a Chapman-Enskog procedure to properly recover some preconditioned-like Navier-Stokes system; (ii) a study of the condition number to assess the potential of the method; and (iii) a linear analysis to establish stability limits.

- The main advantage of preconditioned lattice Boltzmann methods is that, by switching to an MRT collision operator and adding a minor modification to the standard LB algorithm, it is possible to reduce about one order of magnitude the computational time for steady state simulations, and, additionally, to improve the accuracy and the stability of the method.

- Two preconditioners for LB have been presented: β- and γ-preconditioner. Specifically, the β-preconditioner is a new LB preconditioner based on the modification of the linear-velocity terms u of the equilibrium distribution function, and it is proved to improve γ-preconditioned results at very low Mach numbers ($Ma < 0.05$).

Future work

The work presented opens new interesting possibilities for future research in lattice Boltzmann methods. Some possible future work is discussed in the following.

Regarding the first part, the Euler-characteristic approach for open boundary conditions can be improved in several ways following the development of this boundary treatment in classical CFD techniques (e.g. [113]). Possible improvements from the lattice Boltzmann method perspective may include: the projection of the Euler characteristics onto the equilibrium moments to express this boundary condition in the LB variables f_α (e.g. as a correction term for UBB or PAB); the extension, following [31], of the CBC to higher order and to arbitrary geometries; and the application of advanced LB methods [114] to introduce the energy-acoustic effects in a consistent way.

Future work regarding preconditioning for LB methods should focus on its extension to the solution of non-isothermal flows and of transient flows. Extensions for unsteady flows would be possible with a dual-time stepping. The design of new preconditioning methods is another interesting research direction; this could be effected through a bidirectional search of equivalent lattice Boltzmann preconditioners of well-known Navier-Stokes ones. A global mapping between NS preconditioning schemes and modified equilibrium distribution functions would be useful to determine possible new directions in this field and possible improvements of NS methods through the Boltzmann equation analysis. This mapping would be necessary for the formulation of hybrid NS-LB schemes for multiscale and/or multiphysics problems, where time-derivative NS preconditioning needs to be applied. The study of boundary-condition effects in preconditioning schemes, only briefly mentioned in this Thesis, could be addressed with the aid of the asymptotic analysis of the lattice Boltzmann equation [16, 31].

Appendices

A – Nomenclature

This Appendix collects the main nomenclature terms used in this Thesis. The meaning of each symbol is detailed in the text where the symbol is applied.

Acronyms

BGK	Bhatnagar-Gross-Krook collision operator (also called SRT in this Thesis)
CBC	Characteristic Boundary Condition
CFD	Computational Fluid Dynamics
CFL	Courant-Friedrichs-Levi number
CN	Condition Number
DBE	Discrete Boltzmann Equation
DPD	Dissipative Particle Dynamics
LB	Lattice Boltzmann
LBM	Lattice Boltzmann Methods
LODI	Local One-Dimensional Inviscid
MR	Multi-Reflection (boundary condition)
MRT	Multiple-Relaxation-Time collision operator
NS	Navier Stokes
PAB	Pressure Anti-Bounce-back
PLI	Pressure Linear Interpolation
PMR	Pressure Multi-Reflection
SPH	Smoothed-Particle Hydrodynamics
SRD	Stochastic Rotation Dynamics
SRT	Single-Relaxation-Time collision operator
UBB	Velocity Bounce-Back
ULI/DLI	Upwind/Downwind Linear Interpolation

Abbreviations

e.g.	*exempli gratia*
Eq.	Equation
Fig.	Figure
i.e.	*id est*

Latin alphabet

c_s	speed of sound
e	macroscopic moment related to energy
$e_{i\alpha}$	microscopic velocities
f	microscopic-velocity distribution function
f_α	discretized microscopic-velocity distribution function
$\tilde{f}_\alpha$	post-collision distribution function
g_α	modified microscopic-velocity distribution function
h	length
i	imaginary unit
j_i	momentum (ρu_i)
k	relaxation parameter in linear relaxation models for wave amplitudes
m_α	macroscopic moments
n	normal direction
p	pressure
p_{ij}	macroscopic moment related to the stress tensor
q_i	macroscopic moment related to the energy flux
r	reflection ratio
s	specular reflection factor
$s_{e,\epsilon,q}$	relaxation times related to e, ϵ and q_i
s_ν	relaxation time related to viscosity ($s_\nu = 1/\tau_s$)
t	time
u_i	velocity $u_i = (u, v, w)$
u_0	reference velocity
w_α	weight factors
$\mathrm{w}_{1,2,3}$	coefficients to define boundary conditions
x_i	spatial coordinates

A	amplitude
$A_{\alpha\beta}$	advection operator
C_d	drag coefficient
C_l	lift coefficient
D	diameter
$DdQq$	d dimensions and q discrete velocities (for lattice classification, e.g. D2Q9 or D3Q19)
E	energy
$\mathbf{E}, \mathbf{F}$	vectors of convective- and pressure-term variables in the NS equations in vector form
$\mathbf{E}_v, \mathbf{F}_v$	viscous terms in NS equations in vector form
F_α	body force
$F_\alpha^{p.c.(u,p)}$	boundary-condition error-correction for (velocity, pressure)
F_d	drag force
$G_{\alpha\beta}$	variation of moments due to collision
K	constant free parameter
Kn	Knudsen number
L	length
L_i	characteristic wave amplitude $L_i = (L_1, L_2, L_3, L_4)$
$L_{\alpha\beta}$	linearized evolution operator
$M_{\alpha\beta}$	transformation matrix between f_α and m_α
Ma	Mach number
N	number of nodes (in a characteristich length)
$\mathbf{P}$	preconditioned matrix
P	ratio between the inlet and outlet pressures
$\mathbf{Q}$	matrix of left eigenvectors of $\mathbf{\Gamma}$
R	ideal gas constant
$R_\alpha^{u,p}$	interpolation boundary-condition scheme for (velocity, pressure)
Re	Reynolds number
$S_{\alpha\beta}$	diagonal relaxation matrix
St	Strouhal number
T	temperature; normalized t-coordinate
T_c	time period
$W_\alpha^{u,p}$	Dirichlet condition for (velocity, pressure)
X	normalized x-coordinate
Y	normalized y-coordinate

Greek alphabet

α	preconditioned parameter related to ρ
β	preconditioned parameter related to u
γ	preconditioned parameter related to u^2
δq	link-distance between the last fluid node and the boundary
$\delta\rho$	density variation
δt	time step in the lattice
δx	space between lattice nodes
ϵ	macroscopic moment related to energy square; small parameter (Appendix C)
ζ	bulk viscosity
κ	specific-heat ratio
λ	second coefficient of viscosity; eigenvalue
μ	dinamic viscosity
ν	kinematic viscosity
ρ	density
ρ_0	reference density
τ_{ij}	shear stress
τ_p	relaxation time in the preconditioned SRT LB method
τ_s	relaxation time in the SRT collision operator ($\tau_s = 1/s_\nu$)
ϕ	under-relaxation parameter; arbitrary variable
ω	frequency
Γ	damping coefficient
$\mathbf{\Gamma}$	matrix of convective- and pressure-term variables in the NS equations in vector form
$\mathbf{\Lambda}$	diagonal matrix of the eigenvalues of $\mathbf{\Gamma}$
Π	relative to the symmetric part of the distribution function; momentum flux
Ω_α	collision operator

Superscript

eq	equilibrium
neq	non-equilibrium
$+$	symmetric
$-$	antisymmetric

Subscript

b	boundary
c	conserved
e	extrapolated
f	fluid
i, j, k	spatial coordinate indices
in	inlet
max	maximum
min	minimum
n	normal
out	outlet
tot	total
v	viscous
w	wall
N	Neumann
R	Robin
α, β, γ, δ	microscopic-velocity-space indices
$\bar{\alpha}$	velocity index opposite to α

B – D3Q19 MRT lattice Boltzmann method

The $D3Q19$ lattice Boltzmann method used in this work is the one defined by Tölke et al. [115]. The model uses the following velocity vector (see Fig. 1):

$$e_{i\alpha}^{D3Q19} = \begin{pmatrix} 0 & 1 & -1 & 0 & 0 & 0 & 0 & 1 & -1 & 1 & -1 & 1 & -1 & 1 & -1 & 0 & 0 & 0 & 0 \\ 0 & 0 & 0 & 1 & -1 & 0 & 0 & 1 & -1 & -1 & 1 & 0 & 0 & 0 & 0 & 1 & -1 & 1 & -1 \\ 0 & 0 & 0 & 0 & 0 & 1 & -1 & 0 & 0 & 0 & 0 & 1 & -1 & -1 & 1 & 1 & -1 & -1 & 1 \end{pmatrix} ; \tag{B.1}$$

and the moments are defined as:

$$m_\alpha = (\rho, e, \epsilon, j_x, q_x, j_y, q_y, j_z, q_z, 3p_{xx}, 3\pi_{xx}, p_{ww}, \pi_{ww}, p_{xy}, p_{yz}, p_{xz}, m_x, m_y, m_z)^T . \tag{B.2}$$

The relaxation matrix is:

$$S_{\alpha\beta} = diag(0, s_e, s_\epsilon, 0, s_q, 0, s_q, 0, s_q, s_\nu, s_\pi, s_\nu, s_\pi, s_\nu, s_\nu, s_\nu, s_m, s_m, s_m) ; \tag{B.3}$$

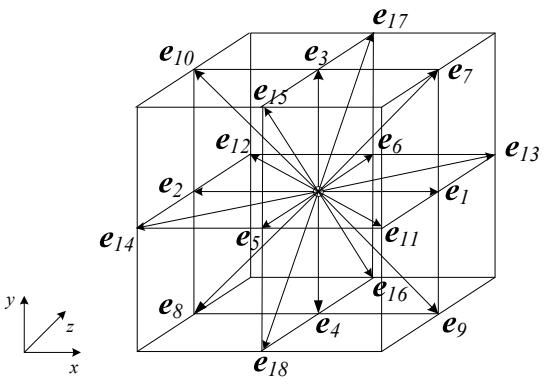

Figure 1: D3Q19 lattice used for three-dimensional simulations.

and the transformation matrix is:

$$M_{\alpha\beta} = \begin{pmatrix}
1 & 1 & 1 & 1 & 1 & 1 & 1 & 1 & 1 & 1 & 1 & 1 & 1 & 1 & 1 & 1 & 1 & 1 & 1 \\
-1 & 0 & 0 & 0 & 0 & 0 & 0 & 1 & 1 & 1 & 1 & 1 & 1 & 1 & 1 & 1 & 1 & 1 & 1 \\
1 & -2 & -2 & -2 & -2 & -2 & -2 & 1 & 1 & 1 & 1 & 1 & 1 & 1 & 1 & 1 & 1 & 1 & 1 \\
0 & 1 & -1 & 0 & 0 & 0 & 0 & 1 & -1 & 1 & -1 & 1 & -1 & 1 & -1 & 0 & 0 & 0 & 0 \\
0 & -2 & 2 & 0 & 0 & 0 & 0 & 1 & -1 & 1 & -1 & 1 & -1 & 1 & -1 & 0 & 0 & 0 & 0 \\
0 & 0 & 0 & 1 & -1 & 0 & 0 & 1 & -1 & -1 & 1 & 0 & 0 & 0 & 0 & 1 & -1 & 1 & -1 \\
0 & 0 & 0 & -2 & 2 & 0 & 0 & 1 & -1 & -1 & 1 & 0 & 0 & 0 & 0 & 1 & -1 & 1 & -1 \\
0 & 0 & 0 & 0 & 0 & 1 & -1 & 0 & 0 & 0 & 0 & 1 & -1 & -1 & 1 & 1 & -1 & -1 & 1 \\
0 & 0 & 0 & 0 & 0 & -2 & 2 & 0 & 0 & 0 & 0 & 1 & -1 & -1 & 1 & 1 & -1 & -1 & 1 \\
0 & 2 & 2 & -1 & -1 & -1 & -1 & 1 & 1 & 1 & 1 & 1 & 1 & 1 & 1 & -2 & -2 & -2 & -2 \\
0 & -2 & -2 & 1 & 1 & 1 & 1 & 1 & 1 & 1 & 1 & 1 & 1 & 1 & 1 & -2 & -2 & -2 & -2 \\
0 & 0 & 0 & 1 & 1 & -1 & -1 & 1 & 1 & 1 & 1 & -1 & -1 & -1 & -1 & 0 & 0 & 0 & 0 \\
0 & 0 & 0 & -1 & -1 & 1 & 1 & 1 & 1 & 1 & 1 & -1 & -1 & -1 & -1 & 0 & 0 & 0 & 0 \\
0 & 0 & 0 & 0 & 0 & 0 & 0 & 0 & 1 & 1 & -1 & -1 & 0 & 0 & 0 & 0 & 0 & 0 & 0 \\
0 & 0 & 0 & 0 & 0 & 0 & 0 & 0 & 0 & 0 & 0 & 0 & 0 & 0 & 0 & 1 & 1 & -1 & -1 \\
0 & 0 & 0 & 0 & 0 & 0 & 0 & 0 & 0 & 0 & 0 & 1 & 1 & -1 & -1 & 0 & 0 & 0 & 0 \\
0 & 0 & 0 & 0 & 0 & 0 & 0 & 1 & -1 & 1 & -1 & -1 & 1 & -1 & 1 & 0 & 0 & 0 & 0 \\
0 & 0 & 0 & 0 & 0 & 0 & 0 & -1 & 1 & 1 & -1 & 0 & 0 & 0 & 0 & 1 & -1 & 1 & -1 \\
0 & 0 & 0 & 0 & 0 & 0 & 0 & 0 & 0 & 0 & 0 & 1 & -1 & -1 & 1 & -1 & 1 & 1 & -1
\end{pmatrix} . \tag{B.4}$$

The preconditioned equilibrium moments are:

$$e^{eq} = -2\rho + \frac{3\rho_0(u^2+v^2)}{\gamma} , \tag{B.5a}$$

$$\epsilon^{eq} = \rho - \frac{3\rho_0(u^2+v^2+w^2)}{\gamma} , \tag{B.5b}$$

$$q_x^{eq} = \rho_0 u , \tag{B.5c}$$

$$q_y^{eq} = \rho_0 v , \tag{B.5d}$$

$$q_z^{eq} = \rho_0 w , \tag{B.5e}$$

$$p_{xx}^{eq} = \frac{\rho_0(2u^2-v^2-w^2)}{\gamma} , \tag{B.5f}$$

$$p_{zz}^{eq} = \frac{\rho_0(v^2-w^2)}{\gamma} , \tag{B.5g}$$

$$p_{xy}^{eq} = \frac{\rho_0 uv}{\gamma} , \tag{B.5h}$$

$$p_{yz}^{eq} = \frac{\rho_0 vw}{\gamma} , \text{ and} \tag{B.5i}$$

$$p_{xz}^{eq} = \frac{\rho_0 uw}{\gamma} . \tag{B.5j}$$

The eighting factors in Eq. (1.9) are: $w_0 = 1/3$, $w_{1-6} = 1/18$, and $w_{7-18} = 1/36$.

As a reference for possible linear stability analysis, the following matrix is the $D3Q19$ equivalent to the $D2Q9$ G_{ij} matrix, Eq.(1.26):

$$G_{ij} = \begin{pmatrix}
0 & 0 & 0 & 0 & 0 & 0 & 0 & 0 & 0 & 0 & 0 & 0 & 0 & 0 & 0 & 0 & 0 & 0 & 0 \\
0 & -s_e & 0 & \frac{20us_e}{13\gamma} & 0 & \frac{20vs_e}{13\gamma} & 0 & \frac{20ws_e}{13\gamma} & 0 & 0 & 0 & 0 & 0 & 0 & 0 & 0 & 0 & 0 & 0 \\
0 & 0 & -s_\epsilon & 0 & 0 & 0 & 0 & 0 & 0 & 0 & 0 & 0 & 0 & 0 & 0 & 0 & 0 & 0 & 0 \\
0 & 0 & 0 & 0 & 0 & 0 & 0 & 0 & 0 & 0 & 0 & 0 & 0 & 0 & 0 & 0 & 0 & 0 & 0 \\
0 & 0 & 0 & 0 & -s_q & 0 & 0 & 0 & 0 & 0 & 0 & 0 & 0 & 0 & 0 & 0 & 0 & 0 & 0 \\
0 & 0 & 0 & 0 & 0 & 0 & 0 & 0 & 0 & 0 & 0 & 0 & 0 & 0 & 0 & 0 & 0 & 0 & 0 \\
0 & 0 & 0 & 0 & 0 & 0 & -s_q & 0 & 0 & 0 & 0 & 0 & 0 & 0 & 0 & 0 & 0 & 0 & 0 \\
0 & 0 & 0 & 0 & 0 & 0 & 0 & 0 & 0 & 0 & 0 & 0 & 0 & 0 & 0 & 0 & 0 & 0 & 0 \\
0 & 0 & 0 & 0 & 0 & 0 & 0 & 0 & -s_q & 0 & 0 & 0 & 0 & 0 & 0 & 0 & 0 & 0 & 0 \\
0 & 0 & 0 & \frac{10us_\nu}{9\gamma} & 0 & -\frac{5vs_\nu}{9\gamma} & 0 & -\frac{5ws_\nu}{9\gamma} & 0 & -s_\nu & 0 & 0 & 0 & 0 & 0 & 0 & 0 & 0 & 0 \\
0 & 0 & 0 & 0 & 0 & 0 & 0 & 0 & 0 & 0 & -s_\pi & 0 & 0 & 0 & 0 & 0 & 0 & 0 & 0 \\
0 & 0 & 0 & 0 & 0 & \frac{5vs_\nu}{3\gamma} & 0 & -\frac{5ws_\nu}{3\gamma} & 0 & 0 & 0 & -s_\nu & 0 & 0 & 0 & 0 & 0 & 0 & 0 \\
0 & 0 & 0 & 0 & 0 & 0 & 0 & 0 & 0 & 0 & 0 & 0 & -s_\pi & 0 & 0 & 0 & 0 & 0 & 0 \\
0 & 0 & 0 & \frac{5vs_\nu}{2\gamma} & 0 & \frac{5us_\nu}{2\gamma} & 0 & 0 & 0 & 0 & 0 & 0 & 0 & -s_\nu & 0 & 0 & 0 & 0 & 0 \\
0 & 0 & 0 & 0 & 0 & \frac{5ws_\nu}{2\gamma} & 0 & \frac{5vs_\nu}{2\gamma} & 0 & 0 & 0 & 0 & 0 & 0 & -s_\nu & 0 & 0 & 0 & 0 \\
0 & 0 & 0 & \frac{5ws_\nu}{2\gamma} & 0 & 0 & 0 & \frac{5us_\nu}{2\gamma} & 0 & 0 & 0 & 0 & 0 & 0 & 0 & -s_\nu & 0 & 0 & 0 \\
0 & 0 & 0 & 0 & 0 & 0 & 0 & 0 & 0 & 0 & 0 & 0 & 0 & 0 & 0 & 0 & -s_m & 0 & 0 \\
0 & 0 & 0 & 0 & 0 & 0 & 0 & 0 & 0 & 0 & 0 & 0 & 0 & 0 & 0 & 0 & 0 & -s_m & 0 \\
0 & 0 & 0 & 0 & 0 & 0 & 0 & 0 & 0 & 0 & 0 & 0 & 0 & 0 & 0 & 0 & 0 & 0 & -s_m
\end{pmatrix}. \tag{B.6}$$

C – Derivation of lattice Boltzmann methods

A succinct derivation is provided in the following which helps to connect the continuum Boltzmann equation with the discrete Boltzmann equation, and the latter with the standard lattice Boltzmann algorithm. Furthermore, the Chapman-Enskog expansion is used to derive the Navier-Stokes equations from the discrete Boltzmann one. This appendix is based on references [1, 18, 19, 116].

C.1 Continuum Boltzmann equation

The Boltzmann equation describes the evolution of the phase density f due to the free flight and the collision of particles. Collisions between particles involve exchange of momentum and energy, and f will change accordingly. $f(x_i, e_i, t)$ is the single-particle phase density, or distribution function, and e_i is the microscopic velocity. The continuum Boltzmann equation with the BGK [32] collision operator (also called SRT in this Thesis) is considered:

$$\frac{\partial f}{\partial t} + e_i \frac{\partial f}{\partial x_i} = \frac{1}{\tau_s}\left(f - f^{(0)}\right) \; ; \tag{C.7}$$

where τ_s is the single relaxation time of the collision model. The equilibrium distribution function $f^{(0)}$ is derived to ensure that the proper values of the conserved macroscopic variables are recovered:

$$\rho = \int f^{(0)} de_i, \qquad \rho u_i = \int e_i f^{(0)} de_i, \qquad \rho RT = \frac{1}{3}\int (e_i - u_i)^2 f^{(0)} de_i \; ; \tag{C.8}$$

and that $\ln f^{(0)}$ is collisional invariant. This yields the following *Maxwellian* expression:

$$f^{(0)} = \frac{\rho}{(2\pi RT)^{(3/2)}} exp\left[-\frac{(e_i - u_i)^2}{2RT}\right] \; ; \tag{C.9}$$

where ρ, u_i and T are the macroscopic density, velocity and temperature; and R is the ideal gas constant.

C.2 Discrete Boltzmann equation

The discrete Boltzmann equation can be derived by truncating the continuum Boltzmann equation (C.7) in velocity space. As low-Mach-number flows are usually simulated, the equilibrium distribution function is expanded up to second order in the macroscopic velocity:

$$f^{(0)} = \rho w(e_i) \left[1 + \frac{e_i u_i}{RT} + \frac{(e_i u_i)^2}{2(RT)^2} - \frac{u_i^2}{2RT} \right] + O(u^3) \,, \tag{C.10}$$

where the weight function is:

$$w(e_i) = (2\pi RT)^{-3/2} exp(-e_i^2/2RT) \,. \tag{C.11}$$

Using Eq. (C.10) the integrals in Eq. (C.8) are all of the form:

$$\int p_n(e_i) w(e_i) de_i \,, \; 0 \leq n \leq 5 \,, \tag{C.12}$$

where $p_n(e_i)$ are polynomials of degree n in the components of e_i. These integrals can be evaluated as sums using Gaussian quadrature formulas [13]:

$$\int p_n(e_i) w(e_i) de_i = \sum_{\alpha=0}^{Q} w_\alpha p(e_{i\alpha}) \,. \tag{C.13}$$

The points $e_{i\alpha}$ are the quadrature points, the coefficients w_α are the weight factors, and Q is the number of quadrature points. Q depends on the degree n and on the dimension D of the e_i space.

The continuum Boltzmann equation (C.7) can be replaced by the discrete Boltzmann equation using the quadrature points. This is the so called lattice Boltzmann equation:

$$\frac{\partial f_\alpha}{\partial t} + e_{i\alpha} \frac{\partial}{\partial x_i} f_\alpha = \frac{1}{\tau_s} \left(f_\alpha - f_\alpha^{(0)} \right) \,, \text{ for } \alpha = 0, ..., Q \,. \tag{C.14}$$

The macroscopic quantities of density, momentum, and momentum flux are now:

$$\rho = \sum_{\alpha=0}^{Q} f_\alpha, \qquad \rho u_i = \sum_{\alpha=0}^{Q} e_{i\alpha} f_\alpha, \qquad \Pi_{ij} = \sum_{\alpha=0}^{Q} e_{i\alpha} e_{j\alpha} f_\alpha \,. \tag{C.15}$$

Recently, a new procedure to derive lattice Boltzmann methods has been developed [14] based on the relation between entropy construction and roots of Hermite polynomials. This is a systematic procedure which can be used to construct numerically stable and complete Galilean invariant LB models with arbitrary precision.

C.3 Chapman-Enskog expansion

The Chapman-Enskog expansion is nowadays applied in a more comprehensive form than the originally one developed independently by Enskog and Chapman [1].

The Navier Stokes equations can be recovered from the lattice Boltzmann equation in the limit of low Mach and Knudsen numbers through a Chapman-Enskog expansion. This expansion introduces a small parameter ϵ (which can be physically identified with the Knudsen number) so that the lattice Boltzmann equation (C.14) with the SRT collision operator Eq. (1.13) becomes:

$$\frac{\partial f_\alpha}{\partial t} + e_{i\alpha}\frac{\partial f_\alpha}{\partial x_i} = \frac{1}{\epsilon\tau_s}\left(f_\alpha - f_\alpha^{(0)}\right) . \tag{C.16}$$

The temporal and spatial derivatives appear at lower order in ϵ than the collision term. The distribution function and time are expanded as follows:

$$f_\alpha = f_\alpha^{(0)} + \epsilon f_\alpha^{(1)} + \epsilon^2 f_\alpha^{(2)} \cdots ; \tag{C.17a}$$

$$\frac{\partial}{\partial t} = \frac{\partial}{\partial t_0} + \epsilon\frac{\partial}{\partial t_1} + \cdots ; \tag{C.17b}$$

where t_0 is an advective timescale and t_1 is a diffusive one. Two solvability conditions are imposed:

$$\sum f_\alpha^n = \sum e_{i\alpha} f_\alpha^n = 0 , \ n = 1, 2, ... \tag{C.18}$$

Therefore, higher order terms of the distribution functions ($f_\alpha^n, n = 1, 2, ...$) do not contribute to mass and momentum conservation, and only moments of the known equilibrium functions $f_\alpha^{(0)}$ and their derivatives in time and space are needed. In the equations below, ϵ can be included in the relaxation time τ_s and hence be set equal to unity.

Using the expansion Eq. (C.17) in Eq. (C.16) the following equations are obtained at $O(1)$ and $O(\epsilon)$:

$$\frac{\partial f_\alpha^{(0)}}{\partial t_0} + e_{i\alpha}\frac{\partial f_\alpha^{(0)}}{\partial x_i} = -\frac{1}{\tau_s} f_\alpha^{(1)} ; \tag{C.19a}$$

$$\frac{\partial f_\alpha^{(0)}}{\partial t_1} + \frac{\partial f_\alpha^{(1)}}{\partial t_0} + e_{i\alpha}\frac{\partial f_\alpha^{(1)}}{\partial x_i} = -\frac{1}{\tau_s} f_\alpha^{(2)} . \tag{C.19b}$$

The Euler equations are obtained by taking the first $\sum_\alpha(\cdot)$ and the second $\sum_\alpha e_{i\alpha}(\cdot)$ moments of Eq. (C.19a):

$$\frac{\partial \rho}{\partial t_0} + \frac{\partial \rho u_i}{\partial x_i} = 0 ; \tag{C.20a}$$

$$\frac{\partial \rho u_i}{\partial t_0} + \frac{\partial \Pi_{ij}^{(0)}}{\partial x_i} = 0 . \tag{C.20b}$$

Similarly for Eq. (C.19b):

$$\frac{\partial \rho}{\partial t_1} = 0\,; \tag{C.21a}$$

$$\frac{\partial \rho u_i}{\partial t_1} + \frac{\partial \Pi_{ij}^{(1)}}{\partial x_i} = 0\,. \tag{C.21b}$$

The Navier-Stokes equations are obtained by combining Eqs. (C.20) and Eqs. (C.21) and neglecting $O(\epsilon^2)$ terms:

$$\frac{\partial \rho}{\partial t} + \frac{\partial \rho u_i}{\partial x_i} = 0\,; \tag{C.22a}$$

$$\frac{\partial \rho u_i}{\partial t} + \frac{\partial \Pi_{ij}^{(0)}}{\partial x_i} + \frac{\partial \epsilon \Pi_{ij}^{(1)}}{\partial x_i} = 0\,; \tag{C.22b}$$

where $\Pi_{ij}^{(0)} = \sum_{\alpha=0}^{Q} e_{i\alpha} e_{j\alpha} f_\alpha^{(0)}$ and $\Pi_{ij}^{(1)} = \sum_{\alpha=0}^{Q} e_{i\alpha} e_{j\alpha} f_\alpha^{(1)} \approx \sum_{\alpha=0}^{Q} e_{i\alpha} e_{j\alpha} (f_\alpha - f_\alpha^{(0)})$.

C.4 Standard lattice Boltzmann algorithm

Integrating Eq. (C.14) along characteristics over the time step δt, the following equation is obtained:

$$f_\alpha(x_i + e_{i\alpha}\delta t, t+\delta t) - f_\alpha(x_i,t) = -\frac{1}{\tau_s}\int_t^{t+\delta t} f_\alpha(x_i + e_{i\alpha}s, t+s) - f_\alpha^{(0)}(x_i + e_{i\alpha}s, t+s) ds\,. \tag{C.23}$$

Note that the time integration $(t, t+\delta t)$ is coupled with the space integration $(x_i, x_i + e_{i\alpha}\delta t)$. Application of the trapezoidal rule for second-order accuracy and unconditional stability leads to:

$$\begin{aligned} f_\alpha(x_i + e_{i\alpha}\delta t, t+\delta t) \;&-\; f_\alpha(x_i,t) = \\ &-\; \frac{\delta t}{2\tau_s}[f_\alpha(x_i + e_{i\alpha}\delta t, t+\delta t) - f_\alpha^{(0)}(x_i + e_{i\alpha}\delta t, t+\delta t) \\ &+\; f_\alpha(x_i,t) - f_\alpha^{(0)}(x_i,t)] + O(\delta t^3)\,. \end{aligned} \tag{C.24}$$

To simplify the computation the following distribution function is introduced:

$$g_\alpha(x_i,t) = f_\alpha(x_i,t) + \frac{\delta t}{2\tau_s}[f_\alpha(x_i,t) - f_\alpha^{(0)}(x_i,t)]\,. \tag{C.25}$$

The lattice Boltzmann equation can be recast in a simpler form:

$$g_\alpha(x_i + e_{i\alpha}\delta t, t+\delta t) - g_\alpha(x_i,t) = -\frac{\delta t}{\tau_s + \delta t/2}[g_\alpha(x_i,t) - f_\alpha^{(0)}(x_i,t)]\,; \tag{C.26}$$

to which the collision-propagation algorithm can be applied (see Chapter 1); and the macroscopic density, momentum and momentum flux are now constructed from moments of g_α as follows:

$$\rho = \sum_{\alpha=0}^{Q} g_\alpha, \qquad \rho u_i = \sum_{\alpha=0}^{Q} e_{i\alpha} g_\alpha, \qquad \left(1 + \frac{\delta t}{2\tau_s}\right) \Pi_{ij} = \sum_{\alpha=0}^{Q} e_{i\alpha} e_{j\alpha} g_\alpha + \frac{\delta t}{2\tau_s} \Pi_{ij}^{(0)} \ . \tag{C.27}$$

In the notation used in this Thesis, the variables denoted with f_α are actually the g_α distribution functions.

Bibliography

[1] S. Chapman and T. G. Cowling. *The mathematical theory of non-uniform gases*. Cambridge University Press, third edition, 1991.

[2] Y. Sone. *Kinetic theory and fluid dynamics*. Birkhäuser, 2002.

[3] U. Frisch, B. Hasslacher, and Y. Pomeau. Lattice-gas automata for the Navier-Stokes equation. *Phys. Rev. Lett.*, 56:1505–1508, 1986.

[4] G. Doolen, editor. *Lattice gas methods for partial differential equations*, volume 4 of *Santa Fe Institute studies in the sciences of complexity*, 1990. Addison-Wesley.

[5] F. J. Higuera and J. Jiménez. Boltzmann approach to lattice gas simulations. *Europhys. Lett.*, 9:663–668, 1989.

[6] F. J. Higuera, S. Succi, and R. Benzi. Lattice gas dynamics with enhanced collisions. *Europhys. Lett.*, 9:345?349, 1989.

[7] PowerFlow by Exa Corporation. http://www.exa.com.

[8] R. Benzi, S. Succi, and M. Vergassola. The lattice Boltzmann equation: theory and applications. *Phys. Rep.*, 222:3, 1992.

[9] S. Chen and G. Doolen. Lattice Boltzmann method for fluid flows. *Annu. Rev. Fluid Mech.*, 30:329–364, 1998.

[10] D. A. Wolf-Gladrow. *Lattice-Gas Cellular Automata and Lattice Boltzmann Models. An Introduction*. Lecture Notes in Mathematics 1725. Springer, 2000.

[11] S. Succi. *The Lattice Boltzmann Equation for Fluid Dynamics and Beyond*. Oxford, 2001.

[12] D. Yu, R. Mei, L. S. Luo, and W. Shyy. Viscous flow computations with the method of lattice Boltzmann equation. *Prog. Aerosp. Sci.*, 39:329–367, 2003.

[13] X. He and L. S. Luo. Theory of lattice Boltzmann mehtod: From the Boltzmann equation to the lattice Boltzmann equation. *Phys. Rev. E*, 56:6811–6817, 1997.

[14] S. S. Chikatamarla and I. V. Karlin. Entropy and Galilean invariance of lattice Boltzmann theories. *Phys. Rev. Lett.*, 97:190601, 2006.

[15] Y. H. Qian, D. d'Humières, and P. Lallemand. Lattice BGK Models for Navier-Stokes Equation. *Europhys. Lett.*, 17:479–484, 1992.

[16] M. Junk, A. Klar, and L. S. Luo. Asymptotic analysis of the lattice Boltzmann equation. *J. Comp. Phys.*, 210:676–704, 2005.

[17] D. J. Holdych, D. R. Noble, J. G. Georgiadis, and R. O. Buckius. Truncation error analysis of lattice Boltzmann methods. *J. Comput. Phys.*, 193(2):595 – 619, 2004.

[18] C. Cercignani. *Rarefied gas dynamics: from basic concepts to actual calculations.* Cambridge University Press, 2000.

[19] H. Struchtrup. *Macroscopic transport equations for rarefied gas flows: approximation methods in kinetic theory.* Springer, 2005.

[20] T. Lee and C. L. Lin. An Eulerian description of the streaming process in the lattice Boltzmann equation. *J. Comput. Phys.*, 185:445 – 471, 2003.

[21] T. Lee and C. L. Lin. Rarefaction and compressibility effcts of the lattice-Boltzmann-equation method in a gas microchannel. *Phys. Rev. E*, 71:046706, 2005.

[22] A. Bardow, I. V. Karlin, and A. A. Gusev. General characteristic-based algorithm for off-lattice Boltzmann simulations. *Europhys. Lett.*, 75 (3):434–440, 2006.

[23] D. d'Humières. Generalized lattice-Boltzmann equations. *AIAA Rarefied Gas Dynamics: Theory and Simulations. Prog. Astronaut. Aeronaut.*, 59:450–548, 1992.

[24] P. Lallemand and L. S. Luo. Theory of the lattice Boltzmann method: Dispersion, dissipation, isotropy, Galilean invariance, and stability. *Phys. Rev. E*, 61: 6546–6562, 2000.

[25] Z. Guo, C. Zheng, and B. Shi. Discrete lattice effects on the forcing term in the lattice Boltzmann method. *Phys. Rev. E.*, 65:046308, 2002.

[26] Q. S. Zou, S. L. Hou, S. Y. Chen, and G. D. Doolen. An improved incompressible lattice Boltzmann model for time-independent flows. *J. Stat. Phys.*, 72(2-6): 165–168, 1995.

[27] X. He and L. S. Luo. Lattice Boltzmann model for the incompressible Navier-Stokes equation. *J. Stat. Phys.*, 88:927–944, 1997.

[28] P. Asinari and T. Ohwada. Connection between kinetic methods for fluid-dynamic equations and macroscopic finite-difference schemes. *Comp. & Math. Applic.*, 2008. (Accepted).

[29] H. Struchtrup. Scaling and expansion of moment equations in kinetic theory. *J. Stat. Phys.*, 125:565–587, 2006.

[30] I. Ginzburg and D. d'Humières. Multireflection boundary conditions for lattice Boltzmann models. *Phys. Rev. E*, 68:066614, 2003.

[31] I. Ginzburg, F. Verhaeghe, and D. d'Humières. Two-relaxation-time lattice Boltzmann scheme: about parametrization, velocity, pressure and mixed boundary conditions. *Commun. Comput. Phys.*, 3(2):427–478, 2008.

[32] P. L. Bhatnagar, E. P. Gross, and M. Krook. A model for collision process in gases, I. Small amplitude processes in charged and neutral one-component system. *Phys. Rev.*, 94:511–525, 1954.

[33] T.J. Chung. *Computational Fluid Dynamics*. Cambridge University Press, 2002.

[34] A. Caiazzo. Analysis of lattice Boltzmann initialization routines. *J. Stat. Phys.*, 121:37–48, 2005.

[35] P. A. Skordos. Initial and boundary conditions for the lattice Boltzmann method. *Phys. Rev. E*, 48:4823, 1993.

[36] R. Mei, L. S. Luo, P. Lallemand, and D. d'Humière. Consistent initial conditions for lattice Boltzmann simulations. *Comput. & Fluids*, 35:855–862, 2006.

[37] P. Van Leemput. *Multiscale and equation-free computing for lattice Boltzmann models*. PhD thesis, Katholieke Universiteit Leuven, 2007.

[38] M. Bouzidi, M. Firdaouss, and P. Lallemand. Momentum transfer of a Boltzmann-lattice fluid with boundaries. *Phys. Fluids*, 13(11):3452–3459, 2001.

[39] Q. Zou and X. He. On pressure and velocity boundary conditions for the lattice Boltzmann BGK model. *Phys. Fluids*, 9:1591–1598, 1997.

[40] D. Yu, R. Mei, and W. Shyy. Improved treatment of the open boundary in the method of lattice Boltzmann equation. *Prog. Comp. Fluid Dyn.*, 5(1/2):3–12, 2005.

[41] Z. Yang. *Analysis of lattice Boltzmann boundary conditions*. PhD thesis, Konstanz Universitaet, 2007.

[42] J. D. Sterling and S. Chen. Stability analysis of lattice Boltzmann methods. *J. Comput. Phys.*, 123:196–206, 1996.

[43] D. N. Siebert, L. A. Hegele Jr., and P. C. Philippi. Lattice Boltzmann equation linear stability analysis: thermal and athermal models. *Phys. Rev. E*, 77:026707, 2008.

[44] Mathematica. *Wolfram Research, Inc.* Wolfram Research, Inc., Champaign, Illinois, version 5.0 edition, 2003.

[45] T. Poinsot and S. K. Lele. Boundary conditions for direct simulations of compressible viscous flows. *J. Comput. Phys.*, 101:104–129, 1992.

[46] T. Poinsot and D. Veynante. *Theoretical and numerical combustion.* Edwards, 2001.

[47] T. Colonius. Modeling artificial boundary conditions for compressible flow. *Annu. Rev. Fluid Mech.*, 36:315–345, 2004.

[48] P. Martínez-Lera, S. Izquierdo, and N. Fueyo. Lattice-Boltzmann LES of vortex shedding in the wake of a square cylinder. In *Complex Effects in Large Eddy Simulations*, volume 56 of *LNCSE*, pages 203–217. Springer, 2007.

[49] M. Breuer, J. Bernsdorf, T. Zeiser, and F. Durst. Accurate computations of the laminar flow past a square cylinder based on two different methods: lattice-Boltzmann and finite-volume. *Int. J. Heat Fluid Flow*, 21:186–196(11), 2000.

[50] S. Chen, D. Martínez, and R. Mei. On boundary conditions in lattice Boltzmann methods. *Phys. Fluids*, 8:2527, 1996.

[51] K. Ogata. *Modern Control Engineering.* Prentice Hall, 1990.

[52] L. Selle, F. Nicoud, and T. Poinsot. Actual impedance of nonreflecting boundary conditions: implications for computations of resonators. *AIAA J.*, 42:958–964, 2004.

[53] R. Mei, D. Yu, W. Shyy, and L. S. Luo. Force evaluation in the lattice Boltzmann method involving curved geometry. *Phys. Rev. E*, 65:041203, 2002.

[54] C. Pan, L. S. Luo, and C. T. Miller. An evaluation of lattice Boltzmann schemes for porous medium flow simulation. *Comput. & Fluids*, 35:898–909, 2006.

[55] J. Boyd, J. Buick, J. A. Cosgrove, and P. Stansell. Application of the lattice Boltzmann model to simulated stenosis growth in a two-dimensional carotid artery. *Phys. Med. Biol.*, 50:4783?4796, 2005.

[56] C. van Treeck, E. Rank, M. Krafczyk, J. Tölke, and B. Nachtwey. Extension of a hybrid thermal LBE scheme for large-eddy-simulations of turbulent convective flows. *Comput. & Fluids*, 35:863–871, 2006.

[57] E. Fares. Unsteady flow simulation of the Ahmed reference body using a lattice Boltzmann approach. *Comput. & Fluids*, 35:940–950, 2006.

[58] A. J. C. Ladd. Numerical simulations of particulate suspensions via a discretized Boltzmann equation. Part 2. Theoretical foundation. *J. Fluid Mech.*, 271:285–309, 1994.

[59] D. P. Ziegler. Boundary conditions for lattice Botlzmann simulations. *J. Stat. Phys.*, 71:1171–1177, 1993.

[60] D. R. Noble, S. Y. Chen, J. G. Georgiadis, and R. O. Buckius. A consistent hydrodynamic boundary-condition for the lattice Boltzmann method. *Phys. Fluids*, 7(1):203–209, 1995.

[61] R. S. Maier, R. S. Bernard, and D. W. Grunau. Boundary conditions for the lattice Boltzmann method. *Phys. Fluids*, 8:1788, 1996.

[62] I. Ginzbourg and P. M. Adler. Boundary flow condition analysis for the three-dimensional lattice Boltzmann model. *J. Phys. II France*, 4:191–214, 1994.

[63] O. Filippova and D. Hänel. Lattice-Boltzmann simulation of gas-particle flow in filters. *Comput. & Fluids*, 26(7):697 – 712, 1997.

[64] R Mei, L. S. Luo, and W. Shyy. An accurate curved boundary treatment in the lattice Boltzmann method. *J. Comput. Phys.*, 155:307, 1999.

[65] H. Chen, C. Teixeira, and K. Molving. Realization of fluid boundary conditions via discrete Boltzmann dynamics. *Int. J. Mod. Phys. C*, 9:1281–1292, 1998.

[66] M. Rohde, D. Kandhai, J. J. Derksen, and H. E. A. Van den Akker. Improved bounce-back methods for no-slip walls in lattice-Boltzmann schemes: theory and simulations. *Phys. Rev. E*, 67:066703, 2003.

[67] R. Verberg and A. J. C. Ladd. Lattice-Boltzmann model with sub-grid-scale boundary conditions. *Phys. Rev. Lett.*, 84:2148–2151, 2000.

[68] Z. Guo, C. Zheng, and B. Shi. An extrapolation method for boundary conditions in lattice Boltzmann method. *Phys. Fluids*, 14(6), 2002.

[69] I. Ginzbourg and d'Humières D. Local second-order boundary method for lattice Boltzmann models. *J. Stat. Phys.*, 84:927–971, 1996.

[70] M. Junk and Z. Yang. Asymptotic analysis of lattice Boltzmann boundary conditions. *J. Stat. Phys.*, 112:3–35, 2005.

[71] B. Chun and A. J. C. Ladd. Interpolated boundary condition for lattice Boltzmann simulations of flows in narrow gaps. *Phys. Rev. E*, 75:066705, 2007.

[72] C. Shu, N. Liu, and Y. T. Chew. A novel immersed boundary velocity correction-lattice Boltzmann method and its application to simulate flow past a circular cylinder. *J. Comput. Phys.*, 226:1607–1622, 2007.

[73] M. Sbragaglia and S. Succi. Analytical calculation of slip flow in lattice Boltzmann models with kinetic boundary conditions. *Phys. Fluids*, 17:093602, 2005.

[74] L. Szalmás. Slip-flow boundary condition for straight walls in the lattice Boltzmann model. *Phys. Rev. E*, 73:066710, 2006.

[75] X. Yin, D. L. Koch, and R. Verberg. Lattice-Boltzmann method for simulating spherical bubbles with no tangential stress boundary conditions. *Phys. Rev. E*, 73:026301, 2006.

[76] W. Miller. Flow in the driven cavity calculated by the lattice Boltzmann method. *Phys. Rev. E*, 51:3659–3669, 1995.

[77] S. Ansumali and I. V. Karlin. Kinetic boundary conditions in the lattice Boltzmann method. *Phys. Rev. E*, 66(2):026311, 2002.

[78] S. Majumdar, G. Iaccarino, and P. Durbin. RANS solvers with adaptive structured boundary non-conforming grids. *Annual Research Briefs. Center for Turbulence Research*, pages 353–366, 2001.

[79] G. Kalitzin and G. Iaccarino. Toward immerse boundary simulation of high Reynolds number flows. *Annual Research Briefs, Center for Turbulent Research*, pages 369–378, 2003.

[80] U. Piomelli and E. Balaras. Wall-layer models for large-eddy simulations. *Ann. Rev. Fluid Mech.*, 34:349, 2002.

[81] Z. Guo, T. S. Zhao, and Y. Shi. Physical symmetry, spatial accuracy, and relaxation time of the lattice Boltzmann equation for microgas flow. *J. Appl. Phys*, 99:074903, 2006.

[82] J. Crank. *The Mathematics of Diffusion.* Oxford University Press, second edition, 1975.

[83] R. Clift, J. R. Grace, and M. E. Weber. *Bubbles, drops and particles.* Academic Press, 1978.

[84] R. Mittal and Iaccarino G. Immersed boundary methods. *Annu. Rev. Fluid Mech.*, 37:239–261, 2005.

[85] H. Viviand. *Numerical Methods for the Euler Equations of Fluid Dynamics.* SIAM, 1985.

[86] E. Turkel. Preconditioned methods for solving the incompressible and low-speed compressible equations. *J. Comput. Phys.*, 72:277–298, 1987.

[87] Y. H. Choi and C. L. Merkle. The application of preconditioning in viscous flows. *J. Comput. Phys.*, 105:207–223, 1993.

[88] E. Turkel. Preconditioning techniques in computational fluid dynamics. *Annu. Rev. Fluid Mech.*, 31:385–416, 1999.

[89] D. Kandhai, A. Koponen, A. Hoekstra, M. Kataja, J. Timonen, and P.M.A. Sloot. Implementation aspects of 3D lattice-BGK: boundaries, accuracy and a fast relaxation method. *J. Comput. Phys.*, 150:1–20, 1999.

[90] Z. Guo, T. S. Zhao, and Y. Shi. Preconditioned lattice-Boltzmann method for steady flows. *Phys. Rev. E*, 70:066706–1, 2004.

[91] C. L. Lin and Y. G. Lai. Lattice Boltzmann method on composite grids. *Phys. Rev. E*, 62:2219–2225, 2000.

[92] D. Yu, R. Mei, and W. Shyy. A multi-block lattice Boltzmann method for viscous fluid flow. *Int. J. Numer. Meth. Fluids*, 39:99–120, 2002.

[93] O. Filippova and D. Hänel. Acceleration of lattice-BGK schemes with grid refinement. *J. Comput. Phys.*, 165:407–427, 2000.

[94] D. J. Mavriplis. Multigrid solution of the steady-state lattice Boltzmann equation. *Comput. & Fluids*, 35:793–804, 2006.

[95] R. Mei and W. Shyy. On the finite difference-based lattice Boltzmann method in curvilinear coordinates. *J. Comput. Phys.*, 143(2):426 – 448, 1998.

[96] G. Peng, H. Xi, C. Duncan, and S. H. Chou. Finite volume scheme for the lattice Boltzmann method on unstructured meshes. *Phys. Rev. E*, 59:4675–82, 1999.

[97] M. Stiebler, J. Tölke, and M. Krafczyk. An upwind discretization scheme for the finite volume lattice Boltzmann method. *Comput. & Fluids*, 35:814 – 819, 2006.

[98] M. Bernaschi, S. Succi, and H. Chen. Accelerated lattice Boltzmann schemes for steady-state flow simulations. *J. Sci. Comput.*, 16(2):135 – 144, 2001.

[99] J. Tölke, M. Krafczyk, and E. Rank. A multigrid solver for the discrete Boltzmann equation. *J. Stat. Phys.*, 107:573–591, 2002.

[100] J. M. Weiss and W. A. Smith. Preconditioning applied to variable and constant density flows. *AIAA Journal*, 33(11):2050–2057, 1995.

[101] P. N. Shankar and M. D. Deshpande. Fluid Mechanics in the Driven Cavity. *Annu. Rev. Fluid Mech.*, 32:93–136, 2000.

[102] E. Turkel and V. N. Vatsa. Local preconditioners for steady and unsteady flow applications. *Mathematical Modelling and Numerical Analysis-ESAIM*, 39: 515–535, 2005.

[103] O. Botella and R. Peyret. Benchmark spectral results on the lid-driven cavity flow. *Comput. & Fluids*, 27:421–433, 1998.

[104] P. J. Dellar. Incompressible limits of lattice Boltzmann equations using multiple relaxation times. *J. Comput. Phys.*, 190:351–370, 2003.

[105] X. D. Niu, C. Shu, and Y. T. Chew. A thermal lattice Boltzmann model with diffuse scattering boundary condition for micro thermal flows. *Comput. & Fluids*, 36:273–281, 2007.

[106] C. M. Ho and Y. C. Tai. Micro-electro-mechanical-systems (MEMS) and fluid flows. *Annu. Rev. Fluid Mech.*, 30:579–612, 1998.

[107] G. Karniadakis, A. Beskok, and N. R. Aluru. *Microflows and Nanoflows: Fundamentals and Simulation*. Springer-Verlag New York Inc, 2005.

[108] E. B. Arkilic, M. A. Schmidt, and K. S. Breuer. Gaseous slip flow in long microchannels. *J. Microelectromech. Syst.*, 6(2):167–178, 1997.

[109] B. F. Armaly, F. Durst, J. C. F. Pereira, and B. Schönung. Experimental and theoretical investigation of backward-facing step flow. *J. Fluid Mech.*, 127: 473–496, 1983.

[110] R. A. Brownlee, A. N. Gorban, and J. Levesley. Stability and stabilization of the lattice Boltzmann method. *Phys. Rev. E*, 75:036711, 2007.

[111] M. Geier, A. Greiner, and J. G. Korvink. Cascaded digital lattice Boltzmann automata for high Reynolds number flow. *Phys. Rev. E*, 73(6):066705, 2006.

[112] J. Latt and B. Chopard. Lattice Boltzmann method with regularized non-equilibrium distribution functions. *Math. Comp. Sim.*, 72:165–168, 2006.

[113] R. Prosser. Improved boundary conditions for the direct numerical simulation of turbulent subsonic flows. I: inviscid flows. *J. Comput. Phys.*, 207:736 – 768, 2005.

[114] S. Ansumali and I. V. Karlin. Consistent lattice Boltzmann method. *Phys. Rev. Lett.*, 95:260605, 2005.

[115] J. Tölke, S. Freudiger, and M. Krafczyk. An adaptive scheme using hierarchical grids for lattice Boltzmann multi-phase flow simulation. *Comput. & Fluids*, 35: 820–830, 2006.

[116] P. Dellar. Bulk and shear viscosities in lattice Boltzmann equations. *Phys. Rev. E*, 64:031203, 2001.